Numerical and laboratory investigations for maximization of production from tight/shale oil reservoirs: From fundamental studies to technology development and evaluation

ESD14089

Final Technical Report

Date: April 30, 2019
Period: October 1, 2014 – September 30, 2018
NETL Manager: Stephen Henry

Principal Investigators: George Moridis, Matthew Reagan

TABLE OF CONTENTS

GOAL OF THIS REPORT

The intent of the report is to highlight and summarize previously reported results generated during the four-year term of the project, and to report on the completion of the proposed tasks.

In this report we describe the project tasks across multiple Budget Periods (BPs), with a description of the work performed and the resulting deliverables. The complete project was funded in two two-year phases (one budget period per year), with slightly different task numbering between phases. Therefore, in this report, we have combined related tasks in Phase I and Phase II for reporting, as research work continued seamlessly between the two phases and the four budget periods. Therefore, this report is structured in four parts, each addressing an area of the research work:

PART I addresses preliminary and administrative tasks

PART II addresses reservoir simulation tasks

PART III addresses laboratory and visualization tasks

PART IV addresses molecular-scale tasks

The four areas of research communicated continuously during the project timeline, with lab and simulation results informing research directions at each milestone.

PROJECT SUMMARY

Gas production from tight gas/shale gas reservoirs over the last decade has met with spectacular success with the advent of advanced reservoir stimulation techniques (mainly hydraulic fracturing), to the extent that shale gas is now among the main contributors to US hydrocarbon production. This remarkable success has not been matched by similar progress in the production of (relatively) low-viscosity liquid hydrocarbons (including condensates) because of the significant challenges to liquid flow posed by the ultra-low permeability (and the correspondingly high capillary pressures and irreducible liquids saturations) of such reservoirs. These difficulties have limited liquids production to a very low fraction (usually <5%) of the resources-in-place. Increasing the recovery of liquids from these ultra-low permeability systems even by 50-100% over its current very low levels (to a level that is still low in absolute terms, but very significant in relative, hence economic, terms) not only will increase production and earnings, but will have considerable wider economic implications, as the enhanced recovery will affect reserves and the valuation of companies.

This project aims to address this issue by using multi-scale laboratory investigations (nano- to core-scale) and numerical simulations (from molecular to field-scale) to (a) identify and quantify the various mechanisms involved in hydrocarbon production from such tight systems, (b) describe the thermodynamic state and overall behavior of the various fluids in the nanometer-scale pores of these tight media, (c) propose new methods for low-viscosity liquids production from tight/shale reservoirs, (d) investigate a wide range of such possible strategies, and identify the promising ones and quantitatively evaluate their expected performance. By covering the spectrum from fundamental studies to technology development and evaluation, we propose to gain a deeper understanding of the dominant processes that control production from such reservoirs and to develop a compendium of appropriate production strategies and their respective effectiveness.

PART I

PRELIMINARY TASKS

Phases I and II, Task 1: Project Management and Planning

The Recipient shall work together with the NETL project manager to maintain and update the project management plan (PMP) originally submitted at FWP approval (and formatted in accordance with the guidance provided by NETL). In the event of major modifications to the FWP an update of the PMP shall be submitted to the NETL project manager within 30 days. The NETL Project Manager shall have 20 calendar days from receipt of the revised PMP to review and provide comments to the Recipient. Within 15 calendar days after receipt of the NETL Project Manager's comments, the Recipient shall submit a final revised PMP to the NETL Project Manager for final review and approval.

The LBNL team worked together with the NETL project manager, and completed the maintenance and update of the project management plan (PMP) within the specified time frame and budget. Final PMPs were accepted in November 2014 and November 2016. The PMP and associated milestone list was updated each Budget Period under consultation with the Project Manager.

Phase I, Task 2: Definition of metrics and methodology for screening production strategies

October 1, 2014-September 30, 2016

Internal discussions within the LBNL team led to the identification (and quantification, where appropriate) of the parameters, objectives and metrics of the study, as well as the methodology. The first step involved the determination of the reference (base) cases, and the LBNL team decided that these have to be two: the first is the case of production from unfractured reservoirs (to establish a baseline for low-permeability systems), and the second is that of production from a fractured reservoir. The obvious objective was to show the significant improvement of production, and then begin to experiment with more complex modifications to production strategies. The outcomes of those simulation experiments are described in Part II.

In this task, we also finalized the choice of simulation codes, and established development pathways for code upgrades and enhancements relevant to the project. The forward codes (i.e., codes for predictive studies of system behavior) developed within the framework of DOE hydrate projects, i.e. TOUGH+, were expanded in capabilities, first adding multicomponent gas and shale-specific physics (TOUGH+RealGasBrine). Then, black oil, gassy oil, and multicomponent oil were gradually added to the codes as the research required, with an interim codebase known as TOUGH+MultiComponentMultiPhase (MCMP) used for many of the studies described in Part II. Over the course of the two project phases (2014-2018), this resulted in the development of the TOUGH+OilGasBrine code, which is now used for current and future shale oil (and shale gas) projects. This code handles conventional and tight oil and gas, EOR processes, gas sorption, pore-scale effects and micro-flow, inertial effects in wells and fractures, with oil, water, salts/inhibitors, 11 gas components, multicomponent oil with new physical properties relationships, fully non-isothermal behavior, and can be run in MPI-parallel mode on large clusters to handle large-scale systems.

PART II

RESERVOIR SIMULATION TASKS

Phase I, Task 3: Evaluation of enhanced liquids recovery using displacement processes

Phase I, Task 4: Evaluation of enhanced liquids recovery by means of viscosity reduction

Phase I, Task 7: Evaluation of enhanced liquids recovery by means of increased reservoir stimulation, well design and well operation scheduling

Phase I, Task 8: Evaluation of combination methods and of new strategies

October 1, 2014-September 30, 2016

Phase II, Task 2: Continuation of evaluation of enhanced liquids recovery

October 1, 2016-September 30, 2018

These tasks, over two project phases and eight budget periods, studied by means of numerical simulation a wide range of production enhancement strategies. The individual tasks have been discussed in quarterly reports over the two budget periods, and these tasks evolved over time as the research progressed. Here, we summarize the findings of the tasks.

Subtask II.1: Numerical Reservoir Simulation Studies

The numerical simulation studies addressed a wide range of options of fluid production from Ultra-Low Permeability (ULP) reservoirs (e.g., shales) in an effort not only to determine promising production strategies, but also to identify methods that are unlikely to yield positive effects and have to be removed from further consideration.

Subdomains in ULP Fractured Media

Following Moridis *et al* (2010), the fractured system in producing tight- and shale-gas reservoirs can be described as a set of interacting subdomains. These include the following:

- Subdomain 1 (SM): The rock matrix, i.e., the original reservoir rock in its unfeatured state. This may be composed entirely by unfeatured rock (matrix), or it may involve natural fractures that are hereafter referred to as *native fractures* (NF).
- Subdomain 2 (SF1): The fractures that original reservoir rock in its undisturbed naturally fractured initial state. These fractured are hereafter referred to as *native fractures* (NF). The existence of such fractures has been widely discussed in the literature, but opinions on their importance vary. Apiwathanasorn and Ehlig-Economides (2012) provided a summary of recent theories. Some authors consider that "*natural fractures are critical factor that control productivity*", whereas others state that "*there is no evidence of widespread open natural microfractures*" or that "*microfractures do not appear essential for production and may even reduce well productivity*".
- Subdomain 3 (SF2): The fractures or fractured network created during the reservoir stimulation (e.g., by hydro-fracturing the reservoir rock). These artificial fractures penetrate Subdomain SM, increase the surface area from which can be produced, and may intercept the natural fractures of Subdomain SF1, thus providing access of gas in a larger rock volume. The fractures

of Subdomain SF2 are expected to be the dominant pathways of flow to the well and are referred to as *primary fractures* (PF) or *hydraulic fractures* (HF).

- Subdomain 4 (SF3): This is the subdomain defined by the compression-induced (during hydraulic fracturing) or stress-release fractures (caused by changes in the geomechanical status of the rock in the vicinity of the PF during production), or by dilation of pre-existing NFs. Such fractures are referred to as *secondary fractures* (SF): they are connected to SF2, penetrate Subdomain FM and may intercept native fractures (NF), thus increasing the flow area and, consequently, production. Analysis of microseismic and water flow-back data provided evidence that such a SF3 network may originate from NFs in a pre-existing SF1 subdomain and it grows during the hydraulic fracturing treatment. According to King (2010), the HF growth is accompanied by the release of an adjacent micro-NF network that concentrates most the fluid leak-off, whereas pressure dependent leak-off into the matrix is very low because of its near-impermeability. He stated that "*natural fractures are present in almost all gas productive shale but are very rarely productive until opened and connected by a hydraulic fracturing treatment*". Moreover, "*slickwater treatments are particularly well adapted to breakdown the fissures, micro-cracks natural fractures and bedding boundaries in shale, opening up very large shale areas*".

- Subdomain 5 (SF4): This is the subdomain defined by the stress-release fractures that are induced by changes in the geomechanical status of the rock in the immediate vicinity of the wellbore because of drilling. SF4 is directly connected to SM, SF1 and SF2, and possibly intersects fractures in SF3. The fractures in S4 are hereafter referred to as *radial fractures* (RF).

Thus, SM and SF1 represent the natural (at discovery) state of the system. Drilling and well installations may inevitably cause SF4 to form. SF2 is the result of reservoir stimulation activities (and the only one over which the operator can exert control), while SF3 is a direct byproduct of them. SM and SF1 cannot provide sufficiently high production rates without stimulation in tight- and shale-gas reservoirs because of very low permeability. Obviously, all other factors being equal, production is maximized when the cumulative surface area of SF1, SF2, SF3 and SF4 is maximized.

Fractured Media Types

Following Moridis *et al* (2010) and Freeman *et al* (2013), there are four possible types of producing tight- or shale-gas reservoir systems. These are depicted in the four panels of Figure II.1.1 (all of which involve a horizontal well configuration and assume full fracture penetration), and are listed below in order of increasing complexity:

(1) Type I: In its most basic form, it comprises (a) the unfractured matrix (Subdomain SM) and (b) the hydraulic fractures HF in SF2. This is the simplest and least productive system, as it is characterized by the minimum surface area and flow pathways for path production. Type I is possible to include the RF (SF4 subdomain).

(2) Type II: Unlike Type I, Type II systems feature the SF3 subdomain and SF. This is expected to yield higher gas production because of increased surface area and more pathways to flow.

(3) Type III: The difference between Type I and Type III systems is the occurrence of the native fractures (NF) in SF1. Such a system is expected to have higher gas production than Type I systems. Comparison of its productivity to Type II is not straightforward, because production is controlled by the characteristics of the fractures, and the relative contributions of NF and SF cannot be determined *a priori* (Freeman *et al*, 2013)

(4) Type IV: This system involves all 5 subdomains (SM to SF4) and all fracture types (NF, PF, SF and RF). This is the most complex system to describe, simulate and analyze. Freeman *et al* (2013) showed that this type has the highest production potential because of its maximum (compared to the other types) surface area and the largest number of flow pathways to the production well.

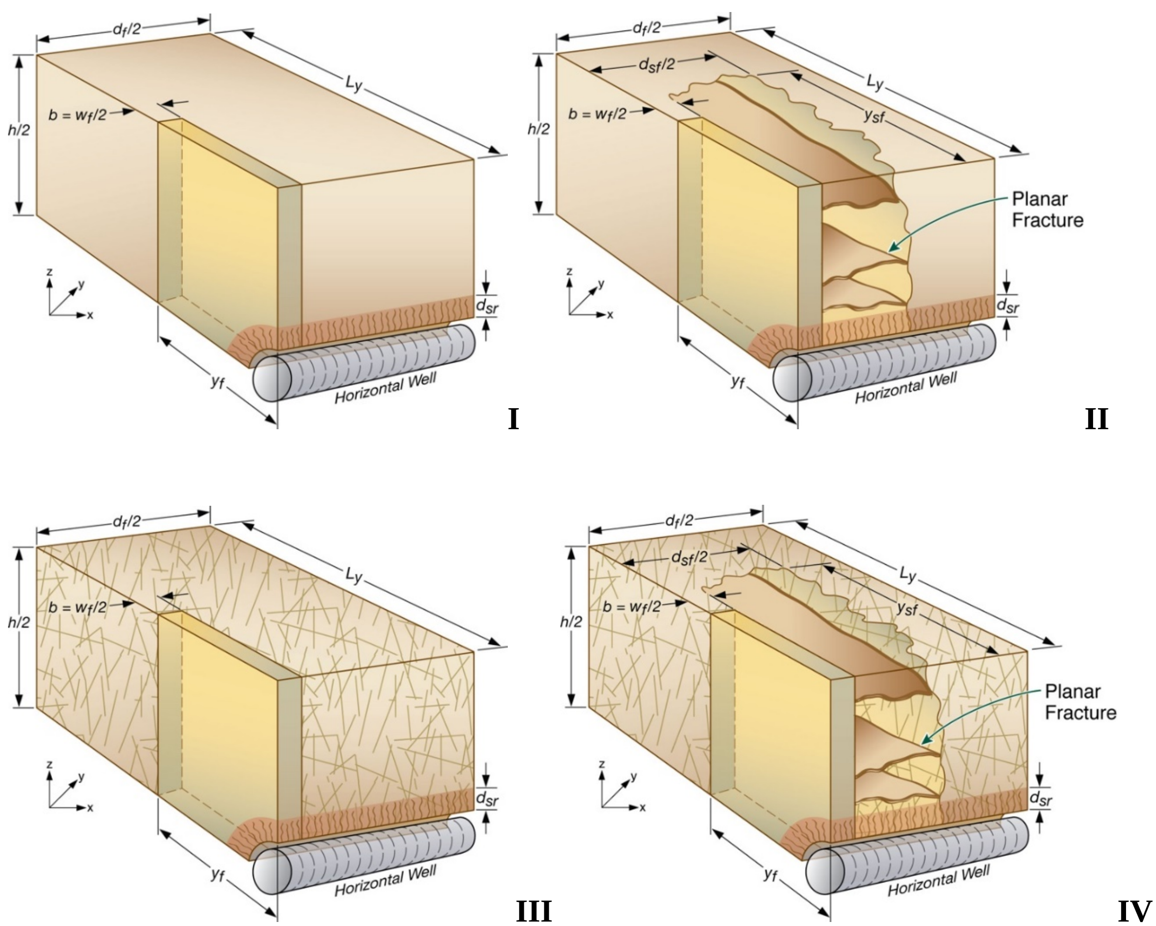

Figure II.1.1: Clockwise: Stencils of Types I with a hydraulic fracture), II (hydraulic fracture and stress release fractures), III (hydraulic fracture and native/natural fractures) and IV (all types of fractures) fractured systems involving a horizontal well in a ULP reservoir (Moridis et al., 2010).

Note that Figure II.1.1 describes the basic stencils of the four types, i.e., the smallest possible repeatable or repetitive element (fraction of the domain) that is necessary and sufficient to fully characterize the system and describe its behavior during production. Implicit in the selection of these stencils are the assumptions of (a) symmetry about the vertical plane that passes by the horizontal well centerline (indicating an assumption of homogeneous property distributions), (b) symmetry about the horizontal plane that passes by the centerline of the well, indicating an assumption of minimal gravitational effects in the overall system performance (a reasonable approximation in deep, thin reservoirs), and (b) negligible tow-to-heel pressure differences during production (a valid approximation in relatively short horizontal wells). Reservoirs with mobile multi-phase saturations (as is the case in our studies) necessitate accounting for gravitational effects (especially at higher pressures), in which case the symmetric lower half of the stencil/domain (i.e., that below the horizontal plane at z = 0) needs to be included in the analysis.

Evaluation of enhanced liquids recovery using displacement processes

In this task we evaluated by means of numerical simulation (involving the TOUGH+ family of codes developed at LBNL) "standard" fluid recovery strategies from ULP formations involving displacement processes, accounting for all known system interactions. The initial intent was that these studies would include (a) traditional continuous gas flooding using parallel horizontal wells and using the currently abundant shale gas, (b) water-alternating-gas (WAG) flooding, and (c) huff-and-puff injection/production strategies using lean gas/rich gas in a traditional (single) horizontal well with multiple fractures.

Note that although there were low performance expectations in some of these strategies, we still evaluated these techniques thoroughly for the sake of completeness. This, early scoping calculations indicated the lack of any potential of the WAG approach because of (a) the extremely low permeability of the system especially beyond the stimulated region, and (b) the reduced permeability following the water injection stage, which resulted in very high pressures (even for low injection rates) that easily exceeded the mechanical strength of the rock and could lead to fracturing of the overburden with unintended (and universally negative consequences).

The bulk of the effort focused on continuous gas flooding because it became evident at an early stage that the associated simulations were much more demanding and time consuming that originally expected. This was caused by the realization that the extremely sharp saturation fronts (during displacement gas injection or gas exsolution) and pressure fronts -- a consequence of the micro- to nano-level permeability of the matrix in the ULP formations of interest in shale oil reservoirs -- could only be resolved with mm-scale spatial discretizations in the vicinity of the production points (e.g., the hydraulic fractures). This led to a very large number of elements in the 3D simulation grids, long execution times and a lengthy effort for the analysis of the simulation results, thus draining the (limited) funds that had been designated for the simulation efforts and preventing the study of processes such as huff-and-huff. Note that the importance of the results of the laboratory studies associated with this project (which yielded exciting new insights and information on the process of fluid production from ULP reservoir) was so high that not only prevented the internal reallocation of funding to support further simulation studies but instead necessitated allocating more resources to the laboratory component of the project.

The work of Olorode (2012) has clearly indicated that a study using stencils is fully representative of the fluid production and of the overall system behavior from the entire horizontal well system over very long periods. Thus, our numerical simulation studies concentrated on the analysis of production from 3D stencils, the fine discretization of which resulted in grids comprised of 100,000s of elements. The dimensions of the stencil used in this study, as well as information on the size of the grid, are presented in Figures II.1.2 and II.1.3. *Note that the hydraulic fracture extended only 5 m into the matrix along the y-direction (and did not cover the entire length of the* *y-coordinate) because scoping calculations revealed that long hydraulic fractures were not especially productive due to diversion of a large portion of the injected gas into the hydraulic fracture (i.e., along the path of least resistance), which short-circuited the displacement process and the recovery of oil.*

Using properties and conditions that are typical of the Eagle Ford, Niobrara and Bakken formation (Table II.1.1), we investigated continuous displacement processes using N_2, CH_4, CO_2 and He as the displacement gases using parallel horizontal wells. Note that the gas drives using CH_4 and CO_2 were not pure displacement processes because they incorporated the physical-chemical effects of changes in the thermophysical properties (mainly viscosity) caused by the gas dissolution in the oil. Baseline data were provided by two reference cases: one involving a hydraulically-fractured system (Type I), and another one with an un-fractured ("virgin") rock. The discretized Type I stencil comprised 370,000 elements, resulting in a total of 1,110,000 simultaneous equations when the simulations were conducted isothermally (and 1,480,000 equations in non-isothermal simulations).

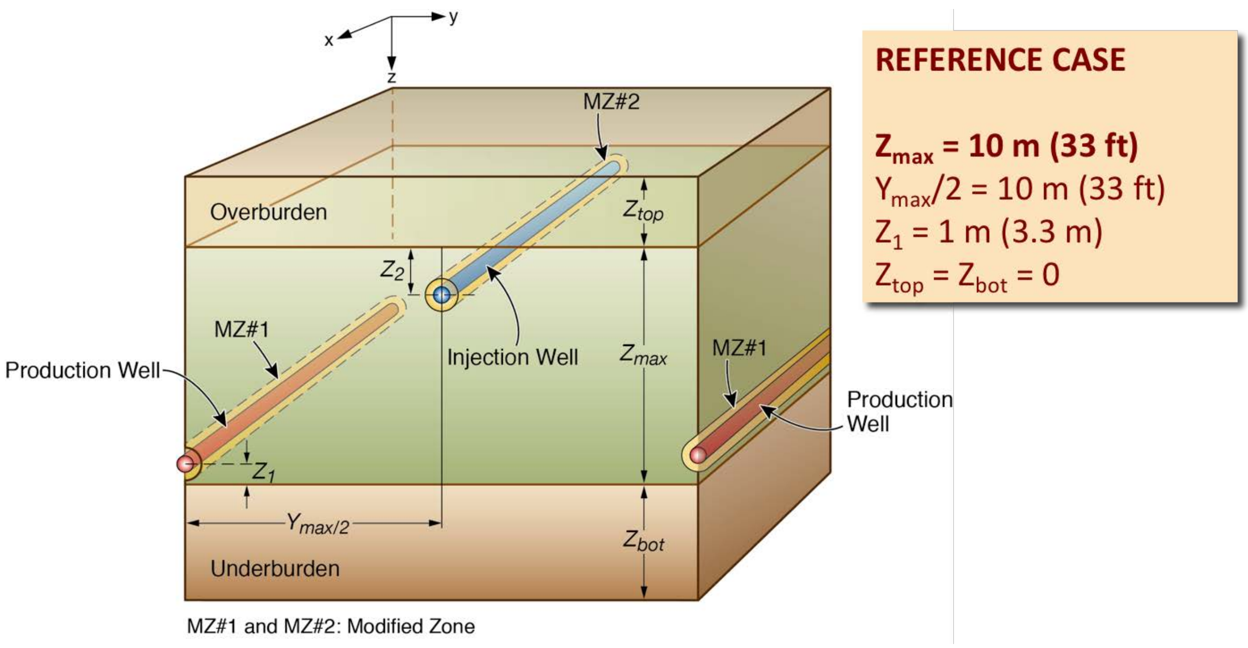

Figure II.1.2: Detailed stencil of the ULP reservoir used in the simulation –View A.

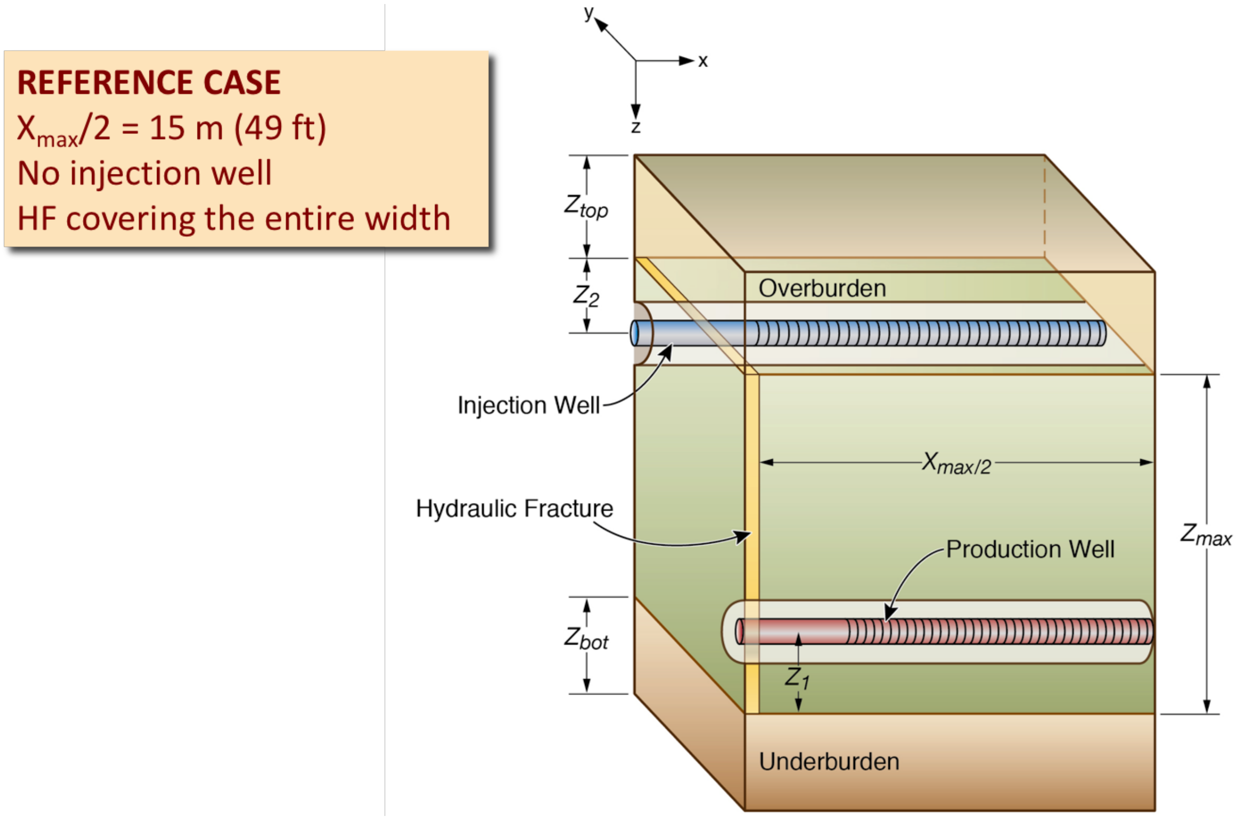

Figure II.1.3: Detailed stencil of the ULP reservoir used in the simulation –View B.

The sensitivity analysis in the simulation of the displacement-based recovery for the ULP reservoir addressed the effects of the following conditions and parameters:

(a) Matrix permeability, covering the range from 10 nD to 1 μD
(b) Presence of hydraulic fractures
(c) Presence of natural fractures
(d) Dissolved gas (dead vs. live oil)
(e) Various displacement gases

Figures II.1.4 and II.1.5 show the evolution of the production rate over time and the cumulative production of *dead light oil* (with the properties of n-octane) from an 1800-m long horizontal well in the two base (reference) cases. The beneficial effect of the hydraulic fracture is evident, especially in the critically important (from the point of view of economic importance) period of early production: the presence of the hydraulic fracture significantly increases the early production rate. Given the fact the amount of oil is finite and fixed in each stencil (limited by the stencil dimensions, as defined by the reservoir thickness, the HF spacing and the horizontal well spacing), there is cross-over point when the production rate from the unfractured system exceeds that of the fractured system at later times. The results in Figures II.1.4 and II.1.5 also depict the importance of the matrix permeability: the early oil production rate increases with an increasing matrix permeability.

Table II.1.1 – Properties and conditions of the reference case (Type I)	
Parameter	**Value**
Initial pressure P	2.00×10^7 Pa (2900 psi)
Initial temperature T	60 °C
Bottomhole pressure P_w	1.00×10^7 Pa (1450 psia)
Oil composition	100% n-Octane
Initial saturations in the domain	$S_O = 0.7$, $S_A = 0.3$
Intrinsic matrix permeability $k_x=k_y=k_z$	10^{-18}, 10^{-19}, 10^{-20} m^2 (=1000, 100, 10 nD)
Matrix porosity ϕ	0.05
Fracture spacing x_f	30 m
Fracture aperture w_f	0.001 m
Fracture porosity ϕ_f	0.60
Formation height	10 m
Well elevation above reservoir base	1 m
Well length	1800 m (5900 ft)
Heating well temperature T_H	95 °C
Grain density ρ_R	2600 kg/m^3
Dry thermal conductivity $k_{\Theta RD}$	0.5 W/m/K
Wet thermal conductivity $k_{\Theta RW}$	3.1 W/m/K
Composite thermal conductivity model[16]	$k_{\Theta C} = k_{\Theta RD} + (S_A^{1/2}+S_H^{1/2})(k_{\Theta RW} - k_{\Theta RD})$
Capillary pressure model[14,23]	$P_{cap} = -P_0\left[\left(S^*\right)^{-1/\lambda}-1\right]^{-\lambda}$ $S^* = \frac{(S_A - S_{irA})}{(S_{mxA} - S_{irA})}$
S_{irA}	1
λ	0.45
P_0	2×10^5 Pa
Relative permeability Model[17]	$k_{rO} = (S_O^*)^n$ $k_{rG} = (S_G^*)^n$ $S_O^*=(S_O-S_{irO})/(1-S_{irA})$ $S_G^*=(S_G-S_{irG})/(1-S_{irA})$ EPM model
n	4
S_{irO}	0.20
S_{irA}	0.60

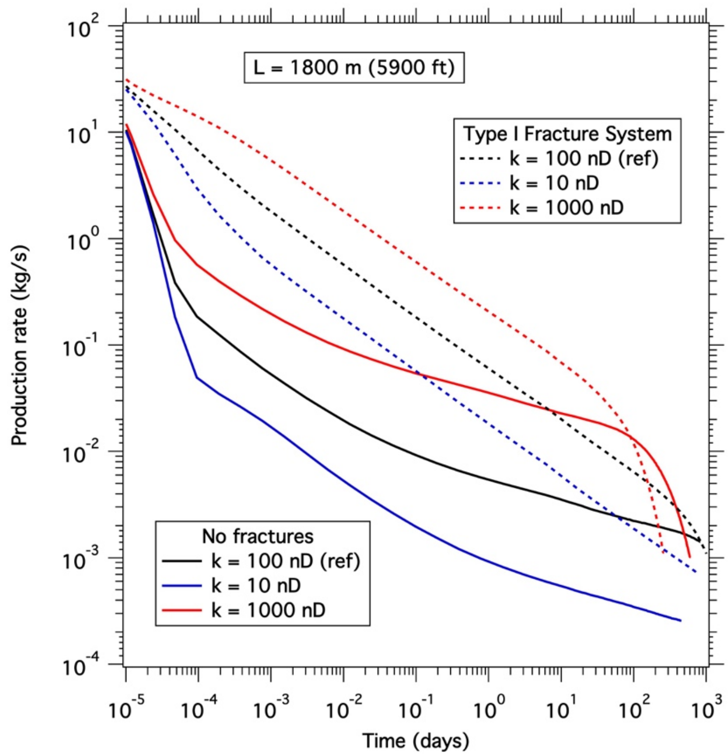

Figure II.1.4: Performance of the reference Cases R (unfractured) and RF (fractured), and effect of matrix permeability on the rate of oil mass production Q.

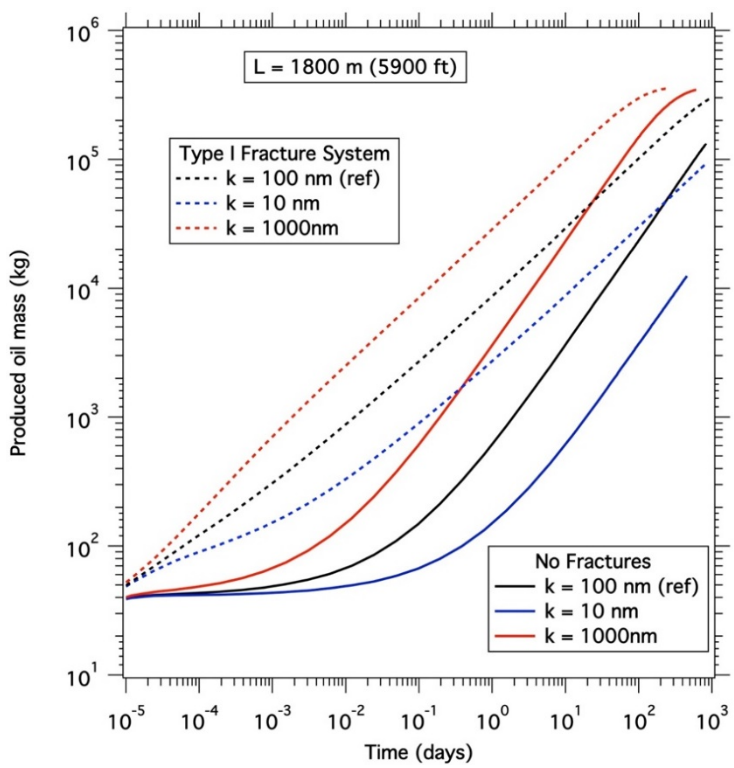

Figure II.1.5: Performance of the reference Cases R (unfractured) and RF (fractured), and effect of matrix permeability on the cumulative mass of produced oil.

The effect of dissolved gas is evident in Figure II.1.6, which shows that, for a given matrix permeability, early recovery increases (significantly) in the case of gas dissolved in the oil (live vs. dead oil). For this study, we used conditions and properties that are representative of the gas-oil ratio in the Bakken reservoir: a GOR of 1000 SCF/bbl, and a bubble point of 185 bars. This pattern is consistent for all matrix permeabilities.

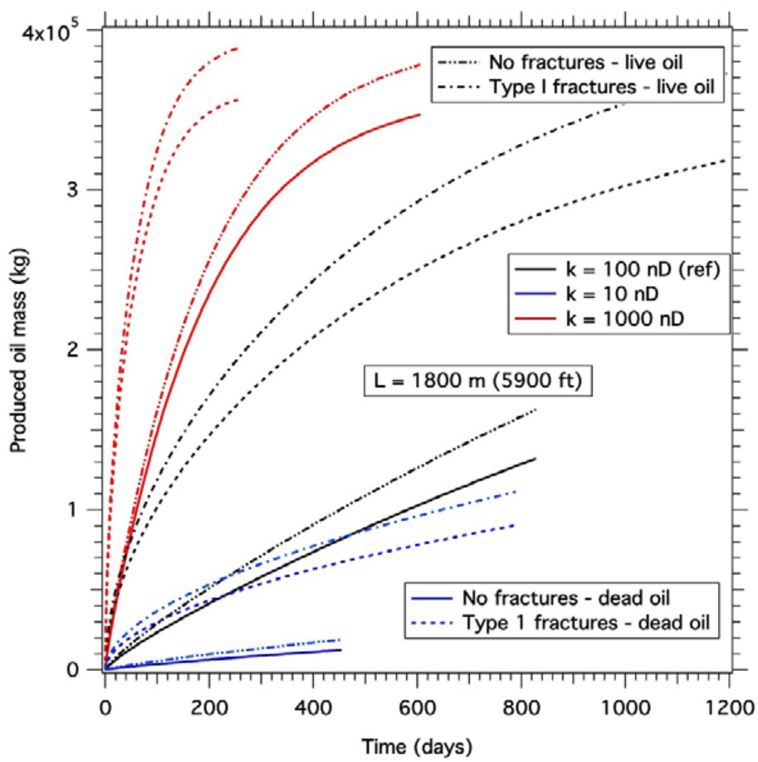

Figure II.1.6: Effect of (a) the presence of a hydraulic fracture, (b) matrix permeability and (c) dissolved gas (gassy/live vs. dead oil) on the cumulative mass of produced oil.

The performance of two different gases (CH_4 and N_2) in displacement-based recovery processes (gas drives) is presented in Figure II.1.7 and shows the superiority of CH_4 because of its superior solubility in oil and its consequent effect on the oil viscosity and (to a lesser extent) on density. Note the difference in the production pattern between the fractured and the unfractured system: there is a late "surge" in oil production in the unfractured system, which is attributed to delays caused by the difficulty in the diffusion of the gases through the displaced "bank" of oil to reach virgin shale oil. The improvement in recovery in the case of the fractured system is almost immediate in the CH_4 drive in the fractured system, and much slower in the N_2 drive. It is important to indicate that the numerical simulations indicated near-identical production performance for both N_2 and He gas drives. However, these results are not included in Figure II.1.7 because they were in sharp disagreement/contrast with the corresponding laboratory results conducted in this project, which indicated no enhancement of production as a result of the He gas drive (attributed to tunneling of the very small He molecules through the shale system, thus bypassing the oil and effecting no displacement).

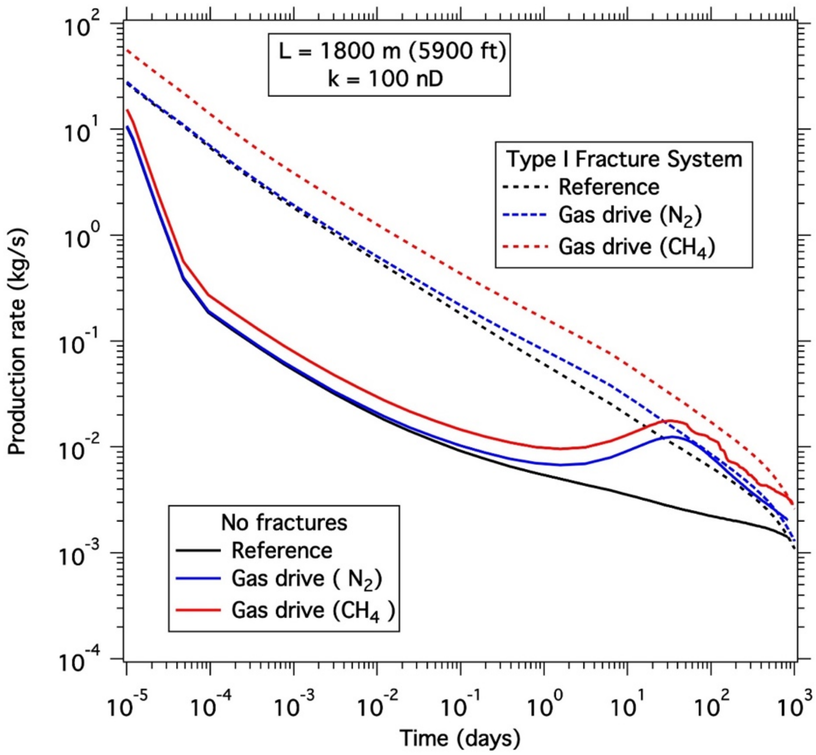

Figure II.1.7: Effect of (a) hydraulic fracture and (b) the displacement process (gas drive using CH_4 and N_2) on Q.

The performance of the CO_2-based displacement in the oil recovery process is depicted in Figures II.1.8 through II.1.10, which show the superiority of the CO_2 drive. The enhancement of production spans the entire spectrum investigated thus far. Recovery improves with an increasing matrix permeability, in hydraulically-fractured media and in live oil: the highest early production rate is observed for live oil in the hydraulically-fractured reservoir with the highest permeability matrix. The superiority of CO_2 over CH_4 as a displacement gas is illustrated in Figure II.1.11 and is attributed to the much higher solubility of CO_2 in the oil and the resulting significant decrease in the oil viscosity.

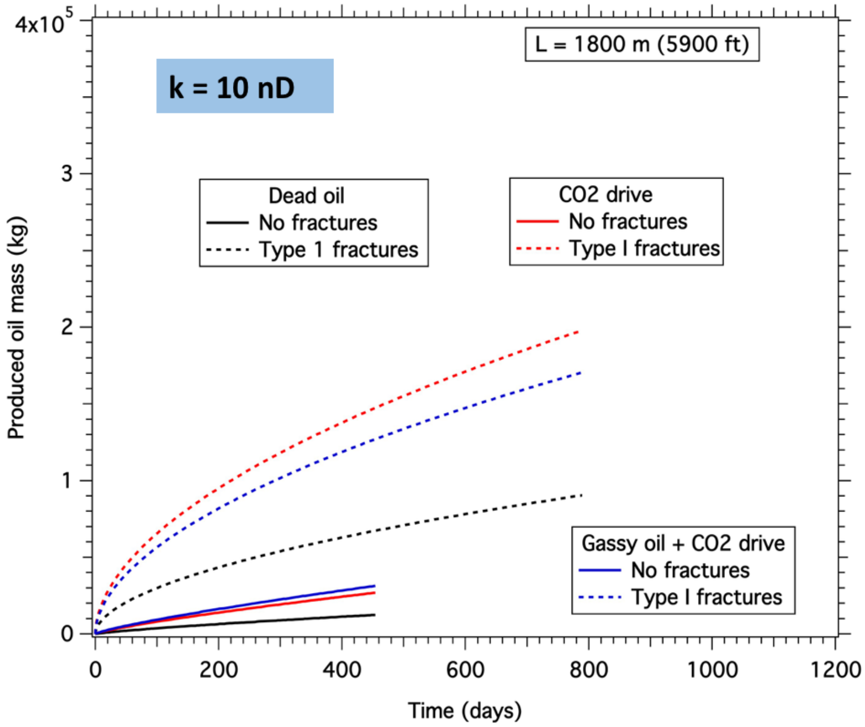

Figure II.1.8: Effect of (a) gassy (live) vs. dead oil and (b) displacement by CO_2 on cumulative oil production from a shale oil reservoir with Type I fractures and a matrix permeability of 10 nD.

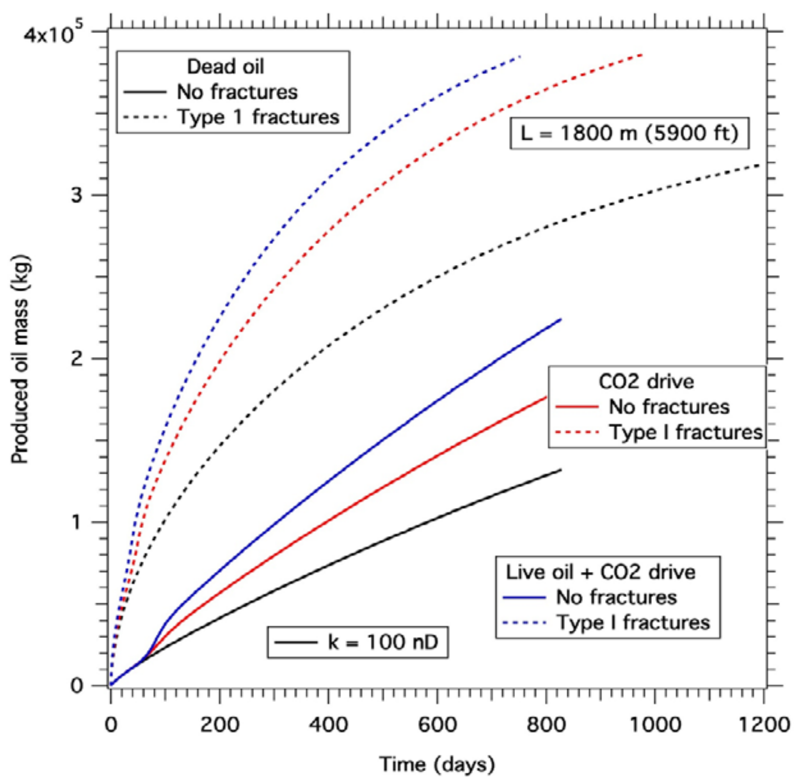

Figure II.1.9: Effect of (a) gassy (live) vs. dead oil and (b) displacement by CO_2 on cumulative oil production from a shale oil reservoir with Type I fractures and a matrix permeability of 100 nD.

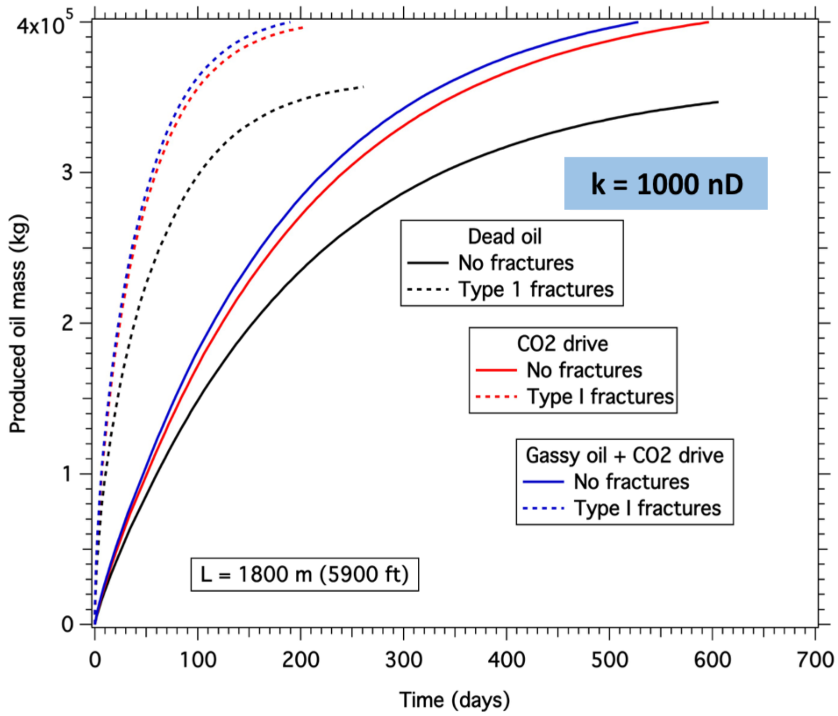

Figure II.1.10: Effect of (a) gassy (live) vs. dead oil and (b) displacement by CO_2 on cumulative oil production from a shale oil reservoir with Type I fractures and a matrix permeability of 1000 nD.

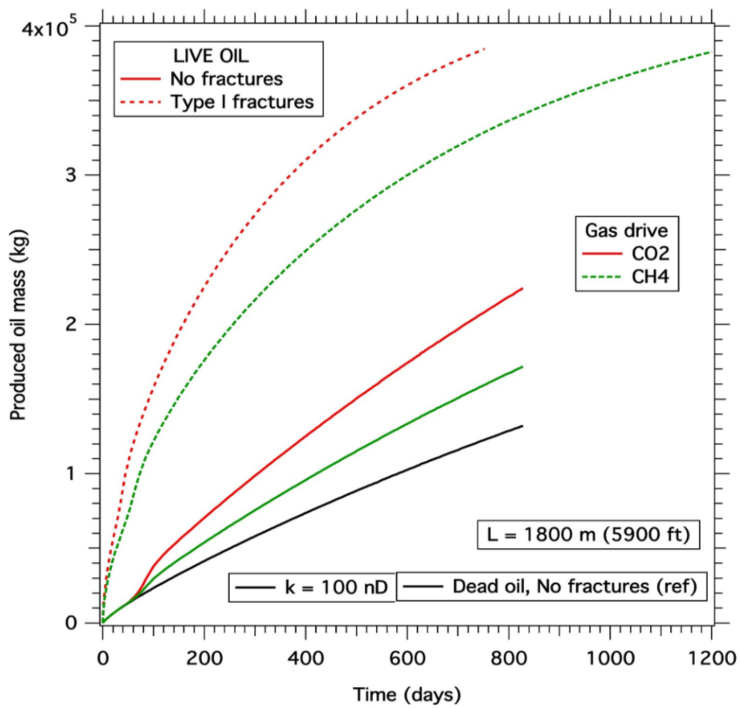

Figure II.1.11: Relative effectiveness of CH_4- vs CO_2-gas drives, as described by the associated cumulative oil productions from a Type I fractured shale oil reservoir with a matrix permeability of 100 nD.

The impact of natural fractures on production from ULP reservoirs is shown in Figure II.1.12. In terms of simulation, the significant natural fracture network was described by Type III fractured domain (see Figure II.1.1) that comprised 740,000 elements, resulting in a total of 2,220,000 simultaneous equations when the simulations were conducted isothermally (and 2,960,000 equations in non-isothermal simulations). The simulation results in Figure II.1.12, as well as those in Figures II.1.4 to II.1.10, provide solid evidence that the occurrence of fractures (both natural and hydraulically induced) are by far the most dominant factor affecting production from ULP reservoirs: extensive fracture networks are associated with higher early production rates and higher ultimate recoveries.

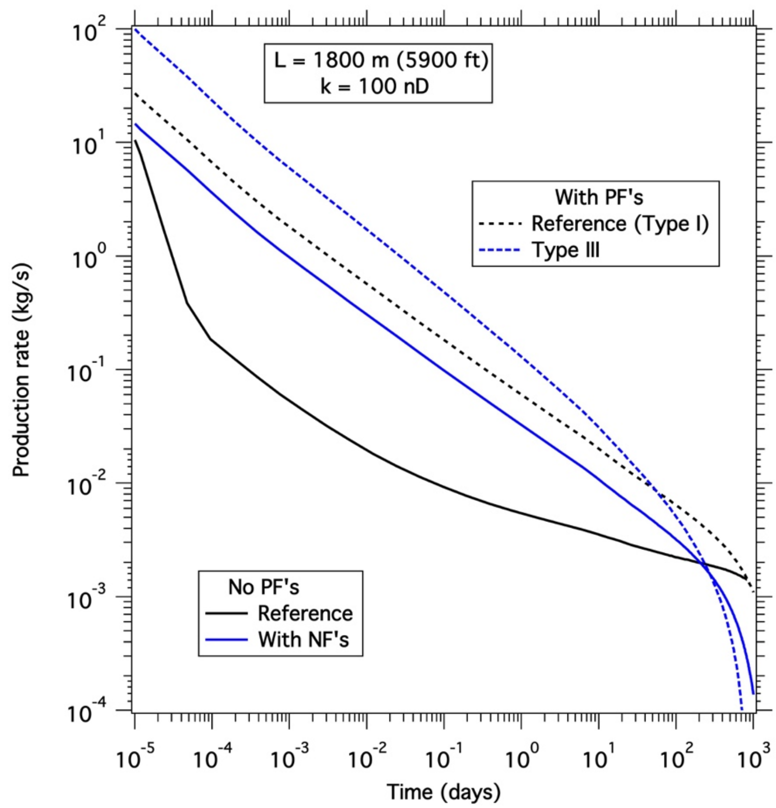

Figure II.1.12: Effect of (a) the hydraulic fracture and (b) the presence of native fractures (NF) fractures on Q. The presence of fractures has the most pronounced positive effect on production.

Evaluation of enhanced liquids recovery by means of viscosity reduction

It can be argued that CH_4- and CO_2-gas drives are (at least partially) viscosity-reducing methods for enhanced oil production (a consequence of the gas dissolution into the oil), as the increase in production is not just the result of oil displacement by the invading gas. Conversely, thermal methods are strategies for enhanced oil production based on pure viscosity-reduction. In the simulations, the thermal effect was realized by the flow of hot fluids flowing through non-perforated horizontal wells parallel to the actual production wells. This configuration allows hear exchange between the thermal well and the ULP formation without any fluid flow into the formation.

The results in Figure II.1.13 indicate the limited effectiveness of pure thermal methods as a means of oil production enhancement strategies. Two cases were investigated: Case RF-H1 involved heat flow through the parallel horizontal "thermal" well that began at the time of the onset of fluid production. In Case RF-H2, heating began 3 months before the beginning of production, thus allowing much more time for heat to cause a reduction in the oil viscosity and a corresponding increase in production. The results in Figure II.1.13 indicate that there is an overall increase in production, but this is not significant in Case RF-H1 and occurs after a significant lead time. As expected, early heating (Case RF-H2) is more effective in increasing production than heating that begins at the time of the initiation of production (Case RF-H1), and the early increase in production can be significant. However, this increase in production has to be evaluated against the significant energy requirements of months of continuous heat injection through the thermal well in order the raise the temperature of the low-porosity, high-heat-capacity, low-thermal-conductivity shale system, considering that the dominant heat transport mechanism in shales is the slow mechanism heat conduction.

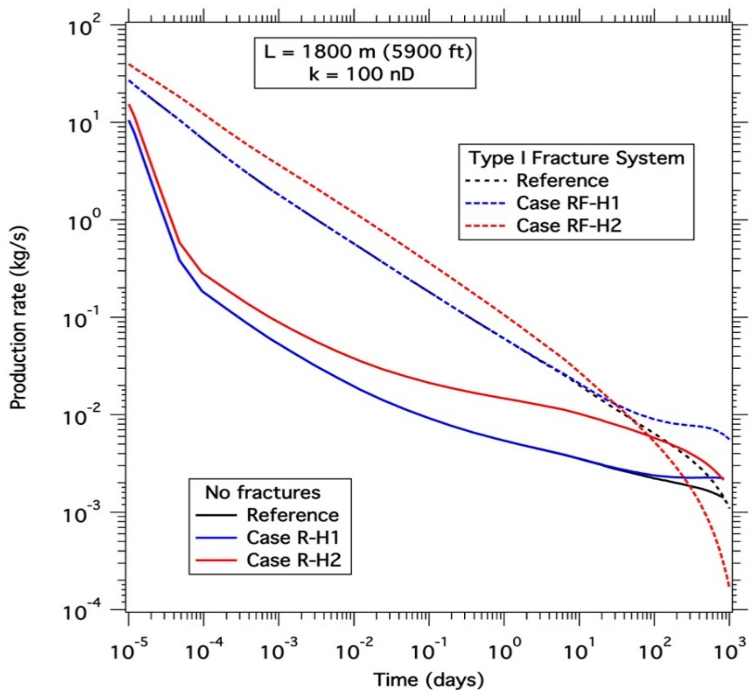

Figure II.1.13: Effect of (a) the hydraulic fracture and (b) of the heating regime on Q. Case RF-H1 corresponds heating beginning at the onset of production. Heating in Case RF-H2 begins 3 months before the initiation of oil production.

Phase II, Task 3: 3D Analysis and Modeling of the Transport and Long-Term Fate of Proppants

October 1, 2016-September 30, 2018

Subtask II.2: Development of Proppant Simulation Methodologies

The behavior of proppant transport at the reservoir scale and at the proppant scale requires different numerical methods, as capturing small scale dynamics inside of fractures are intractable at the reservoir scale. New numerical techniques were developed to create predictive models. Work focused on developing two techniques at these two scales to improve upon three main aspects of the fracture transport problem:

- fluid lag behind the fracture tip during the fracturing process,
- two-way coupled proppant transport inside of the fracturing fluid,
- flow of fluid and proppants through intersections of fractures (branches).

We have implemented a finite element formulation for capturing some of these properties at the reservoir scale, and have implemented a prototype framework for automatically upscaling these relations from proppant-scale simulation.

We also extended previous work on fracture propagation and deformation that evaluated the numerical properties peridynamics. We have accomplished the following tasks to date:

- Developed an analytical model for particle-laden thin-film flow.
- Implement the partial differential equations in a Finite Element simulation using a level set representation for the fluid front and fracture tip.
- Implemented a microscale simulation of fully meshed proppants at fracture branches (Figure 1).
- Deployed a coupled flow-proppant transport code to test the model and generate the preliminary results.

Reservoir Scale

The disparate length scales of the proppants and fracture thickness with respect to the fracture network within the entire reservoir demands a simplification at the reservoir scale. In BP #1, we developed, from first principles, a 2D/3D numerical model of fluid flow and accompanying proppant transport. This numerical model has been implemented as a finite-element code coupled to our in-house geomechanical simulator, and preliminary simulations have demonstrated the ability to represent the moving fluid front and transport of proppants in vertical and horizontal fractures.

A thin-film flow assumption is used to reduce the fracture network to 2D fractures embedded in the 3D rock matrix. The momentum and mass conservation equations for the fluid phase and proppant phase are formulated on the fracture plane. To address the fluid lag problem, the level set method is used to represent the boundary between the injected fluid and the *in situ* fluid present in the fracture. The equations are discretized on a 2D mesh using a Petrov-Galerkin Finite Element discretization using FEniCS and integrated in time high order implicit Runge-Kutta methods.

A new partial-differential equation (PDE) extending the Reynolds lubrication equation to particle-laden flow has been derived. The formulation is based upon the thin-film laminar flow assumption from lubrication theory assuming a uniform distribution of proppants exhibiting Stokes drag, simplifying the 3D equations to a 2D fracture domain. Fluid lag behind the fracture tip is represented using a level-set representation of the fluid front. The primary variables of the newly developed model are fluid pressure, the fluid level set, proppant number density and proppant flux. A prototype Petrov-Galerkin finite element model for the level-set based fluid infiltration into a fracture was implemented using the open source finite element package FEniCS. The additional components to the PDE are being implemented in the FEniCS model.

Computational analyses and numerical experiments have determined that it is necessary to solve fracture deformation and fracture flow fields in a monolithic scheme (with one Jacobian tangent matrix containing the fluid pressures and mechanical deformation). This greatly complicates the implementation of these models in existing reservoir simulations such as TOUGH+ and requires intensive software development.

In the next project, the code development work will continue with the goal of coupling the proppant-transport model into the TOUGH+MCP modeling framework. This coupled thermo-hydrological-mechanical code will be used to perform simulations of fracture propagation and proppant transport in hydraulic fracturing operations, and determine the fate of proppants for a range of reservoir properties and injection scenarios.

The fracture fluid and proppant transport model is designed to be easily coupled with other fracture propagation models, which is an open topic meriting future research. This has provided the impetus for the level set based approach to represent fluid lag and the fracture boundary, which we foresee to be extendable in the future to fracture propagation.

An important factor in the transport of proppants is flow through fracture branches. For example, a crucial instance is where the primary hydraulic fracture intersects a preexisting natural fracture. The problem of fracture branches poses a further challenge where analytical relations will be difficult to obtain. Constructing an analytical solution for the flow through the branches---relating inlet and outlet velocities and pressures as parameterized by the fracture thicknesses and their intersecting angle---is probably possible for a single-phase fluid, but the matter is greatly complicated by the proppant phase, where the behavior extends to the proppant densities and velocities (Figure II.2.1).

This motivated research into microscale simulations and novel upscaling techniques and discretizations for two reasons:

fracture branches do not fit in with a purely partial differential equation approach

the assumptions required to find a closed-form analytical solution to the proppant-laden thin film flow do not hold in the fractured systems typical of reservoirs.

Proppant scale

We turned to focus on the proppant-scale transport behavior upscaling. We have developed prototype tools built on top of TensorFlow to train various models on generated microscale simulation databases and then differentiate and load the trained models into existing scientific codes. The progress is documented in:

https://github.com/afqueiruga/afqstensorflowexamples

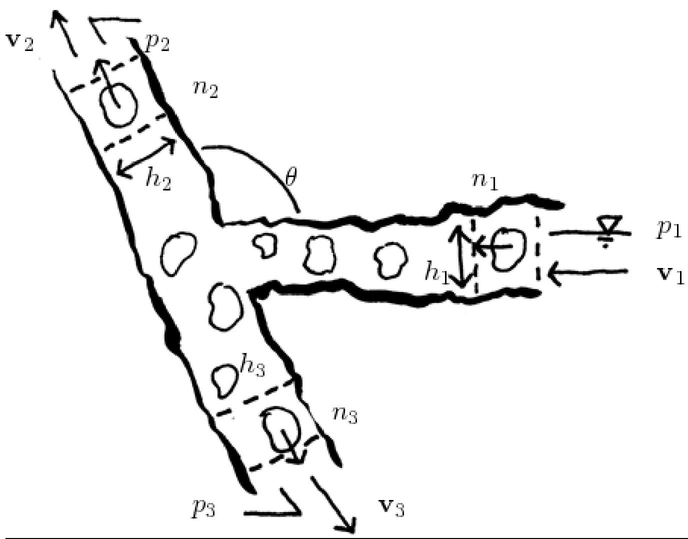

Figure II.2.1: Schematic of complex multiphase flow conditions at a fracture branch. An empirical relation or learned model is needed to relate the flow fields as parameterized by the geometry of the branch.

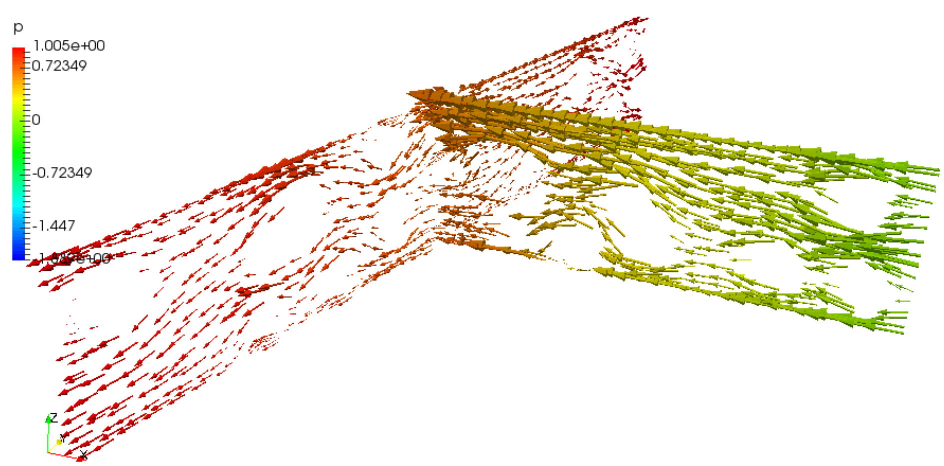

Figure II.2.2: A microscale simulation of fluid flow through a segment of a branch with proppants following the specification of the schematic in Figure 1. These simulations are sampled for random distributions of proppants at different proppant densities and fracture geometries to build the dataset needed for upscaled relations at branches.

We experimented with using FEniCS and TensorFlow (open-source platforms) to perform finite-element simulation of Stokes flow around proppants, developing code to automatically mesh randomly generated distributions of proppant particles with differing densities and fracture heights. These automated ensembles may be used to create reduced-order models to inform both simulation and lab work involving proppant transport.

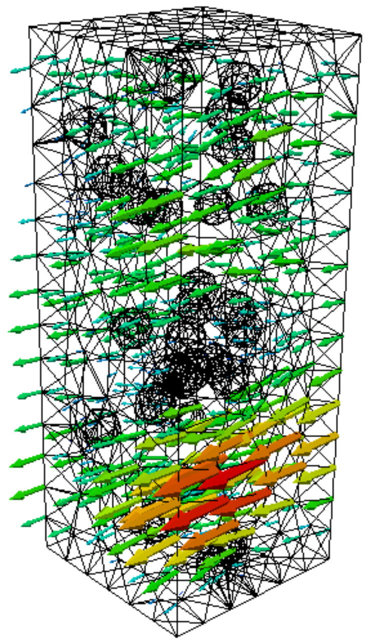

Figure II.2.3: Realization of flow around one possible configuration of proppants in a fracture.

To increase the fidelity of the upscaling efforts, we are developing a coupled particle and flow simulation, wherein the motion of the particles is calculated using the discrete element method and the Navier-Stokes equations are solved by the finite element method. The generally applicable library for performing particle-finite element interaction calculations with the open source FEniCS package that was developed as part of this effort is released open source at:

https://github.com/afqueiruga/FEniCS_Particles

The simulation will be used to determine proppant distributions as they flow through different geometries branching fractures. The data generated by the simulation will then be used to train reduced order models that can be used to incorporate the multiphase flow properties at branches in large scale simulations of fracture networks.

Peridynamics

As part of our ongoing work on studying numerical methods for fracture propagation—a critical aspect to fracture transport—a new code base was written to analyze and demonstrate the properties of Peridynamics. The code was released open source at:

https://github.com/afqueiruga/PeriFlakes

An open source database of reference problem solutions with various Peridynamics formulations was published with this code base and is publicly available on Zenodo:

Alejandro Francisco Queiruga. (2018). 2D Peridynamic Displacement Fields [Data set]. Zenodo. http://doi.org/10.5281/zenodo.1284634

New developments that attempt to address the issues with Peridynamics were incorporated into the code and evaluated. Our studies have shown that Peridynamics is an unsuitable numerical method due to its inability to represent expected mechanics solutions. Exhaustive searches generated using Periflakes have failed to find a boundary condition method or smoothing method that recovers this flaw. Two invited talks were given at the World Congress of Computational Mechanics and the U.S. National Congress for Theoretical and Applied Mechanics presenting these findings.

The following presentations were made as part of this work.

Queiruga, A. F. and G. J. Moridis, “Numerical experiments on the convergence properties of state-based peridynamic laws and influence functions in two-dimensional problems,” World Congress of Computational Mechanics, New York City, New York, July 2018.

Queiruga, A. F. and G. J. Moridis, “Smoothing Methods to Address the Numerical Stability of Peridynamics Near the Fracture Tip in Hydraulic Extension,” 18th U.S. National Congress for Theoretical and Applied Mechanics, Rosemont, Illinois, June 2018.

PART III

LABORATORY AND VISUALIZATION TASKS

Phase I, Task 5: Multi-scale laboratory studies of system interactions

October 1, 2014-September 30, 2016

Phase II, Task 4: Multi-scale laboratory studies of system interactions

October 1, 2016-September 30, 2018

These tasks followed two lines of investigation, as divided into two subtasks: 1) sub-micro-scale visualization studies and 2) laboratory studies of light tight oil production techniques.

Subtask III.1: Sub-Microscopic-Scale Visualization Studies

Section III.1.1: Interaction of fractured Niobrara Shale with CO_2-bearing fluids

Objectives:

- Comprehensive characterization of the Niobrara Shale, to provide quantitative information for models, to predict the possible evolution patterns of the rock under different conditions, and to provide a first insight to help choosing the best approaches for oil recovery.
- Use of 4D synchrotron X-ray microCT to better understand selected processes related to oil production techniques from tight shales at the µm resolution, at ~reservoir conditions.

Characterization of the Matrix Properties in the Niobrara Shale

Within the laboratory investigation team associated with this project, we worked on a common set of natural geologic samples obtained from the Niobrara formation, an extensive shale oil target in the Denver Basin and beyond. The samples in question were quarried from an oil-bearing horizon of the Niobrara and LBNL was provided with a large block for project experimental purposes. While not fully representative of a single reservoir, quarried samples are attractive in that multiple large samples can be easily fabricated from a single block, presumably with similar properties, allowing parallel experimental efforts. However, due to the heterogeneity of the Niobrara formation, extensive characterization was required to provide a context for further experimental work.

Upon receiving initial samples from the Niobrara formation, we embarked on a comprehensive characterization study to inform the next set of in situ micro-imaging and core-flood experiments. The combination of electron microscopy, X-ray diffraction, and X-ray microCT, and provides a dataset including the mineralogy, chemical composition, and, texture/microstructure present in the sample. For the scanning electron microscopy (SEM) characterization two type of samples were prepared:

1) Sample broken along the cleavage plane, subparallel to the bedding. This allows the morphological characterization of the phases and the planar features (SE imaging) of an undisturbed surface.

2) Samples with a face cut and polished ~perpendicular to the bedding plane. This allows a better characterization of the microstructure/texture, better BSE images, and more reliable energy dispersive spectroscopy (EDS) analysis.

The x-ray powder diffraction (XRPD) experiment was carried out on a fragment crushed and pulverized from the same shale block, following a conventional procedure for lab XRPD measurements. The analysis of the XRPD profile was done with the Rietveld method, thus providing quantitative information about the bulk mineralogy, complementing the information obtained with SEM/EDS.

Electron microscopy

The fractured surface shows wavy structures at the tens of μm scale, with clay particles following the direction of these planes. Carbonates-rich structures also follow these planar features.

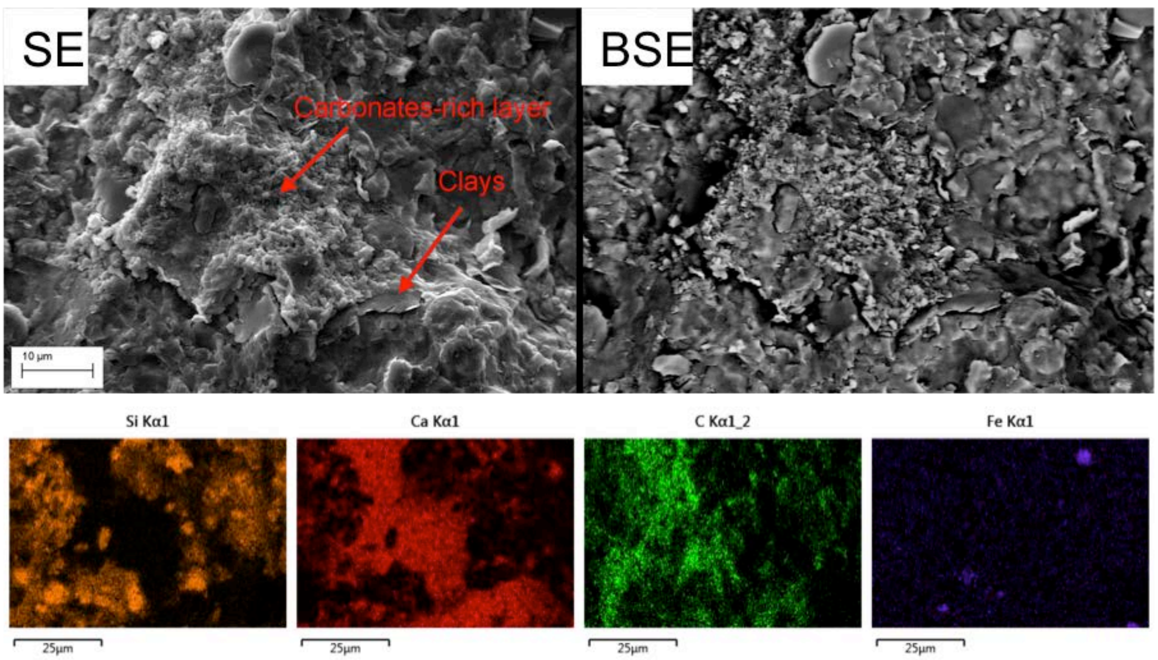

Figure III.1.1: Top: Secondary Electron (SE) and Back Scattered Electron (BSE) images of the fractured Niobrara sample. Bottom: elemental maps of key mineral components showing the distribution of the phases.

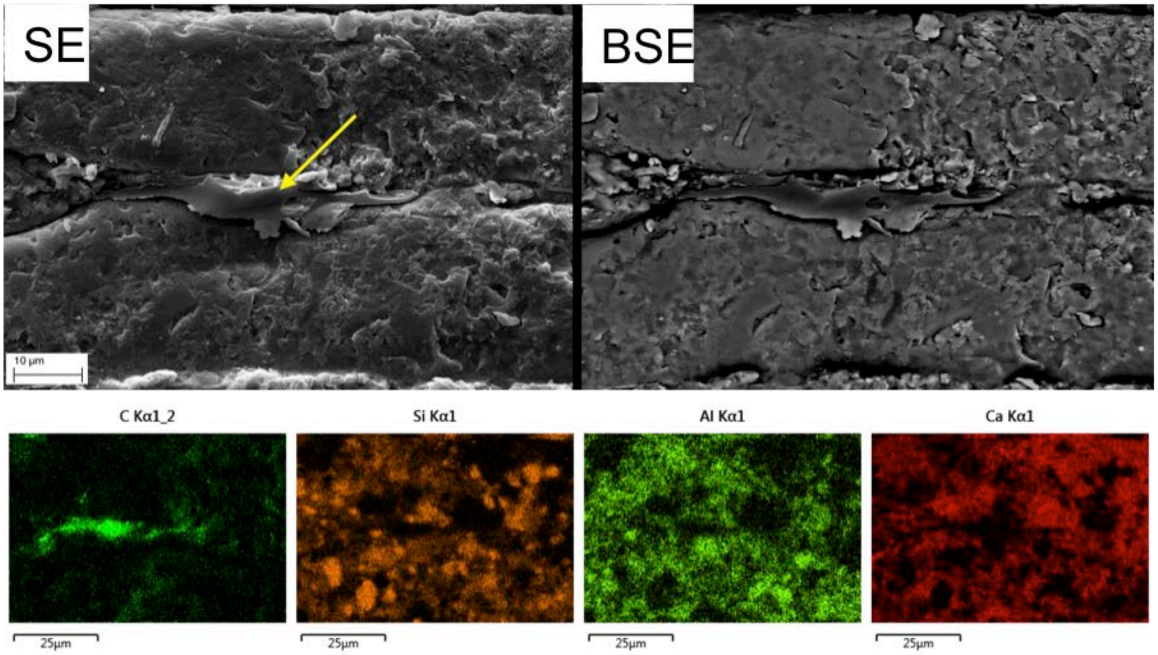

Figure III.1.2: Example of an organic particle (yellow arrow). Top panels are structural images (SE/BSE) while bottom panels include EDS chemical imagery. The EDS maps confirm the carbonaceous composition of the particle.

Organic-rich particles can also be found scattered on the sample surface. An example of an organic fragment can be seen in Figure III.1.2 (top left, yellow arrow) where the particle is found close to what seems to be a clay pseudomorph after feldspar.

The second Niobrara sample was cut and polished on a plane perpendicular to the bedding plane and more accurately captures the layering and textural features of the sample, as can be seen in Figure III.1.3. This particular shale sample has a high carbonate fraction (mainly calcite) and the texture is strongly influenced by carbonate distribution. Carbonate zones are relatively diffuse in the shale, with occasional micrometric lenticular structures enriched in calcite. Some carbonate layering at a larger scale is also present where calcite highlights again small lenticular structures surrounded by clays and quartz. The microporosity seems to be related to the calcite fraction; where calcite is present in larger amounts, the microporosity seems to be low (see BSE images). Some fine cracks healed with (often sparry) calcite are also present. In the figures presented the bedding direction is roughly vertical.

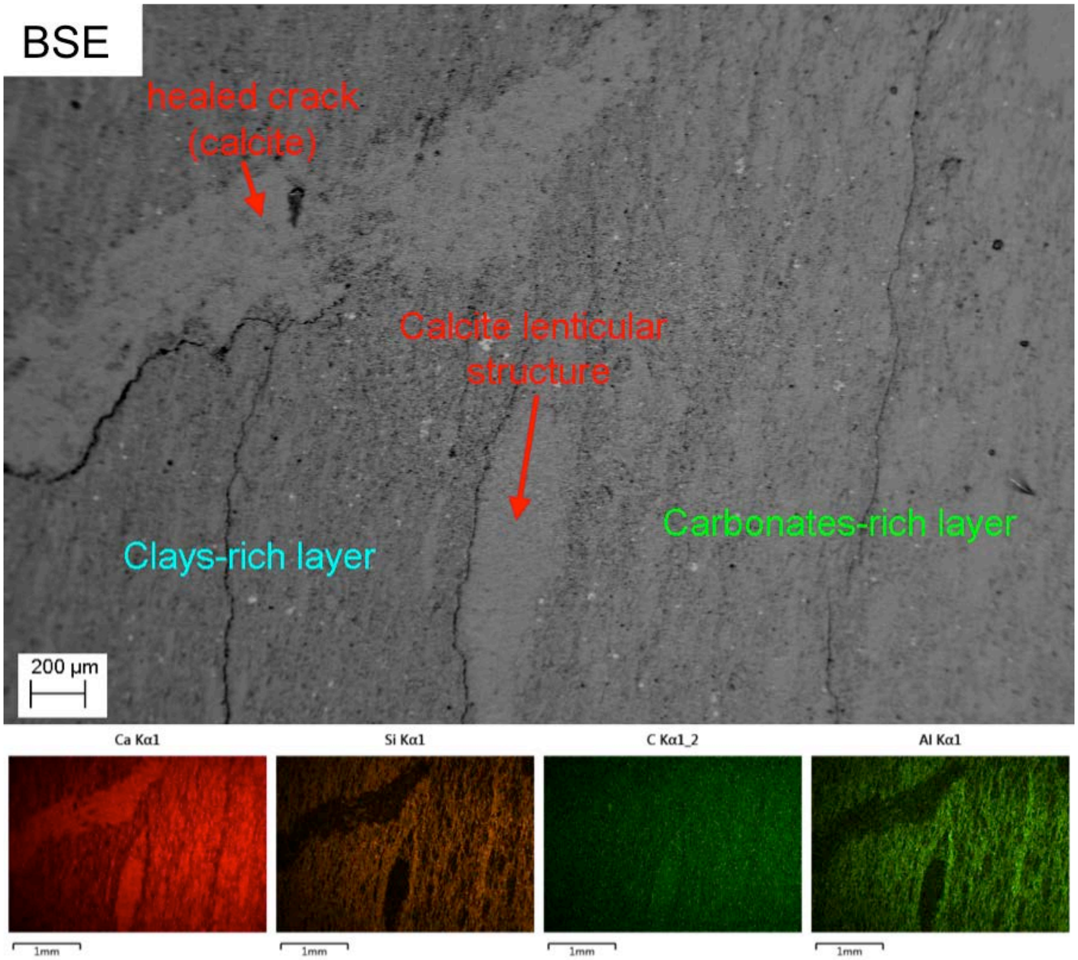

Figure III.1.3: BSE (top) and EDS (bottom) maps of layered structure present in the sample. The EDS maps highlight the texture present on this sample, mostly due to the distribution of calcite (see Ca elemental map, bottom left).

Organic-rich particles are also present as can be seen in Figure III.1.4 (BSE images and EDS maps, with a zoom of the particle). From the SEM analysis different accessory phases have also been identified including dolomite, pyrite (including typical framboids), and sphalerite/greenockite.

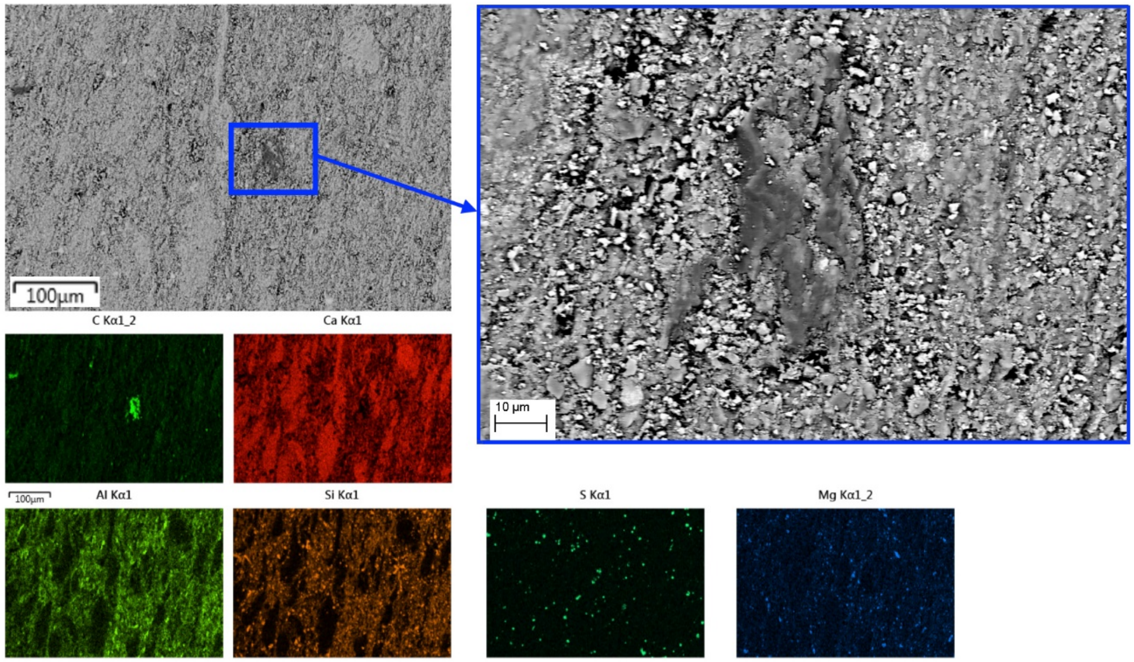

Figure III.1.4: Example of an organic particle embedded in carbonate-rich layers (top BSE, bottom EDS).

X-Ray Powder Diffraction analysis

To complete our initial characterization of the Niobrara shale sample, a fragment contiguous to the sample analyzed has been chosen and ground to a powder for XRPD analysis. The XRPD profile has been analyzed via Rietveld analysis to obtain quantitative information about the mineralogy of the sample. Results are as seen in Table III.1.1 (weight%, sigma referred to the last digit).

Table III.1.1:

Quartz:	14.6(2)
Smectite (~14Å):	6.6(4)
Plagioclase:	3.5(3)
Calcite:	48.5(3)
Dolomite:	6.8(2)
Pyrite:	2.1(1)
Detrital mica-illite:	17.5(4)
(modeled with a muscovite 2M1 structure)	

Lattice preferred orientation was considered for phyllosilicates and carbonates. Turbostratic disorder for the smectite has been included in this analysis. As it is possible to see, the carbonates (mostly calcite) comprise slightly more than one half of the sample by weight. The crystallinity of the sampled calcite is not very high (meaning not as high as in sparry calcite), as it is possible to appreciate from the peak shape function and to indirectly infer from the sample preparation (top loading sample holder for XRPD) that did not induce appreciable crystallographic preferred orientation. This confirms the observation from the SEM where the calcite looks more micritic in nature.

From this first characterization it is possible to see that this shale is very rich in carbonates (mostly calcite, with some dolomite), distributed in layers and in micrometric lenticular structures. The presence of the micritic calcite is also related to the microporosity of the sample. The clay amount is typical of many shales, with smectite (with significant structural/stacking disorder) and detrital mica, while other phyllosilicates such as chlorite and kaolinite seem to be absent. The organic-rich particles are scattered throughout the sample, and do not seem to follow the bedding by forming thin and flat structures like in many gas shales. Also, no significant porosity is visible at the magnification used for imaging.

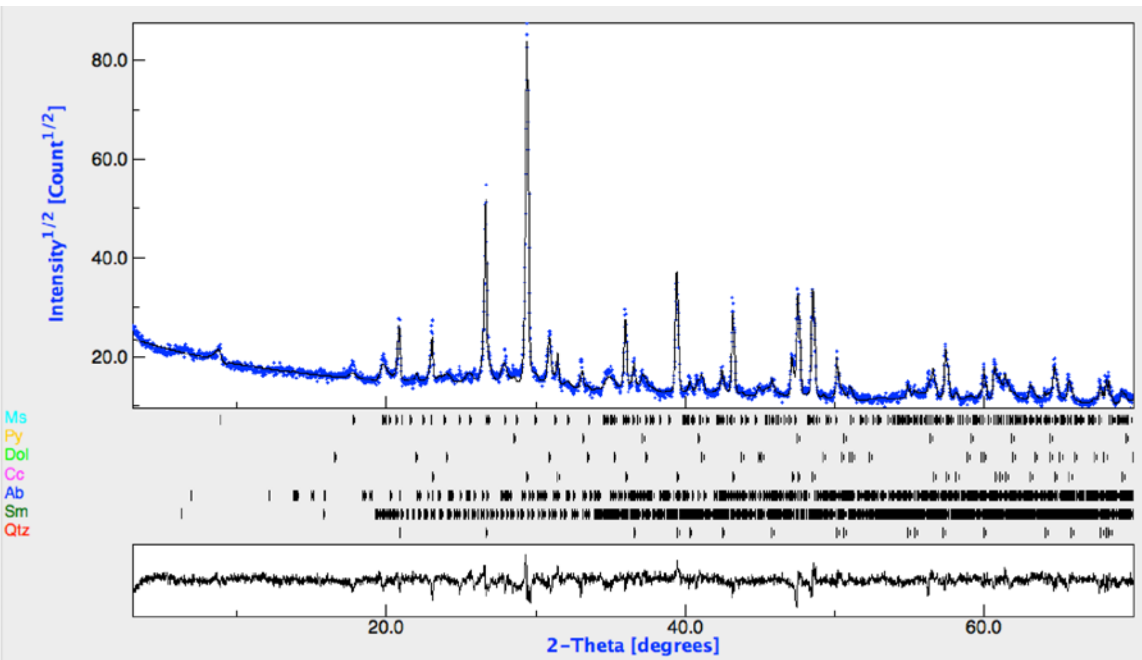

Figure III.1.5: Measured and fit XRD profiles of Niobrara sample. Measurements are blue dots (top panel) while the Rietveld refined fit is the black curve. As can be seen, measurements and fit are in good agreement.

Static X-ray Micro-CT Analysis

To more thoroughly investigate the microstructure of the Niobrara shale, synchrotron X-ray (SXR) microCT has been carried out on selected samples. This technique allows to obtain 3D data and can study the sample in an undisturbed state (no need for vacuum or polished surfaces). The first observations obtained via SXR microCT confirm what seen using other imaging techniques: carbonates form lenticular structures surrounded by clay-rich layers a few µm thick. At a larger scale (~1 mm) also layering structures can be seen, highlighted by a different carbonates/clays ratio. Since the clay-rich layers are less attenuating, they are easily seen in SXR microCT datasets as darker layers (see figures below).

The use of synchrotron radiation in this kind of analysis is advantageous since it is possible to take advantage of the monochromaticity and spatial coherence of the beam, and to choose proper compromises of resolution vs. field of view, to obtain very high-quality datasets. The facility used for these measurements is beamline 8.3.2. at the Advanced Light Source, at the LBNL.

A preliminary investigation to obtain information about the fracturing properties of this shale has been carried out as well. Simple unconfined uniaxial breakage of samples has been performed to see if the crack network generated can be related to textural features. In particular we wanted to see if the breakage of the sample would occur preferably in the clay-rich layers, a characteristic often encountered in shales (es. Mancos Shale). This preferential breakage can have an impact in the micro-fracturing behavior and also in the recovery of hydrocarbons, e.g. in case it would occur preferentially in hydrocarbon-rich layers. The geometry of the fracture surfaces is also important from a context of potential reactive surface area for a number of different processes. In this Niobrara sample we haven't found any clear evidence that the breakage of the sample is *strictly* related to the clay-rich layers, even if evidence of some preferential splitting behavior has been observed.

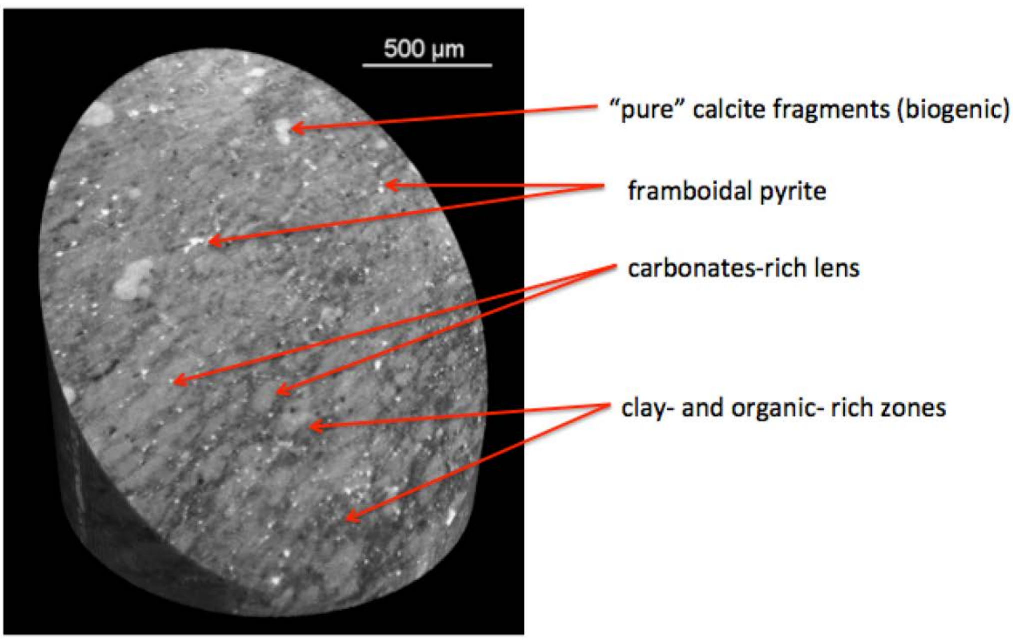

Figure III.1.6: Virtual cut of a Niobrara sample measured with SXR microCT. The different mineral components and textural features as seen with SEM-EDS are visible also with this technique, giving a 3D context to the microstructure of the sample.

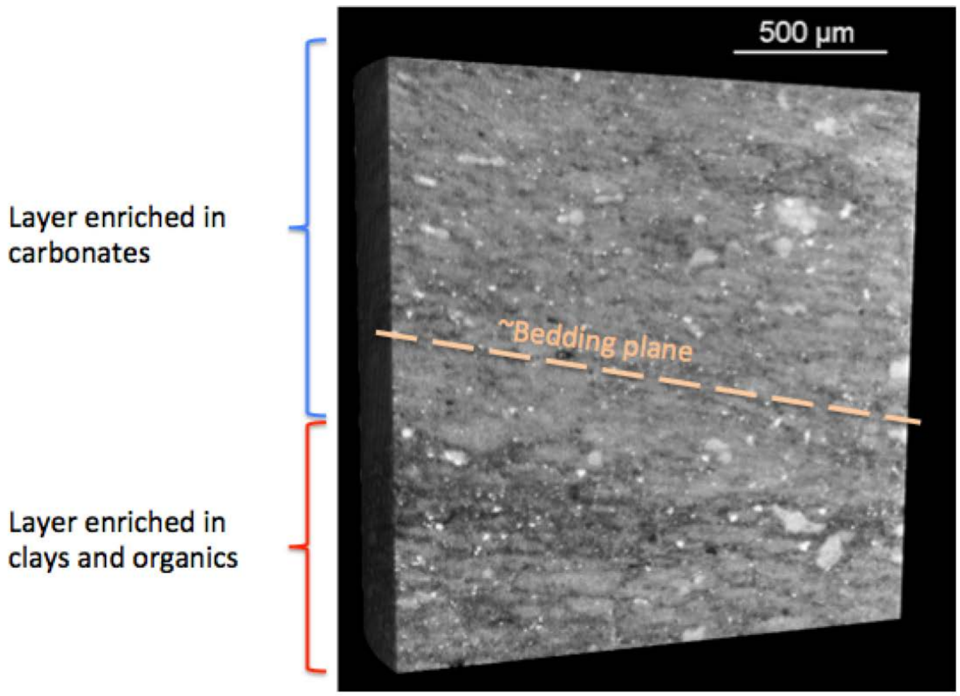

Figure III.1.7: Virtual thin section of the sample, where a better image of the bedding features is shown. It is possible to appreciate the compositional differences highlighted by the different attenuation of x-rays at different scales.

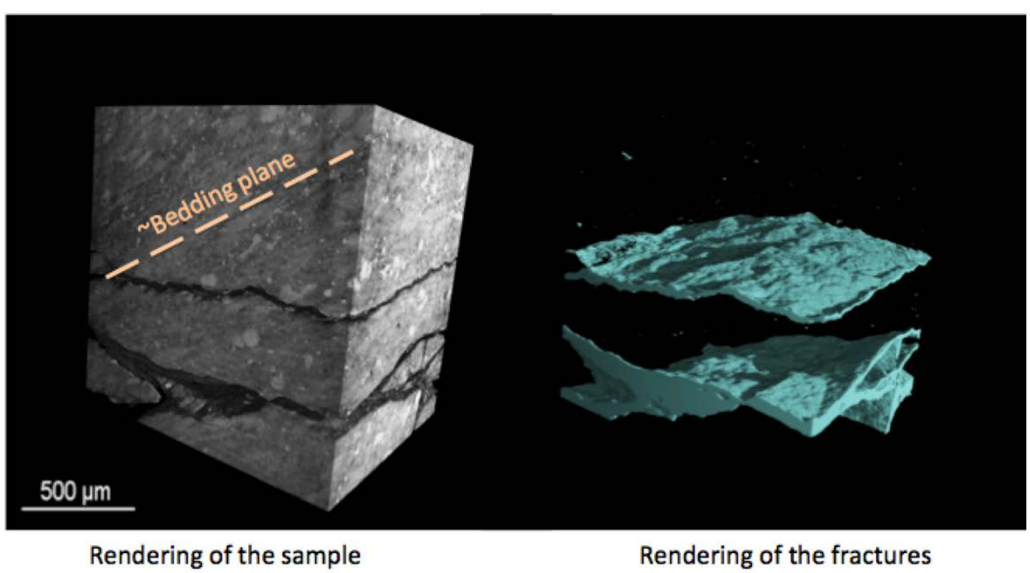

Figure III.1.8: In this first experiment the fractures look very irregular and splintery. They do not seem to be strictly related to the sample microstructure.

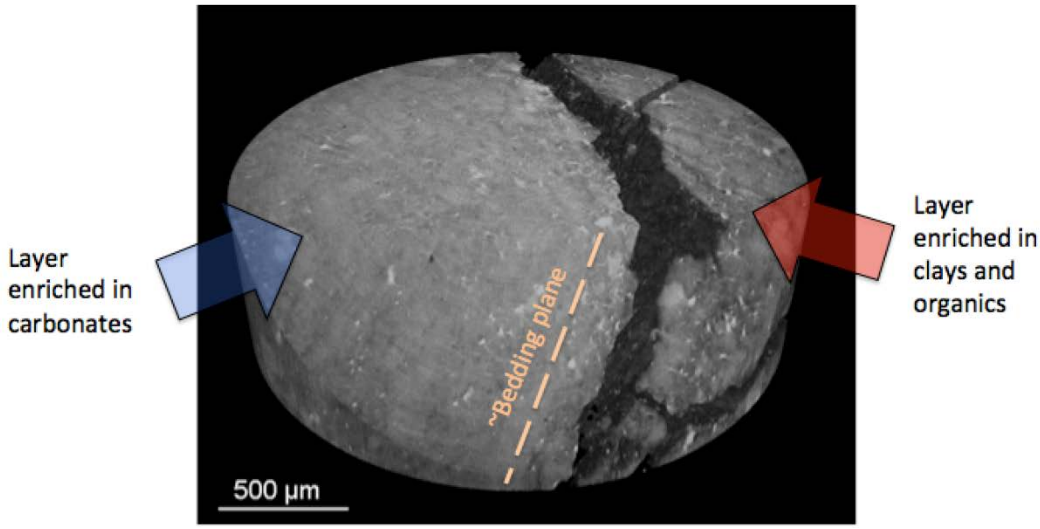

Cylindrical sample, oblique virtual cut facing the viewer

Figure III.1.9: In this experiment the fractures look irregular as well, the main crack is has been generated at the interface of a clay-rich layer with a carbonates-rich layer, following the bedding plane. The clay-rich layer also shows a number of secondary fractures, while the carbonates-rich one is perfectly intact.

The material characterization via diffraction and electron imaging techniques, plus the starting, static, scans of the Niobrara shale samples, also provided an excellent starting point to plan much more challenging experiments of dynamic SXR microCT aimed at understanding the behavior of oil shale at conditions compatible with hydrocarbon recovery processes in the reservoir.

It is worth to remark that the combined effort of beamline 8.3.2. at ALS and the Earth Sciences Division of LBNL for imaging in real time geochemical processes at reservoir conditions is an ongoing effort. But at the same time the local x-ray imaging facility is among the very first worldwide for dynamic imaging (4D XR microCT), with a significant experience on geological materials, as it's becoming evident from the presentations at conferences and from the publications record.

Subtask III.1.2: In situ Synchrotron X-Ray microCT experiments

Objectives:

The in situ SXR microCT experiments carried out were aimed at answering three questions:

1) How a fracture under a flow of carbonated water evolves. From a hydrocarbon recovery point of view, this is a critical point, since if CO_2 is used in the reservoir exploitation, and the reservoir rock is reactive at those conditions, significant modification of the microstructure and of the fracture geometry can occur. It is evident that if in the considered scenario the fractured behave as self-sealing systems, the hydrocarbon recovery would be problematic. On the other hand, self-enhancing systems would increase the local permeability of the reservoir, thus potentially helping with the recovery of the product.

2) The second question is related to EOR involves the utilization of liquid/supercritical CO_2 as a solvent to sweep hydrocarbons from fractured oil shales. The efficiency and the repercussion on the fracture aperture and crack surface microstructure of this process at the pore scale are still poorly understood and our experiment tried to shed some light on this unknown.
3) The third question addresses the behavior of a propped fracture under the flow of aqueous CO_2: will the weathering observed without the proppant cause embedment of the proppant grains?

Experiment 1: Monitoring the development of the fracture under a flow of carbonated water.

In this first experiment we have prepared a 3/8" x 1" Niobrara shale core, cut in half vertically to simulate a fracture along the sample. Bedding plane was chosen to be sub-horizontal to highlight eventual features due to different layers composition.

The experiment was carried out using the in-house developed triaxial cell able to perform in-situ measurement at the SXR-microCT beamline. The experimental conditions chosen for this experiment were: pore pressure = ~1400 psi. Confining pressure = 1700 psi. Fluid: equilibrated CO_2-saturated water at 500 psi, ~25°C. Flow was 5 μl/min for the first part of the experiment, 10 μl/min for the second part (to increase the reaction extent).

Experimental Results

The Niobrara shale showed some unexpected behavior. While the dissolution of the carbonates was relatively fast, as expected, the development of the surface of the fracture was different from any other rock investigated so far at similar conditions. Specifically, we assist at the development of an unexpectedly wide weathered zone along the directions of preferential flow in the fracture, due to the preferential dissolution of the carbonate-rich lenses. The resulting less soluble material on the fracture surface, mostly clays and quartz/feldspar, is *not* easily mobilized by the flow of the reactant, but resides on the fracture surface for at least a few hundred microns of thickness.

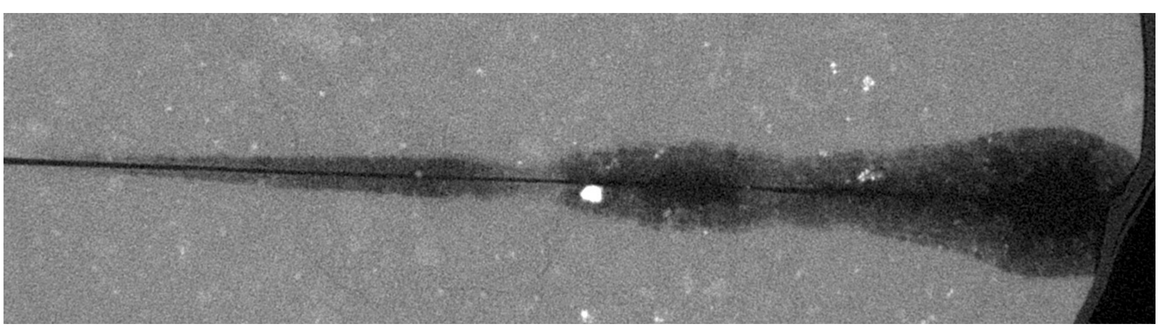

Figure III.1.10: Horizontal cut of the sample after the reaction: the weathered layer developed on the crack surface and the preferential flow channels are evident. (image width: ~7mm)

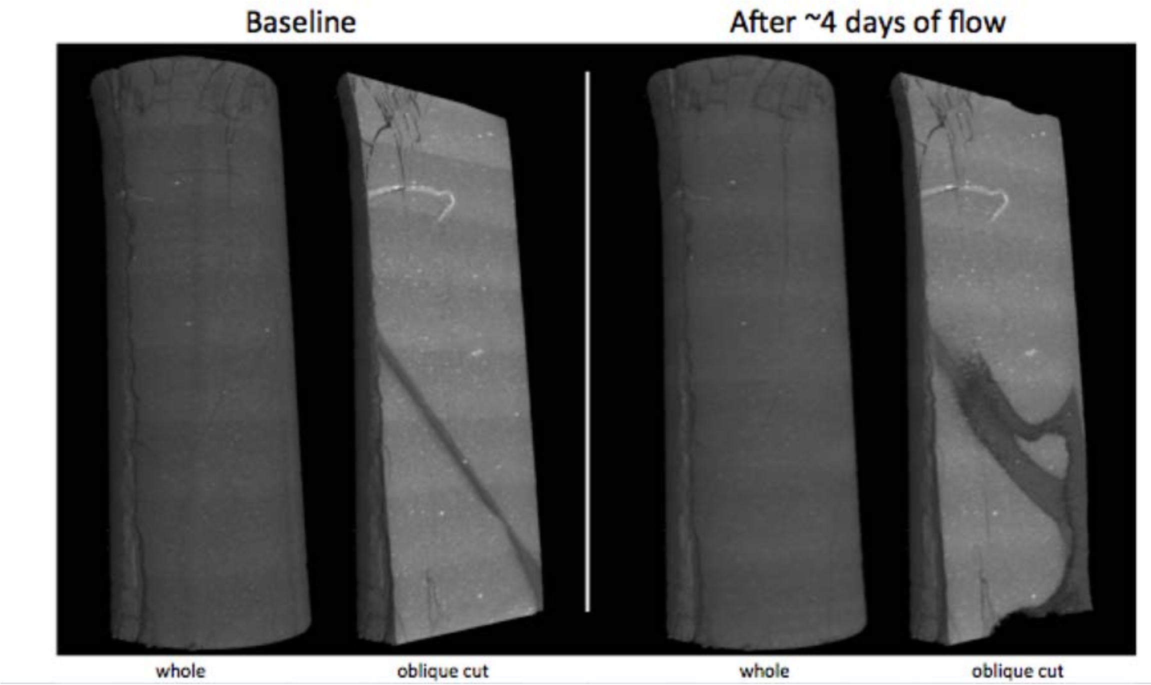

Figure III.1.11: The whole sample, before and after the reaction.

The aperture maps also show the development of the fracture geometry, with branching and the development of a "wormhole" structure with the evolution of the reaction:

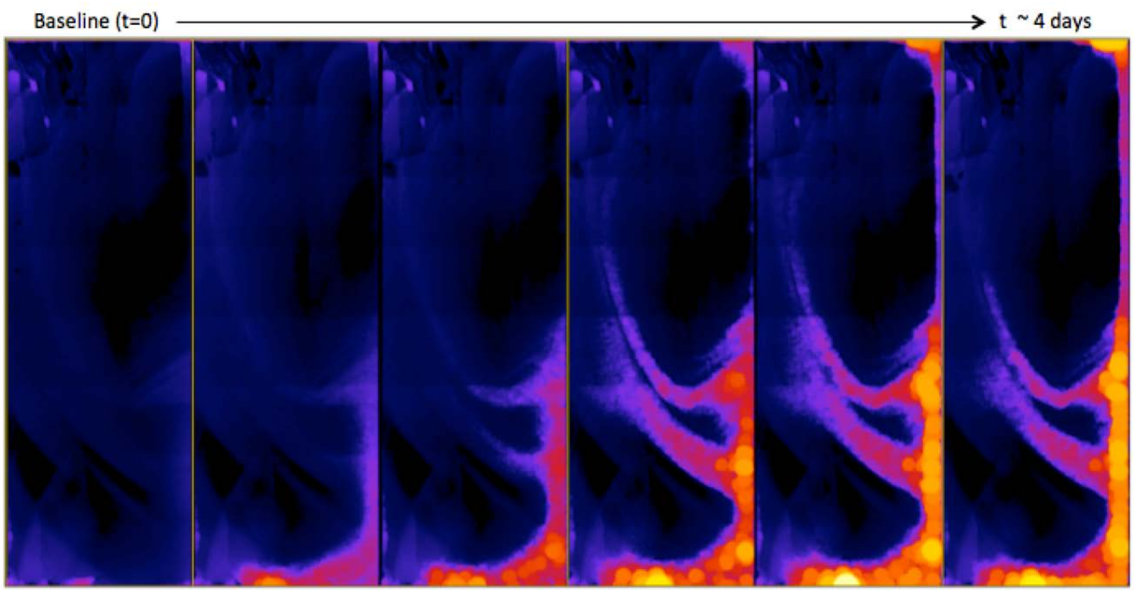

Figure III.1.12: Local thickness aperture maps of the fracture at different stages of the reaction. Each step covers the whole sample with an area approximately of 3/8"x1". Inlet is at the bottom of the sample.

From the slice above it is possible to see that the microstructure of the crack surface is not smooth, but apparently it follows the texture of the rock. This is to be expected since the lens-shaped structures are expected to dissolve faster than any other component. A SEM study also confirms this observation:

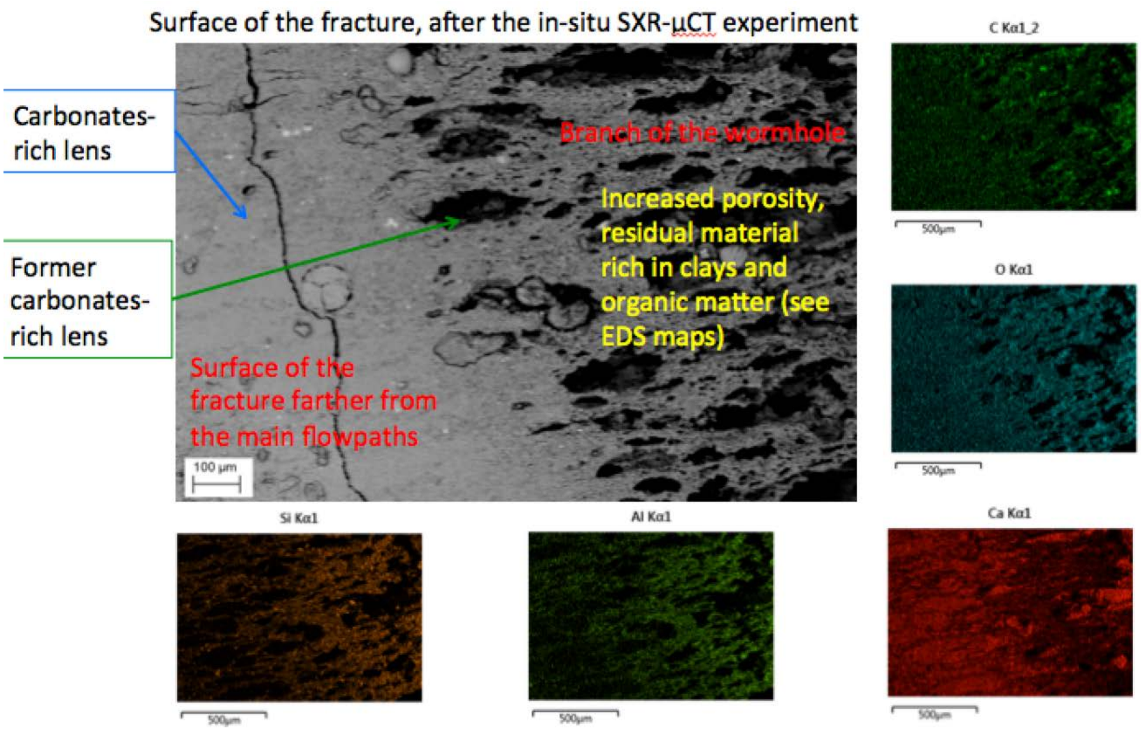

Figure III.1.13: SEM analysis on one of the “branches” of the wormhole.

From the SEM maps it possible to appreciate how the newly developed porosity is indeed due to the dissolution of the carbonate-rich lenses. A more interesting observation is that the residual clay-rich material is also enriched in organics (see C EDS map).

To summarize the information pertinent to EOR obtained with this experiment, it is possible to affirm that, in this context (mini-core, limited reaction time):

1) There is an *increase in permeability* due to the wormholing and preferential dissolution of carbonate-rich structures.
2) Despite the development of a wide weathered zone along the preferential flow paths, the dissolution does not generate a significant change in the contact points in the fracture (so *the fracture is not closing* under the applied confining pressure)
3) The weathered zone is *enriched in phases associated with the organic content* of the rock, potentially making them more exposed in case techniques involving oil solvents were employed.
4) The weathered zone, made for a significant part from clay flocs, is also likely to have *bad mechanical properties* (important in case proppants are considered: es. sand grains would embed very easily in this layer, losing their ability to keep the fracture open).

5) The *migration of fines is difficult*, thus leading to the development of the extensive weathered zone on the crack surface.

Experiment 2: Effect of sweeping a propped fracture with liquid CO_2.

In this second experiment we wanted to study the behavior of a water-saturated sample of Niobrara shale, with a fracture filled with proppant. Main goal was to monitor the solvent action of liquid CO_2 and eventual modifications to the fracture geometry, in particular proppant grain embedding in case of softening of the surface of the fracture.

The experiment was again set using our triaxial cell. The sample was a Niobrara core ~ 3/8" (diameter) x 1/2" (height) in size, cut in half and filled with a double layer of sand grains (20/30 mesh). The cell used in this experiment is shown below:

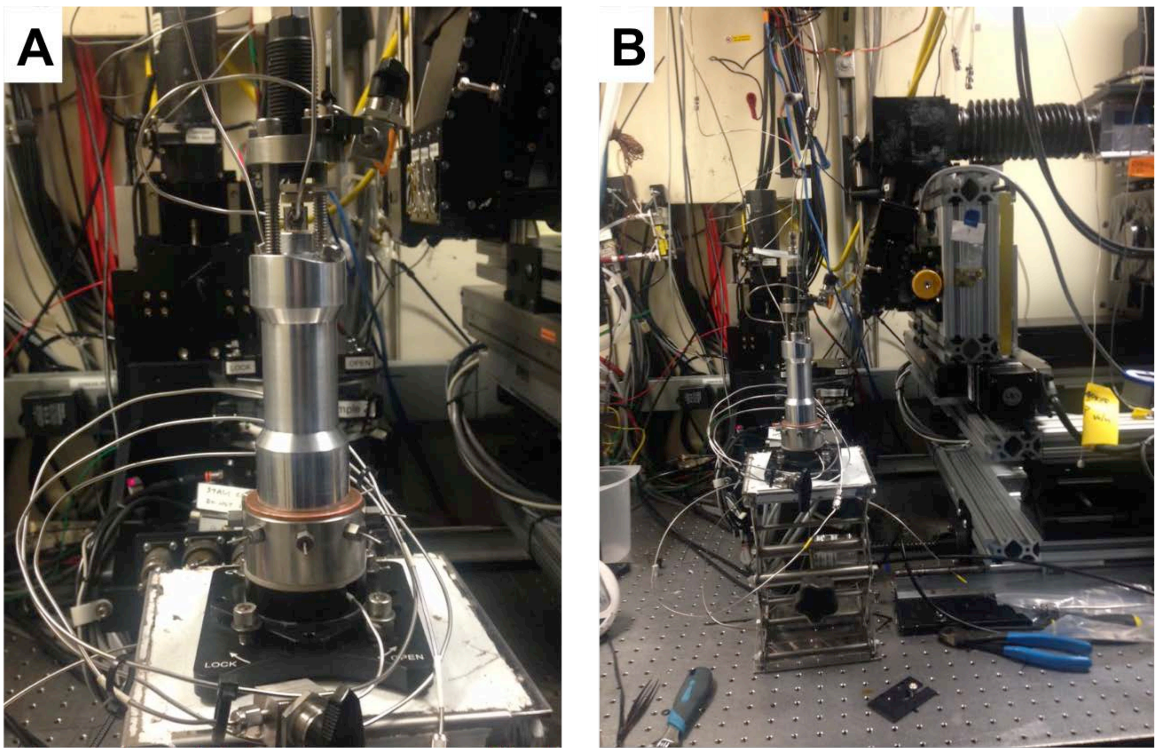

Figure III.1.14: New HP triaxial cell for reservoir sample imaging at Beamline 8.3.2. Panel A shows a close-up of the refurbished micro triaxial vessel during the experiment while panel B includes the beamline hardware including the optics frame (on the right).

The sample was pressurized to a pore pressure of 1100 psi while confined at 1300 psi of hydrostatic stress. After this initial pressurization, a baseline microCT scan was acquired of the entire sample with an isotropic 6.87 µm voxel size.

Pure CO_2 was then compressed from gas to liquid phase (1100 psi, 24.6 °C) in an ISCO syringe pump and injected into the fractured sample at an initial rate of 100 µl/min for 3.25 hours followed by a first repeat scan. At this point flow was restarted at 25 µl/min for 11 hours followed by a second repeat scan. To the end of injection, approximately 36 mL of CO2 were injected through the fracture. After completion of the injection phase, another scan was taken increasing the confining pressure to 1700 psi, trying to induce fracture closure.

The experiment showed extremely little changes of the system. The first injection of liquid CO_2 generated a partial displacement of the water in the sample, but a significant amount of water was left in the fracture, thus limiting the contact of the solvent ($CO_{2(liq)}$) with the solvation target (the oil close to the fracture surface). Moreover, a behavior such as the one described in the first experiment is also limited, since a close to equilibrium state in the water with Ca^{++} and CO_3^{--} /HCO_3^- ionic species is quickly reached, resulting in just a limited amount of dissolution on the crack surface. This makes the whole system quite static, with exception of the two-phase flow: the solvation effect is limited by the pre-existing water, and at the same time the chemical reactions are significantly slowed down because of the fast saturation of the trapped water.

Shown below there's a series of rendering of the sample *after* the reaction. In a reactive system it would be expected to see some modifications on the crack surface (to better appreciate this part of the sample a series of virtual cuts are presented), more specifically a decrease in the x-ray attenuation values (~decrease in density) at the surface of the crack, but this effect is virtually undetectable.

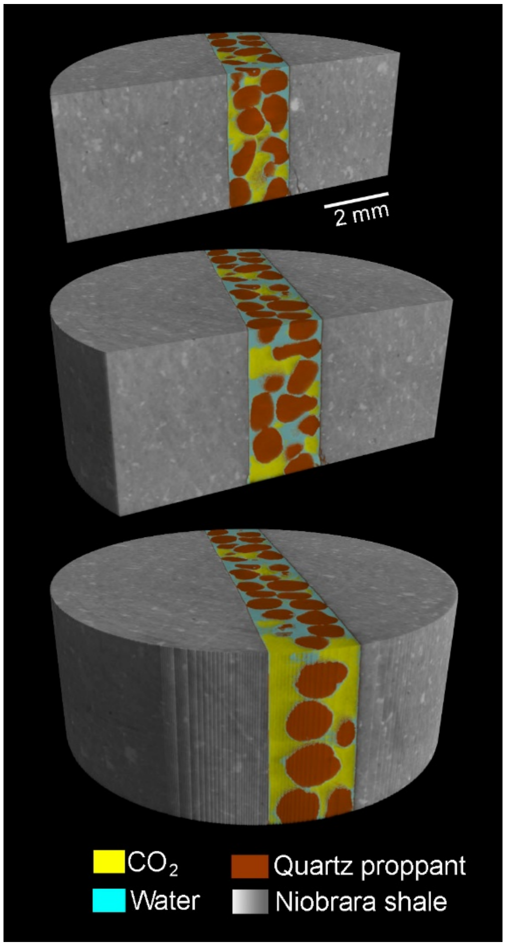

Figure III.1.15: Cuts through the fractured Niobrara sample during liquid CO_2 injection. Niobrara shale matrix is shown in grey while the quartz sand proppant is shown in brown. The CO_2 and water phases are shown in yellow and blue respectively.

In the renderings different components have been segmented and labeled with different colors for clarity. The “shale” component has been left in gray scale to better highlight its texture and the (non-)presence of eventual weathered zones on the crack surface.

To better check for fine changes in the sample a further step in the analysis was taken. An equivalent vertical section of part of the sample was taken from the datasets before and after the reaction. A registration procedure has been employed to take into account the slight shifts of the sample due to mounting/unmounting, compression, etc. A difference of the registered images has been calculated to highlight where changes in grayscale (~density) are present. In the figure below the vertical slices pre- and post- reaction are presented using a different lookup table to better highlight the differences (A and B). A part from the zone with the fluids, the two images look in fact absolutely identical. In C the pre-reaction vertical section (in grays) with superimposed a colormap where a decrease in attenuation values occurred is plotted. This color map highlights where the reactions in the sample happened. It is evident that the extent of the reactions is extremely low and concentrated in some parts of the crack surface, apparently far from the proppant grains, where the flow and diffusion are likely to be faster, and in these zones the extent of the reaction barely reaches 20 μm in thickness.

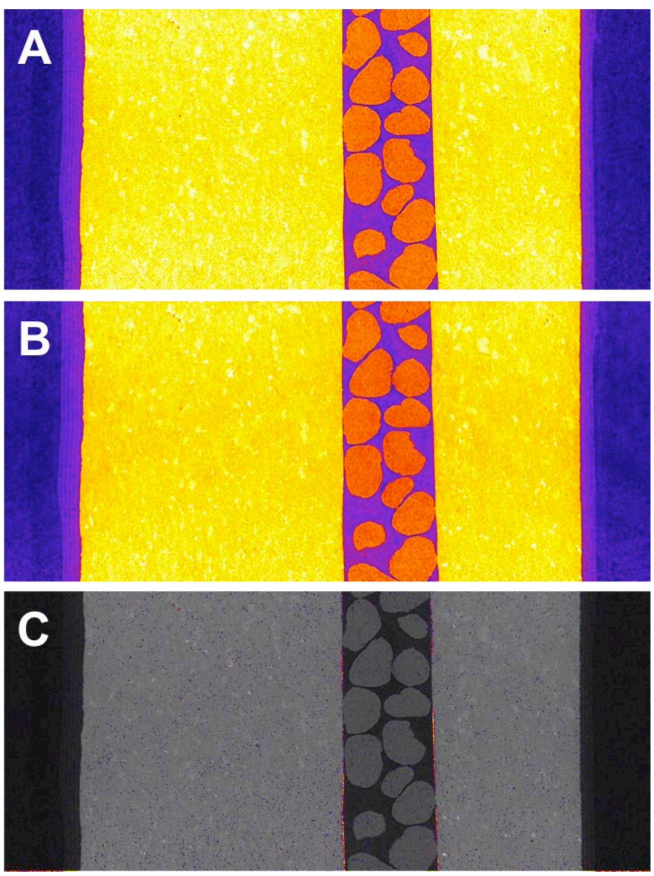

Figure III.1.16: Cross-sections of tomographic volume showing near-fracture region before (A) and after (B) liquid CO_2 injection. Panel (C) shows the baseline image with color highlights in the narrow near-fracture regions which showed modification (only 2-3 voxels).

To summarize the results important from an oil recovery perspective obtained with this second experiment (we remark that the processes investigated with this experiment are limited to ~ one day):

1) The water in the sample cannot be effectively displaced. Therefore, *the effect of the solvent, the $CO_{2(liq)}$, is strongly limited* by the presence of the trapped water. This significantly limits the contact of the solvent with the oil close to the surface of the fracture.
2) The trapped water and the two-phase flow also limit the transport of ionic species, thus creating a close to equilibrium situation in the water trapped at the contact with the crack surface, thus *inhibiting the dissolution of the carbonates on the crack surface*.
3) Given the very limited modifications of the crack surface and the mechanical properties of the shale, in this experiment no variation of the fracture aperture is detectable when increasing confining pressure to 1700 psi (600 psi of differential pressure). The proppant is effectively keeping the fracture open.

Experiment 3: Flowing carbonated water in a propped fracture.

While the new microstructure at the surface, as observed in the experiment #1 (flowing carbonated water in a fracture without proppant) could be advantageous for hydrocarbon migration, increasing the surface area at the fracture surface, the mechanical properties of the surface could be severely affected. The generation of channeling features also implies a self-enhancing behavior, in the observed timescale, which could be advantageous in a hydrocarbons recovery scenario.

On the other hand, in a propped fracture, the critical areas are the contacts of the proppant with the surface. The mechanical properties of these small areas are the controlling factor keeping the fractures open. If the mechanical properties of those areas are degraded, for example by a weathering process dissolving the mechanically strong calcite matrix, proppant embedment and subsequent decrease of the fracture aperture is expected to occur. To validate this hypothesis, we run an experiment at the same conditions as the experiment #1, but with two main differences: 1) the fracture was filled with quartz grains used as proppant. 2) The flowrate of the carbonated water was much faster to avoid channeling/wormholing, since we targeted a uniform dissolution of the fracture surfaces, to better observe eventual proppant embedment. The total amount of fluid flown in the sample was the same.

The dissolution at the fracture surface proceeded as expected, in a similar fashion as observed in the first experiment. The calcite cementing the sample is dissolved, leaving a residue enriched in less soluble minerals. But no variation of the fracture aperture, within the resolution, was observed, even when increasing the confining pressure up to 1850 psi. So, the fracture was not subject to fracture closure due to proppant embedment even if the expected pervasive weathering was present. The reason of this general behavior is linked to the specific behavior of the small contact areas of the proppant with the fracture surface: the proppant is actively protecting the contact areas, avoiding the reactant to reach them. As we'll see better in the next section of the report, when looking at the simulated flow in a propped fracture, the flow is effectively channeled between the proppant grains and the surface, leaving zones of slow flow where the proppant is in contact with the shale. Here the availability of reactant likely becomes more and more dependent on diffusion, rather than flow, hence a slower reaction rate. Of course, this becomes especially true when flattish parts of the proppant grains are in contact with the fracture surface. In Figure III.1.17 it is easy to observe where the proppant-shale contacts protected the surface from weathering. No weathering means that the mechanical properties are preserved, and no embedment can occur.

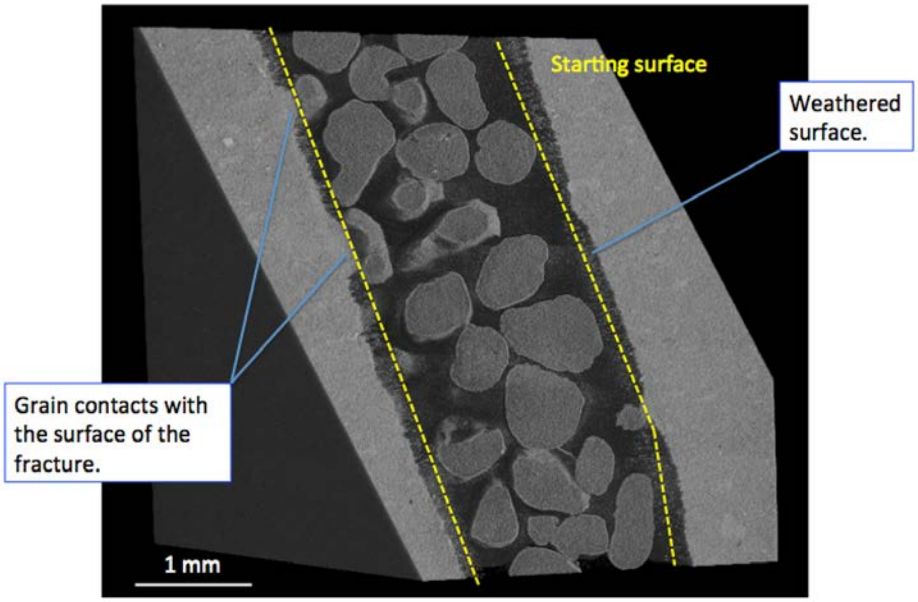

Figure III.1.17: Oblique cutout of the sample after the experiment. In yellow the starting surface is displayed as a reference: the sample was sawn; therefore the starting surface was perfectly flat.

To further emphasize this behavior of the proppant protecting the contact areas from chemical weathering, in Figure III.1.18 we present a different cutout, with one of the sides of the sample and the proppant layer partially cut out, to better display the surface of the fracture, to appreciate the new topography.

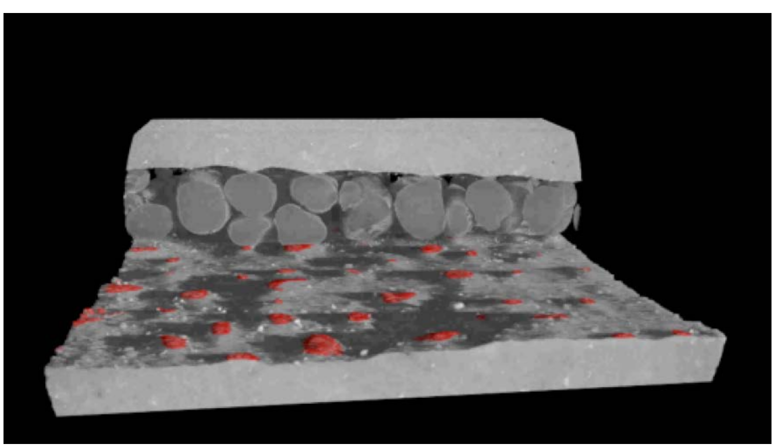

Figure III.1.18: 3D rendering of the sample at the end of the experiment, with the top side and the proppant layer partially cut. On the fracture surface, the contact areas are highlighted in red.

As previously mentioned, the starting surface was a flat, sawn, surface, but after the experiment the presence of a modulated topography with "hills and valleys" is clearly present. The top of those "hills" correspond to the contact areas of the proppant with the fracture surface, so the distribution of proppant is directly linked to the newly generated topography of the fracture surface.

Summarizing, in this kind of oil shale, where microcrystalline calcite is cementing the shale and providing most of its mechanical strength, flowing a reactant able to solubilize this cement is actually enhancing the flow properties of the fracture, without the problem of weakening the contact areas and causing proppant embedment. In a more applied context, the flowing of e.g. a short "acid spike" would actually be beneficial in a context compatible with our experiments: in addition to dissolving fines present in the fracture, a partial dissolution of the fracture itself would enhance the flow properties of the system, without the weakening of the proppant-shale contacts. The extent of flow of acid to significantly weaken these contacts and result in proppant embedment, is higher than it would be generally expected, but of course is bound to occur with the progressive development of flow structures in the system.

From our experiments, it seems that the situation to be avoided is the one where the acid resides for a long time in the system, where diffusion would eventually reach the contacts and progressively weather the material there. Fast flow for short amounts of time is likely the best scenario, with uniform dissolution at the fracture far from the contact areas, and negligible weathering of the material at the contacts keeping the fracture open.

Summary of the results of Sections III.1. and III.1.2:

1) Niobrara Shale has a significant amount of carbonates acting as a cement and leading the mechanical properties of this rock.
2) When subject to weathering due to acid flow (e.g. carbonated water) the resulting microstructure is led by the starting distribution of the different mineral phases, leaving a lens-shaped residue of clays, organics and other less soluble minerals with poor mechanical strength.
3) Liquid CO_2 flow for a limited amount of time does not significantly modify the microstructure of the fracture surface.
4) CO_2 dissolved in water instead can weather the surface of fractures very quickly, resulting in a microporous layer, mechanically weak.
5) The proppant in these fracture systems protects actively the contact areas from weathering.

Section III.1.3: The Microscale Parameters Controlling the Hydraulic Properties of Propped Fractures in Shales during closure: Answers from in-situ Synchrotron X-Ray Microtomography

Objectives:

1) Visualize dynamically the behavior of a propped fracture at the microscale under progressive loading, at confined conditions.
2) Investigate the role of the type of shale.
3) Investigate the role of bedding orientation.
4) Investigate the role of type of proppant.
5) Understand the evolution of the fracture topology under those three variables.
6) Understand the evolution of the hydraulic properties under those three variables.

The bulk of this work has been carried out via in situ confined loading experiments in a mini-triaxial cell at the 8.3.2. beamline at the Advanced Light Source at the Lawrence Berkeley National Laboratory. The in-situ cell employed is the mini triaxial cell first described in Voltolini et al. (2017). The cell, its ancillary equipment, and the available configurations are explained in detail in the article cited above. The setup used for these experiments involved the connection of the cell with two high pressure syringe pumps ISCO-Teledyne 260HP: the first one, connected to the annulus of the cell was set to keep a constant pressure of 2.1 MPa. The second pump was connected to the axial ram of the system, and the pressure was increased incrementally in steps, increasing the axial load. This configuration imposed a geometry of the sample with a horizontal fracture, to have the axial load direction perpendicular with respect to the fracture plane.

The samples were three different types of shales targeted for stimulated production of oil and gas: Eagle Ford, Niobrara, and Marcellus. The shales were cored in ~9 mm in diameter cylinders, with a height of ~4 mm. Both ends of the samples were cut flat. A flat cut also acted as the fracture: this choice was made to rule out the known effects of uneven fracture surface geometry, thus eliminating a variable very difficult to control (i.e. the necessity of having surfaces with the same uneven topography) to focus on the interactions of proppant with the fracture surface. A series of the three samples was cut with the bedding direction vertical, and samples of Niobrara shale were also cut with the bedding direction horizontal. All coring and cutting were done using thin-walled diamond bits and saws in water.

The nature of the samples is very similar: they are relatively strong, mechanically, and this is due to the presence of large amounts of calcite cementing the rock. X-ray powder diffraction analysis via Rietveld method on cuttings of these samples confirmed a very high percentage of carbonates, and the summary of the mineralogical composition of the samples is presented in Table III.1.2. Both Niobrara and Marcellus exceed 80% of carbonates (mostly calcite) by weight. The Eagle Ford sample displays a larger amount of lithics (mainly quartz, for all the three samples), and all the three “shales” do not exceed the 10% by weight in clays (where detrital illite is the most abundant, and a measurable amount of kaolinite is found in Eagle Ford). Compositionally the three samples are rather similar, with Niobrara and Marcellus being almost identical. The samples display very faint banding structures. The Eagle Ford sample displayed the more evident lamination structures (likely due to the higher amount of lithics and clays). The homogeneous structure of the Niobrara shale is revealed to be only apparent when looking at the sample at the microscale, e.g. with electron microscopy. Oriented lenticular structures enriched in calcite, and surrounded by material richer in clays and organic material, are present, so even if not evident macroscopically, also the Niobrara sample displays a significant degree of anisotropy.

The proppants used are Ottawa sand for quartz proppant, and ceramic ball blasting beads for ceramic proppant (Raytech Industries, Middletown, CT), to test both a high sphericity and mechanical strength media. Proppant was sieved in order to obtain a 720 μm to 1000 μm size fraction.

The samples for the measurements were mounted placing onto the lower piston of the cell the first half of the sample, then a ~1 mm high ridge was built around the top of the cylinder, using thin adhesive Kapton® tape, to keep the proppant grain and the water placed on the surface from falling from the sides. With all the samples, a loosely packed monolayer of proppant grains was placed. The top half of the shale core was then put in place. Samples were stacked vertically in two experiments. The final connection to the pistons, and insulation of the sample from the confining fluid, was done via PVDF heat-shrink tubing, clamped at the ends with gapless pinch clamps, acting as a jacket to transfer the confining pressure from the fluid in the annulus. Once the cell was mounted, the two pumps could control independently lateral confining pressure (fixed confining pressure) and the pressure on the axial direction (incremented in steps to induce the closure of the propped fractures).

The SXRμCT measurements were carried out using the same parameters for all the experiments. The radiation used for the measurements was filter-hardened (with 6 mm Al and 0.5 mm Cu filters) white light. The choice of white light allows a much more brilliant beam in the harder region of the spectrum available at 8.3.2., compared to the monochromatic option, making the measurements significantly faster. The detector system consisted in a 0.5 mm LuAG scintillator, followed by a 2× objective. The signal is then recorded by a PCO.Edge camera, using a 290 ms exposure time. In the recorded radiographs, the resulting pixel size is 3.22 μm, the image recorded by the sensor is 2560 px × 2560 px, for a resulting field of view of 8.24 mm. The tomographic scan was set to collect 1751 projection over a 180 degrees rotation; each scan required ~10 minutes to complete. Finally, the reconstruction of the volumes from the projections was carried out with a conventional filtered back-projection procedure, as implemented in the software Octopus®.

The volumes obtained were the starting point for visualization, quantitative morphological characterization, and modeling. For the visualization, volume renderings were done using the VGStudio 2.0 software. Data treatment and morphological characterization were carried out using the Fiji software. To carry out the morphological characterization and the modeling, ~4 mm cubes from the center of the samples were cropped, in order to be able to make direct comparisons with the results, and also to minimize eventual issues related to different behaviors of the sample closer to the borders. A script was written for Fiji to automatize the morphological analysis procedure (given the large amount of volumes to process), and it followed several steps. After loading the full dataset and cropping the cube of the requested size, the script applied the Otsu threshold method, calibrated on the transversal plane (with the proppant and no shale), to separate the free space in the fracture from the shale and proppant material. From the binarized image the amount of connected free space (i.e. the voids able to accommodate flow) is calculated. The following step included the measurement of the average aperture of the fracture, from an averaged profile calculated on the stack averaged on the coronal plane. The last morphometric calculation was the local thickness analysis of the voids. These three parameters were chosen because of their potential relationship with the hydraulic properties of the fracture. Stokes permeability simulations are computationally expensive, so finding a proxy able to suggest permeability variations, would simplify the estimates of the hydraulic properties of propped fractures significantly. To model the permeability of the system, we applied a 3D Stokes code solver, as described in Zuo et al., (2017), to samples rescaled to 250 px × 250 px × 250 px datasets, flowing in a direction parallel to the fractures, along the XR beam path. Results included the permeability of the fracture at all the compression stages, and the Stokes fluid velocity fields, which are extremely helpful in visualizing the distribution of the flow in the fracture, to better understand which are the features influencing the permeability the most.

Table III.1.2: Summary of the mineralogical composition derived from the Rietveld analysis of the three shale samples (weight %)

	Eagle Ford	Niobrara	Marcellus
Lithics	22.7	8.0	8.2
Carbonates	68.6	86.5	83.2
Clays	8.7	5.6	8.6

Types of shale

The first experiment targeted the three different types of shale, with the bedding direction vertical in the mini-cores. The samples were subject to uniaxial compression in a sequence of 8 different steps, up to 9.31 MPa (1350 psi) of differential pressure. The volume rendering images of the three samples (Eagle Ford, Marcellus, and Niobrara) at the end of the experiment are shown in Figure III.1.19. On the left column, a transverse section cutting the proppant grains bed is shown, to highlight the mechanical response of the grains. On the right column, the whole field of view is shown, to better highlight the mechanical response of the shale. At the end of the experiment, both proppant and shales display pervasive fracturing. Some quartz grains completely shatter (generating a large amount of fines), other quartz grains just fracture on a few planes, other remain intact. In the regions where the quartz tends to be more intact, induced fracturing of the shale is present, and partial embedment of the proppant, in a rather brittle fashion, occurs. Among the three different samples, the one displaying the most interesting behavior is the Eagle Ford. As previously noted, this sample has a more marked bedding compared to the other two, and in Figure III.1.19 the bedding direction is roughly vertical. In the rendering with the section highlighting the proppant it is possible to observe in the center-right position a part of the sample where the proppant is embedded, instead of shattering, as in the left side of the sample. A careful observation of the shale reveals that the XR attenuation signal is lower in that region of the sample. The preferential embedding along that line is then due to the presence of a thin layer enriched in clays and lithics. This observation confirms the hypothesis that suggests the samples with more carbonates cementing the sample are mechanically stronger. In this specific case this behavior is emphasized because the mechanical strength of the proppant seems to be in between the strengths of the calcite-rich layer and the clay-rich layer, therefore in the former the proppant shatters, in the latter the proppant induces pervasive breakage and embeds. Concerning the fracturing of the shales, very little anisotropy of the fractures network induced by the layered structures seems to be present.

In addition to qualitative observations, we have calculated morphometric parameters potentially related to the hydraulic properties of the system. The results are summarized in Figure III.1.20, where in Figure III.1.20a the connected “porosity” (i.e. the percentage of space available for flow in the sample) is plotted vs. the different loading stages. In Figure III.1.20b the evolution of the average aperture is plotted for the three shales, and in Figure III.1.20c the local thickness (LT) analysis summary curves are displayed. From the LT analysis, the LT values for each voxel in the pore space is obtained, so the original data are LT distribution curves, for each sample at each loading stage. In order to summarize these results, we have calculated the average value and the standard deviation σ (displayed using error bars in the plot) of the distributions. The two values combined help to explain the topology of the void space: large average values hint to potential large flowing structures, while the σ will define how variable is the LT in a system. A very regular network made with tubular structures will have very small σ values and the average LT would represent the diameter of the tubes, while a very irregular interstitial structure would display high σ values and the LT absolute value would not be substantially helpful by itself, but its evolution would provide hints about how the changes in the pore space proceed. None of these parameters is directly related to the permeability, which has been calculated (Figure III.1.20d) and is discussed later.

The trends for the porosity evolution are rather regular: the more the fracture is loaded, the more the porosity decreases, in a rather linear fashion. Differences among shales are very subtle, since all three display a very similar trend. A rather linear decrease trend is present also in the average aperture plots, with one difference: at the end of the loading sequence, the value tends to decrease more rapidly because of the fracture collapse, i.e. when the loading induces significant shattering of the proppant grains and pervasive fracturing in the shale. This is especially evident in the Eagle Ford (last loading step) and Niobrara (second last loading step) samples. The interpretation of the LT plots is more complicated: the trends for the average LT values tend to follow the porosity variation during the early loading stage, while at the end the trends to become more similar to the aperture ones, including the variations of the trends due to the fracture collapse in Eagle Ford and Marcellus. The σ values slightly decrease with the decrease of LT, and this is due to the shrinking of the widest flow paths close to the top of the fracture, which will be discussed in more detail in the Stokes flow simulation paragraph. Absolute values of σ are fairly high, compatible with an interstitial type of pore structure.

The final target of this research is to try to link different parameters to the permeability of the systems we studied. Direct permeability measurements on such small samples at these conditions are very challenging at best, therefore we calculated the permeability via Stokes flow simulation. The results of the permeability modeling work are plotted in Figure III.1.20d. Again, the trends of these curves are relatively similar for the three samples, and display features linkable to the morphometry plots. All the samples show a fast rate of permeability decrease at the early stages of loading, after a low loading threshold is met. From the observations on the renderings, at this stage the proppant moves: sand grains both rotate and translate to accommodate the compression, often by moving their short axis along the compression direction and rearrange their position in the fracture (as evident in the movie provided in the supplementary material). After the proppant rearrangement, the permeability decreases at a slower pace: at this stage, the proppant is more locked in place, and the first breakage at the contacts of the largest grains with the shale start to occur. Finally, the last decrease in permeability is sudden, and it involves the collapse of the fracture. Here the quartz shatters, and the shale fractures pervasively, embedding the proppant grains. This last trend follows the aperture plots.

To clarify this complicated behavior and its impact on the hydraulic properties of the fracture, we show in Figure III.1.21a a cutout of the early stage of the sample with the Stokes flow velocity field in the fracture space. Quartz grains are randomly dispersed, and the flow field shows an interesting feature: the region of the fracture where the flow is the fastest is at the very top. This is due to the orientation of the fracture: in a horizontal fracture the grains would distribute laying on the lower surface, with only the largest in size able to touch the top of the fracture, simply because of gravity. This leaves a relatively empty space close to the upper surface of the fracture. This space becomes a preferential flow path, as highlighted by the hotter colors in the figure.

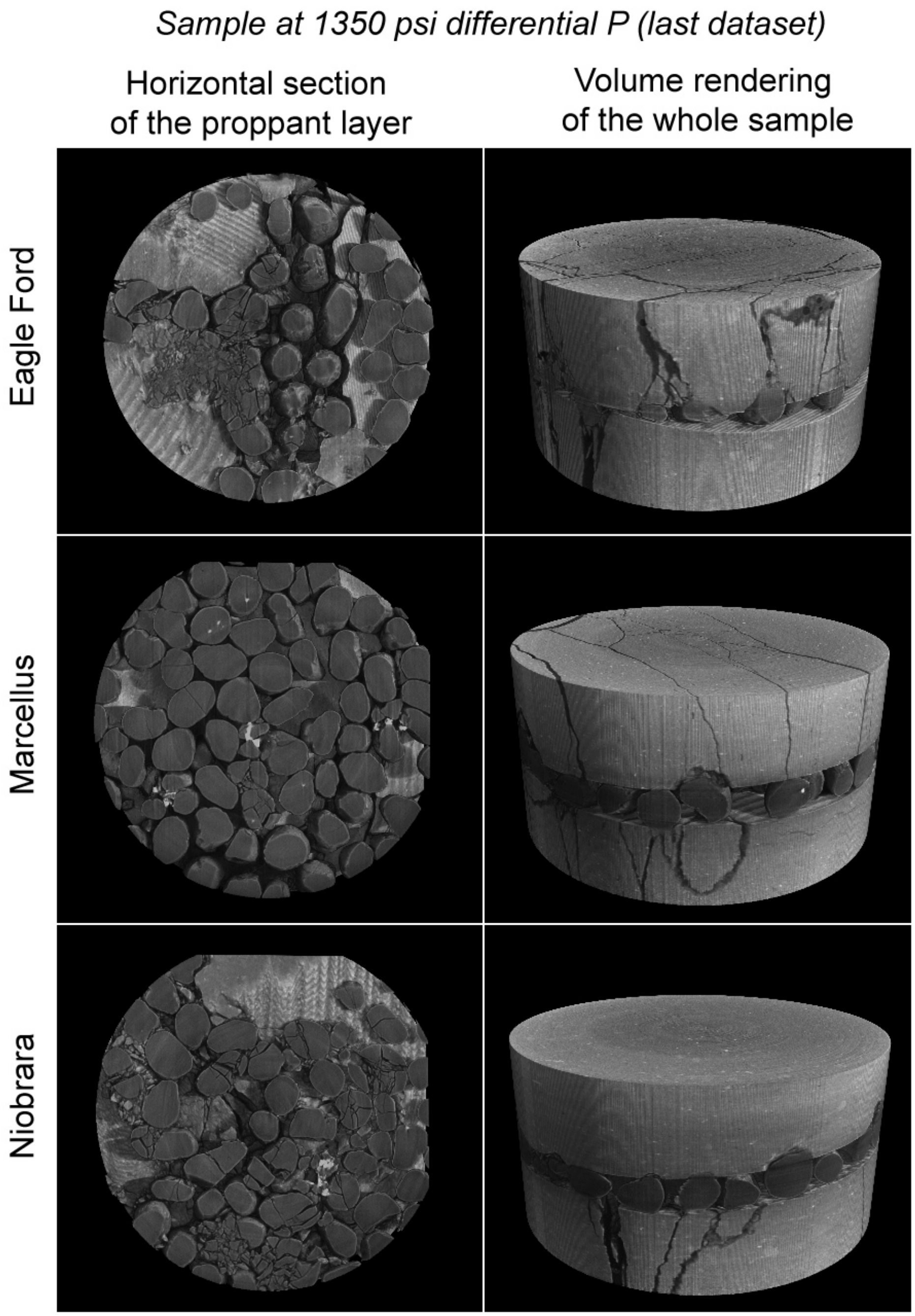

Figure III.1.19: Volume rendering of the three shale samples at the end of the loading cycle. On the left column, a horizontal virtual cut along the propped fracture is shown. On the right column the whole field of view is rendered.

The compression of the sample will rearrange the proppant grains in order to increase the contacts with the top of the fracture, progressively closing this upper layer of fast flow, determining the rapid decrease in the permeability at this stage. The progressive increase in loading will start to break proppant grains and shale at the contacts, making the flow velocity field more similar to the field observed at the bottom of Figure III.1.21a, where all the proppant grains touch the fracture surface. When the fracture collapses, the permeability dramatically decreases and the only flow left occurs between the more intact grains, as shown in Figure III.1.21b. This figure is also important to show the role of microstructure and mineralogical composition in the behavior of the fracture and consequently in the evolution of its hydraulic properties. In the portion of the fracture enriched in carbonates (mechanically stronger), the proppant is shattered and there is no space left for flowing. On the other hand, in the mechanically weaker part of the sample, the proppant, is less prone to breakage, and induces breakage on the shale: this behavior allows some flow around the proppant grains, and a small amount of flow can also appear in the newly-generated fractures. In Figure III.1.21c the permeability evolution curve for this sample is plotted, with the colors labeling the main different behaviors observed during closure.

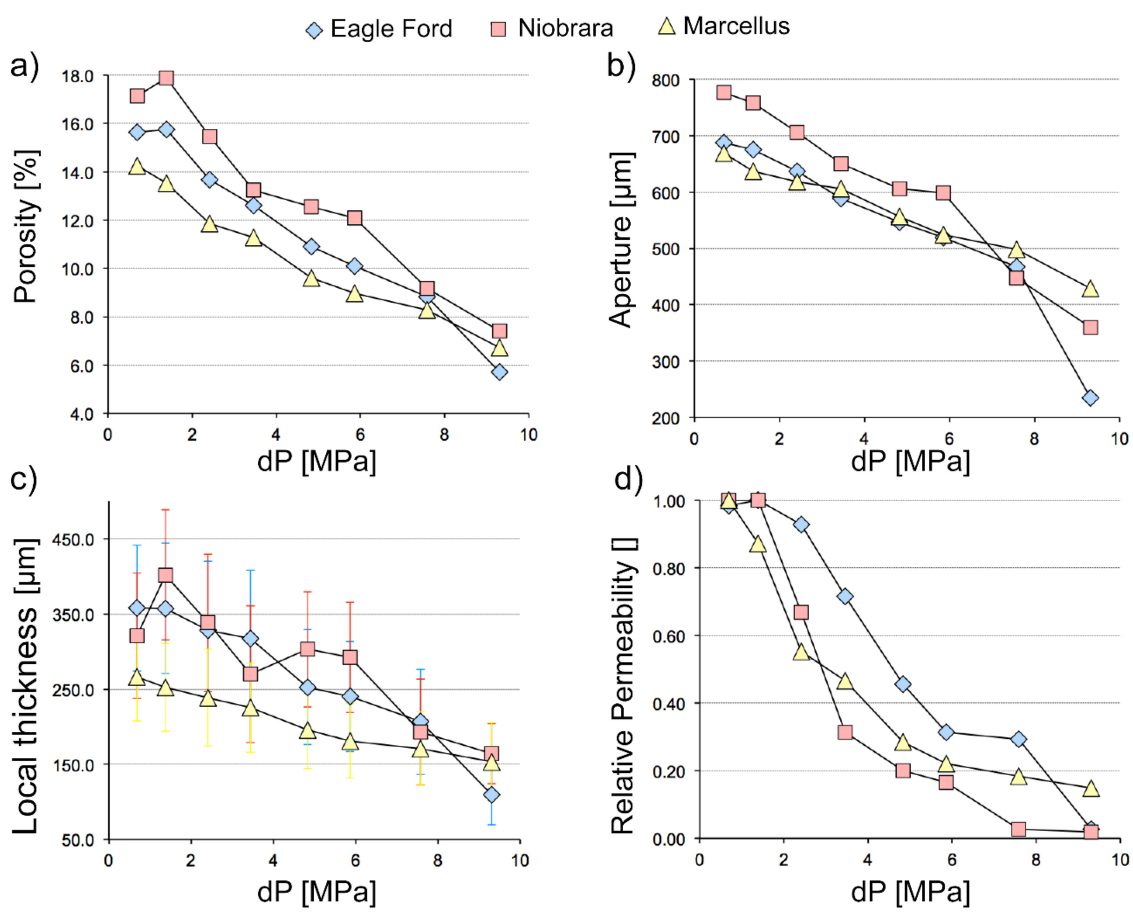

Figure III.1.20: Plots summarizing the results of the morphometric analyses and permeability simulations on the three samples.

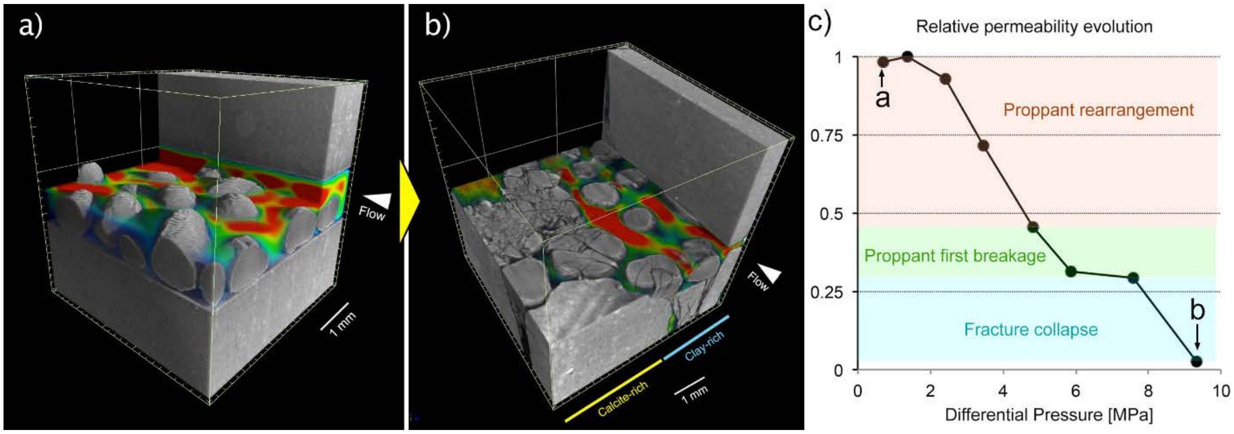

Figure III.1.21: Stokes velocity flow in the sample at the beginning (a) and at the end (b) of the loading experiment on the Eagle ford shale sample. In (c) the permeability plot with the different events highlighted is shown. The volume rendering is displayed in grayscale, while the Stokes velocity fields (rescaled for each sample) are displayed in color, where hotter colors mean higher flow velocity.

Role of the bedding orientation

For the Niobrara sample, we repeated the confined loading experiment with cores cut in orthogonal directions. Macroscopically, the Niobrara shale sample we used did not display clearly anisotropic features, but at the microscale, a lenticular structure made of calcite-rich lenses surrounded by clay, lithics, and organic-rich material is present. We wanted to study how these structures have a role in the mechanical response when loading a propped fracture and ultimately how this behavior influences the hydraulic properties.

As a first step, just by observing the vertical sections in the volume renderings in Figure III.1.22 some differences in behavior appear clear. The sample with the bedding vertical (Figure III.1.22a) displays a more pervasive fracturing, and the behavior at the proppant-shale contacts is markedly different, compared to the sample with the horizontal bedding (Figure III.1.22b). While the main fractures start from the proppant-grain contacts and propagate sub-vertically, the microfractures triggering these events are different: in the case of vertical bedding, a “wedge” of subvertical microfractures and fines is generated, and the proppant embeds and triggers the large fracture. In the horizontal bedding case, the microfracturing at the contact points at the beginning of the events is sub-horizontal, and flat-shaped chips of shale are detached and deposited on the fracture lower surface, before the vertical fracture is triggered and the proppant partially embeds. Also, and more importantly, the pervasive fracturing of the shale and the shattering of the proppant occurs at larger loads in the sample with the horizontal bedding.

When considering the porosity variation trends (Figure III.1.23a), we can still observe a linear behavior. The slope of the linear trends is slightly different, with the vertical bedding sample showing a decrease in porosity at a faster pace. Concerning the aperture variation (Figure III.1.23b) again similar trends are observed, with the Niobrara shale sample with vertical bedding starting at higher values, likely because a larger sand grain was present. The same behavior of a faster decrease in aperture when the breakage phenomena become more frequent at higher differential pressures, as observed with the three samples above, is still present.

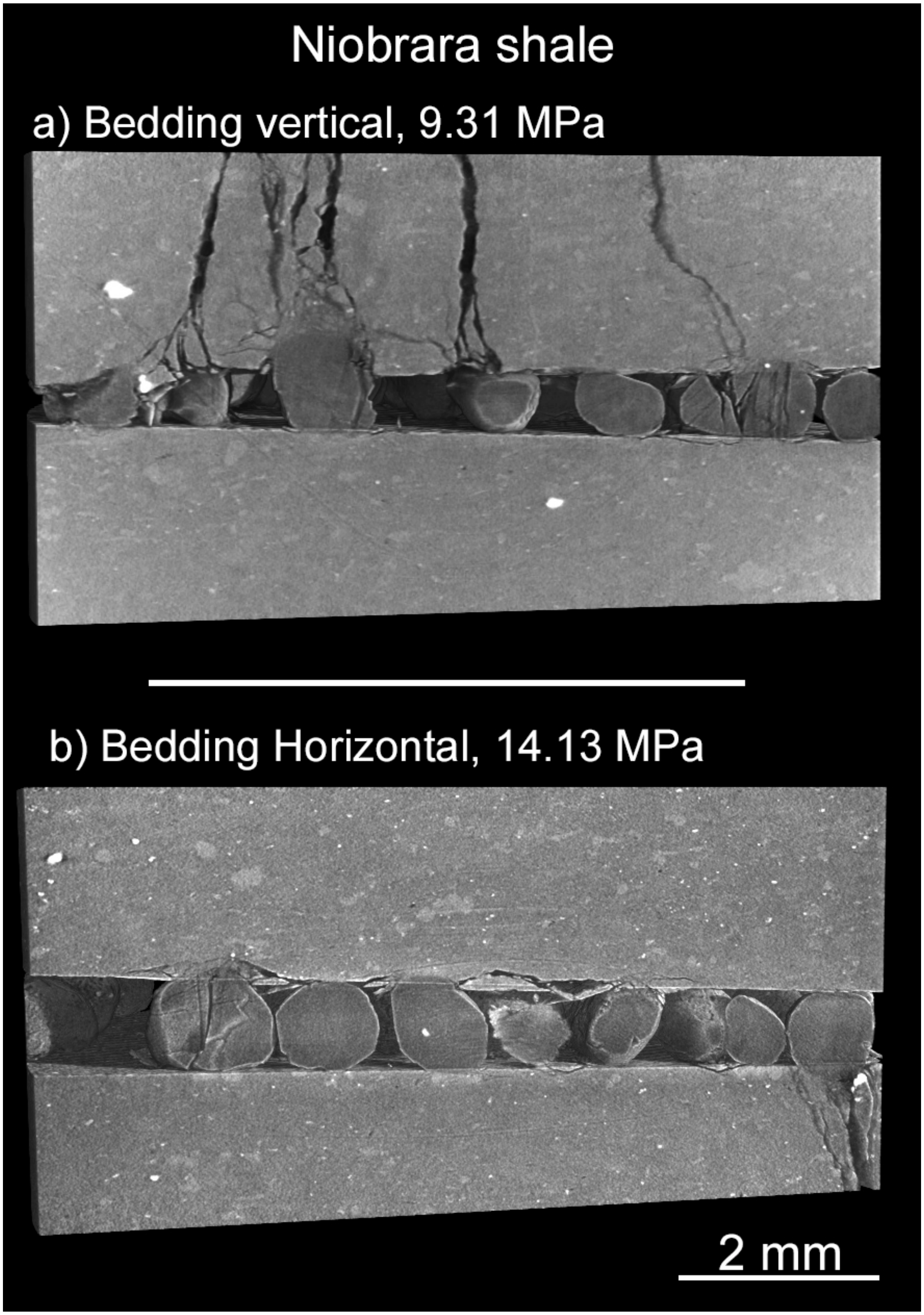

Figure III.1.22: Vertical sections of the volume rendering of the Niobrara shale sample experiments with bedding vertical (a) and horizontal (b).

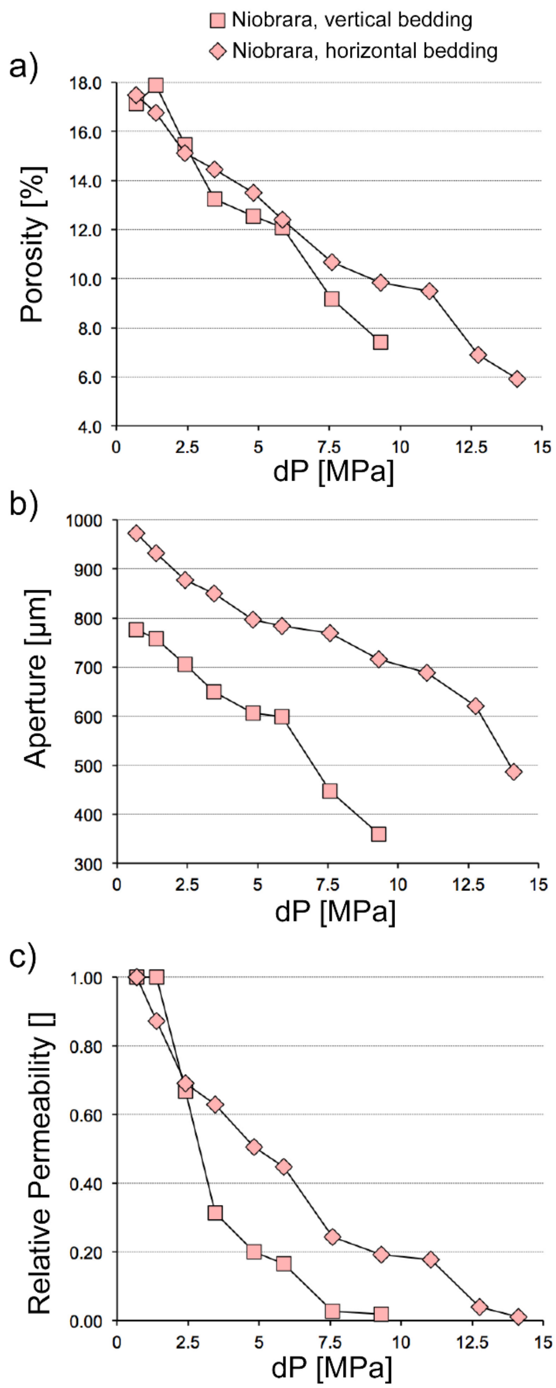

Figure III.1.23. Plots summarizing the results of the morphometric analyses and permeability simulations on the two Niobrara samples with different bedding orientation.

Concerning the relative permeability variation, the sample with the horizontal bedding still displays a curve similar to the other samples, i.e. a rapid decrease in permeability in the first half of the loading sequence, followed by a slowing down of the decrease when breakage start to happen, and a final minor decrease in permeability when the fracture collapses. The difference in slope of the first part of the curve, due to the proppant rearrangement, is due to the starting distribution of the proppant in the fracture and not to the nature of the shale itself.

Role of proppant type

As observed in the previous results, the decrease in permeability -at these conditions- depended on three main factors: proppant rearrangement, breakage events (both proppant and shale), fracture collapse. If the irregular quartz grains are substituted with mechanically harder ceramic spheres, the resulting behavior of the permeability evolution should be very different as well. First, the regular shape of the proppant should minimize the proppant rearrangement. Second, the added strength of the proppant should avoid shattering, the other detrimental effect in maintaining a high permeability observed and discussed in detail for the calcite-rich portion of the sample in Figure III.1.21b. Given the above, a ceramic proppant should be able to maintain its permeability constant for a longer loading interval, until the final collapse.

In Figure III.1.24 the volume renderings of the Niobrara shale samples (horizontal bedding) are shown. These renderings are taken from the samples at the loading step before their collapse, to better show the mechanical response of the sample at high stress. In the top row, the vertical section is displayed to show the interaction of the proppant with the shale: the quartz either shatters or triggers subvertical fractures, and generates substantial spalling, chipping shale fragments. The ceramic proppant just creates a "powdery" material crushing the shale at the contact, and from that regions the subvertical fractures are generated. The horizontal section of the two samples (shown in the bottom row) is cut close to the lower fracture surface to let the bottom of the proppant grains visible. This better displays the processes happening at the proppant contacts with the shale. It is immediately obvious that the behaviors are very different: in the quartz proppant sample several shattered quartz grains are observable, a significant amounts of fragments due to the spalling of the shale is present on the fracture surface, and an irregular distribution of fractures is present as well. On the other hand, in the ceramic proppant sample only one proppant sphere is broken, almost no material from crushing the shale has moved onto the fracture surface (only a single chip is visible on the bottom-right), and the network of fractures is very regular, connecting most of the proppant-shale contact areas. But how these different behaviors affect the morphometric parameters and the hydraulic properties of the sample?

In Figure III.1.25 the results of the morphometric parameters are again summarized. Concerning the porosity variation (Figure III.1.25a), the linear trend observed so far for all the samples is no more present for the ceramic proppant. After a small decrease due to the shale adjustment and a limited proppant rearrangement, the porosity decreases at a very slow pace, until the final collapse of the structure which closes the fracture completely. In the average aperture plot (Figure III.1.25b), the trend roughly follows the one observed with the porosity, with minor adjustments during the first stage of loading, and a final collapse. In this plot the final collapse is not abrupt as in the porosity plot, since the porosity plot takes into account the newly formed space generated by the new fractures (at 12.76 MPa the void space actually slightly increases because of these new fractures), but when the fractures are started, and the tops and bottoms of the proppant started to embed, the aperture value decreases instead, hence the difference in this section of the loading path. The plots of the average LT and σ (Figure III.1.25c) again display very different patterns: the quartz proppant sample displays the typical sub-linear decreasing trend, with σ values decreasing as well. On the other hand, the average LT value for the ceramic proppant follows the trend of the aperture, and its σ are smaller (compared to the quartz sample) and constant, until the final collapse of the fracture. This highlights the more regular and constant topology of the voids space during most of the evolution of the sample.

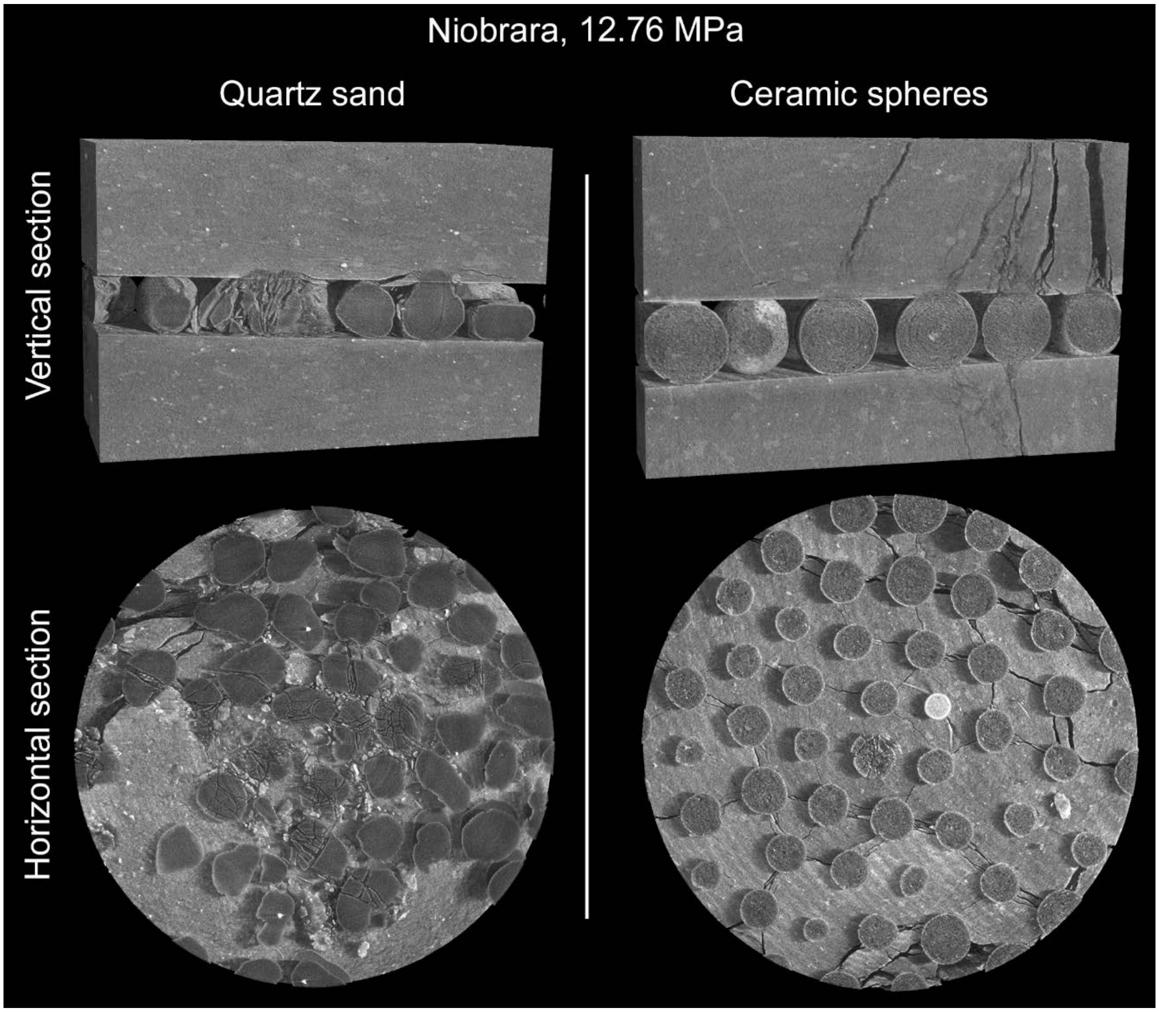

Figure III.1.24. Volume renderings of the experiment addressing the role of proppant type: quartz sand (left column) and ceramic spheres (right column). A vertical section (top row), and a horizontal section cut close to the lower fracture surface (bottom row) are shown.

Concerning the relative permeability variations, the ceramic proppant sample at the very first stage of closure behaves like the sand samples: the fracture surfaces adjust and the proppant starts to move. This minor motion (cfr. aperture values variation) still has a rather strong impact on the permeability decrease because of the closure of the top layer of fast flow, as observed also for quartz grains, and specifically shown in Figure III.1.21a. But while with quartz proppant the grain rearrangement is more continuous, after the first adjustments, the ceramic proppant does not move anymore, therefore the permeability remains constant while its quartz counterpart sample still displays a fast-paced decrease. The presence of this top layer of fast-flowing regions present at the very beginning of the loading cycle is clear in Figure III.1.26, which shows the sample at the beginning of the loading sequence. The hotter colors indicating faster flow regions are concentrated at the top of the sample and in between the grains. A fast flow layer is also present at the bottom of the fracture, but the flow in this part of the sample is lower, being the fracture horizontal: all the proppant grains are touching the lower surface, while the size distribution of the grains dictates how many are touching the upper surface and how much room is left on the top of the fracture. The permeability of the propped sample stays rather constant until the pervasive fracturing event takes place and the fracture collapses. The fracture collapse happen almost simultaneously for the two samples, making direct comparisons easier: the ceramic proppant is evidently able to keep the permeability of the system almost constantly high until the very final collapse of the fracture, after the first adjustment; with the quartz proppant the permeability of the fracture decrease rapidly during the first part of the loading, then slows down until the final fracture collapse. During a hypothetical life cycle with the same constant loading history, the ceramic one would allow a significantly larger amount of fluid (32% more, in our case) to pass, in the case of same starting fracture permeability. In a more realistic scenario where the stress state changes slowly and tends to stay at moderate to high values, the ceramic proppant is generally superior, with a maximum of eight times the efficiency, when the fracture starts to collapse.

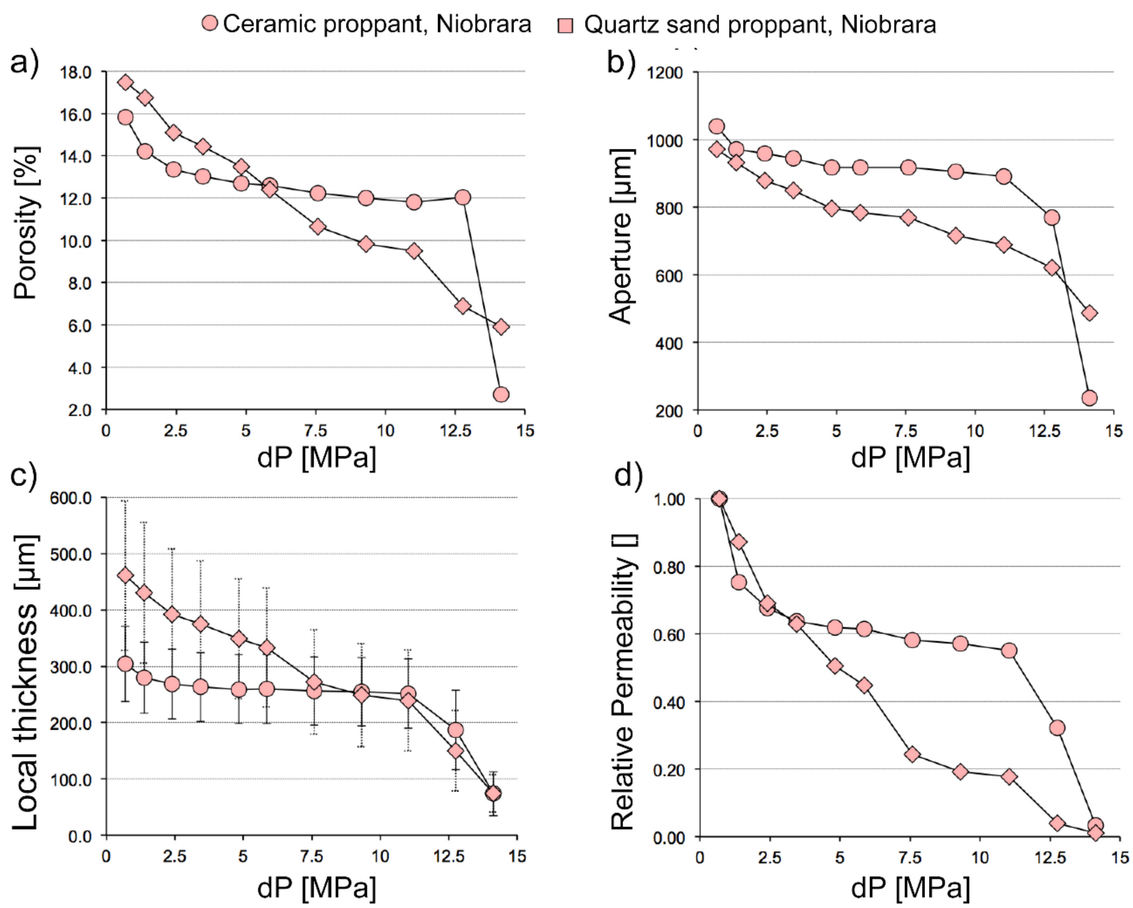

Figure III.1.25: Plots summarizing the results of the morphometric analyses and permeability simulations on the two proppants experiment.

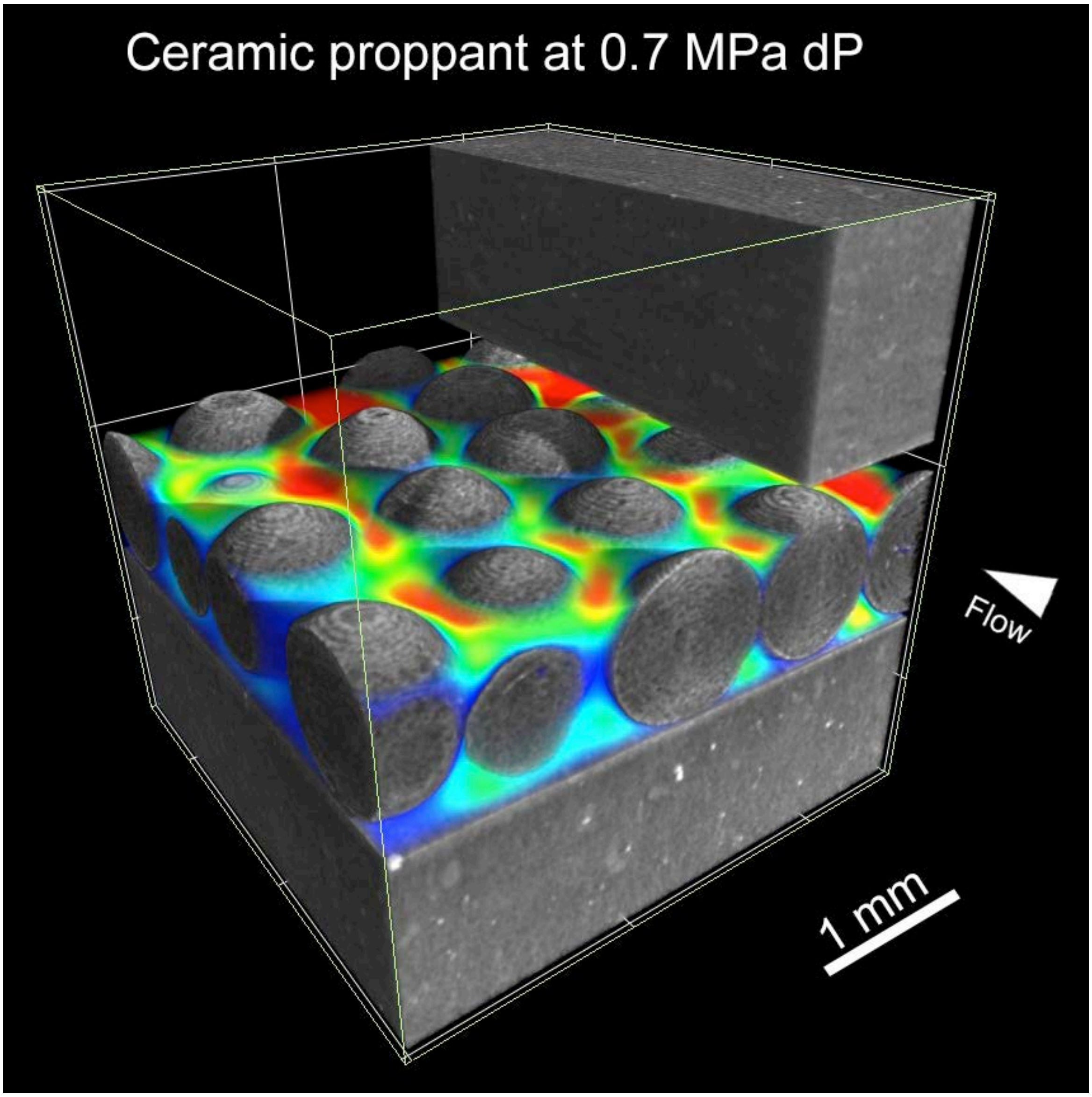

Figure III.1.26: Stokes velocity field (in color) in the sample propped with ceramic spheres at the beginning of the experiment.

Discussion

Concerning the contribution of mineralogy and texture to the fracture behavior during closure, a few points can be summarized: the presence of carbonates acting as a cement greatly increases the mechanical strength of the shale to the point where it surpasses the strength of the quartz sand proppant used in our experiments. The results of this mechanical strengthening are the shattering of the proppant, the generation of fines, and the sealing of the fracture. Where calcite is not as abundant, the mechanical strength of the shale results lower than the proppant. This induces more proppant embedding, more pervasive microfracturing, and better (albeit very low) residual flow capabilities. This mechanical strength threshold is rather evident in Figure III.1.21b. This figure also highlights how compositional/textural heterogeneities play a role at the microscale: proppant seems more prone to embed and propagate microfractures where the contact areas are in layers mechanically weaker (more clays, less cementing carbonates, etc.), highlighting local variations of mechanical response. From a practical point of view, in these cases the use of mechanically strong proppant, able not to shatter in the areas of the fracture which are mechanically strong, would potentially make a large difference, whereas in mechanically weaker samples, the nature of the proppant would be of little importance since the resulting mechanism would mostly be a “brittle” embedding.

The contribution of proppant morphology is another fundamental factor to consider. When looking at the permeability curves, e.g. Figure III.1.21c, the pattern is rather clear: the highest impact on permeability occurs at the early stages and it’s due to proppant rearrangement. This behavior is amplified because of the geometry of the sample in the experiment: a horizontal flat surface will generate a layer at the top of the surface with a very high flow. In theory the aperture of such fracture would be dictated by the size of the largest proppant grain in the vertical direction, and the extent of this high-flow layer by the particle size and topological distributions of the proppant particles. In the real case, the largest proppant grains, contacting the upper surface, get progressively mobilized to better conform to the load. This includes, especially when the load increases, some light chipping and embedding at the contact areas, a mechanism that allows more contacts with grains and a progressive better distribution of the load, shared among more, and larger, contact areas. This first rearrangement is very effective in reducing the upper flow layer, but with fractures with different orientation, the effect of gravity in the starting packing of the proppant grains would be different. The effects due to particle size distributions would be still valid, i.e. in the case of a flat surface, the starting aperture will be set, in theory, by the largest proppant grain, no matter the orientation of the fracture, and with the closure some rearrangement would still happen. A flat horizontal fracture could be considered the upper boundary concerning the importance of this feature, decreasing with the angle with respect to the gravity direction.

From the morphometric analysis of the fractures, different mechanisms can be identified. None of the parameters considered, or their combinations, seem to suggest direct correlations with permeability, for the whole cycle.

Shales can be extremely anisotropic in a large range of properties, including mechanical ones. The orientation of the fracture with respect to the bedding can therefore play a significant role in the response of the proppant. To test this assumption we have used a shale apparently displaying none to weak anisotropy: no banding is visible in the hand sample, like in other shales, but an anisotropic microstructure is present, as described previously. The behavior of the two fractures is different in many aspects, from the behavior of the proppant-shale contact areas to the general fracturing behavior. In the experiment this translated to a better retention of permeability in the sample with horizontal bedding. Observing the permeability curves (Figure III.1.23c), the difference is in the proppant rearrangement portion of the curve (low differential pressure). Once the rearrangement of the proppant is completed, the trend of the two curves become very similar, but with the difference that in the sample with the horizontal bedding it happens at higher differential pressure values. These curves seem to suggest that a similar general mechanism is present, but in the case of vertical bedding it occurs earlier.

It has been mentioned that in the case of a fracture with mechanically strong surfaces, the strength of the proppant would have been a very important factor to keep the fracture flowing. In addition to mechanical strength, the proppant rearrangement proved to be a critical process affecting the evolution of permeability of the fracture. Ceramic proppant is mechanically very strong, and its shape and grain size distribution would make it less prone to rearrangement. From the results section, the plots showed that the influence on the fracture evolution is indeed significant. While the quartz grains move to accommodate the load, the ceramic spheres stay in place. In addition to pure mechanics, the ceramic proppant was also less prone to clumping in mixed-wet systems, making the setting of proppant monolayers easier; proppant surface properties can influence product recovery (e.g. Dusterhoft et al., 2004), but are not considered here, where the focus is on the mechanical interaction of proppant with shale. The generation of the upper fast flow layer, in the case of the ceramic proppant, was due only to the gravity coupled with the classing of the spheres. This resulted in a weak reduction in permeability, once the proppant was set, until the proppant started to fracture the shale to a significant extent, while the quartz proppant kept decreasing in permeability. While in the sample with sand the evolution is relatively gradual (for all the parameters considered: porosity, aperture, average LT, permeability), until collapse, in the sample with ceramic proppant the evolution is divided clearly into three parts: 1) the system starts to accommodate the load, with minimal movement of the proppant and fracture surfaces. 2) Long and stable interval where all the properties remain roughly constant. 3) Catastrophic failure of the system, with pervasive fracturing of the shale and embedment of the proppant. As from the plots in Figure III.1.25, the flow properties of the ceramic propped fracture stay optimal for a very large range of differential pressure.

The results of the experiments presented here highlight that the ceramic proppant has two clear advantages: 1) The regular shape decreases the permeability loss due to proppant rearrangement. 2) The high strength avoids proppant shattering. While this latter advantage should be significant only in shales stronger than the quartz sand grains employed, the former is more universal, being unrelated to the nature of the shale and proppant but only to its morphology. Another factor worth considering is the absolute permeability: in the experiments proposed here, the calculation of the permeabilities has been performed in sub-volumes with a similar number of grains (16 to 20) cut from the center of the samples. The permeability values are presented as relative permeabilities to highlight the changes and the patterns within each variable. When considering the absolute values for permeability in the experiment targeting the two different proppants, the quartz propped fracture is almost three times more permeable than the ceramic propped one, at the beginning of the experiment. This is due only to the much more pronounced upper layer of fast flow, due to the presence of the irregular-shaped and different sized proppant grains. Therefore, when looking at the general trends, the ceramic is clearly superior, but when considering the absolute values, the gravity-driven generation of the fast flow top layer plays a very important role. The problem of this last statement resides in the fast flow top layer, which is the result of having a flat and horizontal surface: fracture orientation with respect to the gravity and fracture topography would play an important role on the generation of such a feature in more realistic and larger scale scenarios, therefore it is not as generalizable as the mechanical response is.

Subtask III.1 Conclusions

This subtask addressed the microscale behavior of propped fractures in shales during closure. Three variables were considered: 1) Type of shale, 2) Shale bedding orientation, 3) Type of proppant. The results suggest that composition and microstructure of the shale have a significant impact on the behavior of the proppant and consequently on the resulting hydraulic properties evolution of the fracture. This is especially true when the strengths of the proppant grains and of the shale are similar: shattering vs. embedding of the grains yields rather different results, as we have directly observed in a sample (Eagle Ford) where the strength of different layers were either above or below the strength of the quartz grains. In our experiments, the main factor producing a drop in permeabilities of the fractures occurs at the early stage of closing and it is due to the proppant rearrangement in the fracture. This drop in permeability is due to a high flow layer due to the geometry of the experiments that quickly becomes less important during the closure process. The extent of this layer is expected to be variable, depending on the fracture orientation (gravity effect), fracture topography, and proppant size distribution, etc.

The role of the orientation of the fracture with respect to the bedding of the shale does not impact the shape of the permeability curves in the ~second half of the closing process (the part of the curve which depends more on the shale mechanical properties rather than the proppant rearrangement), but it impacts when the fracturing events leading to the final collapse occur. The fracture oriented parallel with respect to the bedding is less prone to develop pervasive fractures at a given load, but it's more likely to display chipping and spalling on the contact areas, with the subsequent generation of debris and fines.

When comparing the two types of proppant, the ceramic spheres showed two main advantages: 1) Less prone to rearrangement (no extensive drop in permeability with small differential pressure), 2) High mechanical strength (no shattering causing the fracture to close and sealing with fines). The results seem to suggest how the ceramic spheres should work better than quartz sand, especially in environments where high stress and mechanically strong shales are involved.

The coupling of SXRμCT with morphometric analysis and modeling of the hydraulic properties proved to be a very useful approach in studying the behavior of propped fractures at the microscale. Especially interesting is the ability to link the different events happening in the fracture during closure (proppant rearrangement, proppant embedding, etc.) to specific responses in the morphology of the system and -finally- at its hydraulic properties. This combination enabled to separate, and quantify, the different contributions and can be used to develop and evaluate new proppants and more site-specific strategies for optimizing tight hydrocarbon recovery. The "from micro to macro" approach to better understand the evolution of propped fractures seems to be a winning strategy, since the mechanical response of the fracture when closure is induced depends on the combined effect of the proppant-shale contact areas, which are very small in size; to understand the context, i.e. fracture density, distribution, orientation, etc. in a given site, large scale measurements are needed, especially appealing are techniques such as microseismic imaging (e.g. Maxwell, 2011), which are able to provide such information. This combination could provide a unique kind of complementary information enabling new predictive tools needed to optimize tight hydrocarbon recovery.

Subtask III.2: Laboratory Studies of Light Tight Oil Production Techniques

Objectives

The objectives of the laboratory work performed in this subtask are to: 1) perform quantitative laboratory tests to investigate and quantify differences in possible light tight oil (LTO) production techniques suggested by numerical investigation, 2) provide feedback to simulations, and examine proppant behavior in crooked fractures. Additional studies were also performed examining shale and possible behavior at the micro and nano scale including Synchrotron Infrared NanoSpectroscopy (SINS) on samples to identify the spatial distribution of chemical groups in the shale.

Production techniques

LTO production techniques currently considered include depressurization (liquid phase only), depressurization with gas production and gas expansion, fluid dissolution into oil and subsequent production, water-flood, and surfactant flood.

In depressurization, fluid expands upon the lowering of pressure and “spills” into fractures where it flows to wells (Figure III.2.1). In depressurization with gas expansion, the depressurization results in the fluid expansion as before, but additionally formerly dissolved gas exsolves from the oil and expands into pores driving additional oil out adding to producible oil. In fluid dissolution into oil, an oil soluble fluid is introduced. This fluid has a low viscosity and low boiling point such as scCO2 or propane. Upon mixing, the oil flows more easily and is easier to produce. Subsequent depressurization with possible gas production from the introduced fluid will drive more oil into fractures. Water flooding relies on the imbibition of water into the water-wetting portions of the rock displacing oil. Surfactant flooding relies on injection of a surfactant that will reduce the interfacial tension allowing greater oil drainage.

Each of these techniques has drawbacks and uncertainties. Included in these are that depressurization and depressurization with gas drive depend on the very small fluid compressibility (less so for gas drive), the small increase in effective stress, and the low rock permeability, thus is rock block size dependent as well. Fluid dissolution depends on mixing with the oil in place. In the very stagnant pores, mixing will be limited to diffusion, unless other interfacial or chemical gradient driven processes are present. Because water flooding depends on water imbibition to drive out oil, it is doubly dependent on permeability (fluid in and fluid out), but also on the different types of permeability as the oil and water phases may access pores with different wettabilities. Liquid-phase surfactants also suffer from transport limitations. Interestingly, if a reasonable gas-phase surfactant were available, it might access the desired interfaces more easily, however a drive mechanism will also be needed.

This leads to the development of strategies that might be used. An example might be initial production from depressurization, with secondary production enhanced by repressurizing with gas and shutting in the well to allow dissolution into the oil and further depressurization.

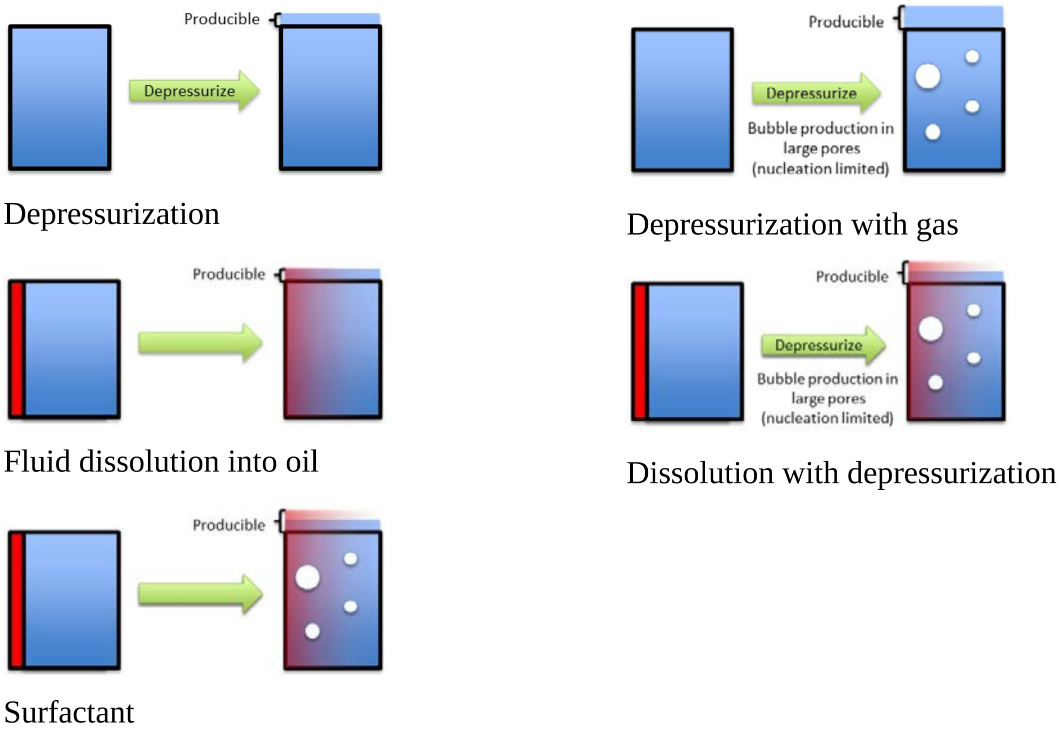

Figure III.2.1: Schematic representation of LTO production methods.

Regarding laboratory tests, quantification of *processes* is important, and laboratory space and time scales must be considered. Using depressurization as an example, oil expands on depressurization and flows into lower pressure fractures. If porosity is assumed to be 5%, oil saturation 50%, compressibility (e.g. dodecane at 293K) 8.63×10^{-5}/MPa, then depressurizing $1 m^3$ of shale by 1MPa will eventually produce 2.15 mL of oil. This amount is quantifiable, but requires a huge relevant sample, long time, and the ability to collect a pristine, yet well characterized sample. Comparison to other processes would be daunting and the error bars high.

Preliminary Laboratory Tests

Supercritical CO_2 extraction of Niobrara Shale

We obtained a large amount of Niobrara outcrop shale from a mine outside of Denver, Colorado. The shale is in relatively large blocks (Figure III.2.2, roughly 10 kg each) and appears extremely competent for shale. By itself, the shale has a very mild oily smell, however when breaking the shale, it has a heavy oily smell similar to that of a rail yard. It is clear from Figure III.2.2 that light color veins (likely calcite – see below) run through the shale showing potential current and former fluid flow pathways.

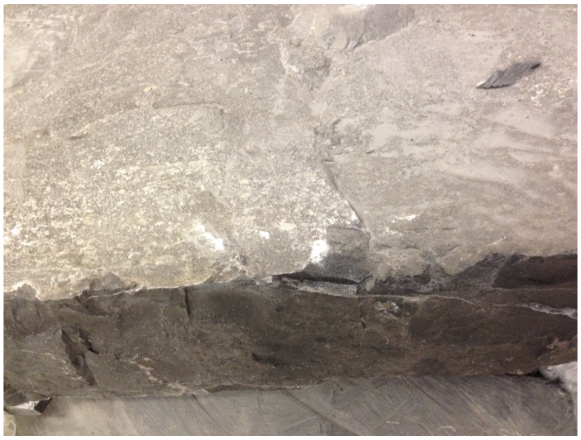

Figure III.2.2: Photos of half-meter scale Niobrara shale block. Left-broken on bedding plane, right-saw cut.

A smaller (on the order of 12 cm x 12 cm x 12 cm) piece of rock was scanned using a medical X-ray CT scanner to examine the rock structure at the submillimeter to centimeter+ scale. A slice from the CT scan of the shale is presented on the left side of Figure III.2.3. The CT scan was calibrated to density using a calibration curve based on CT scans of materials with known density. This density calibration is somewhat approximate, because heavy elements skew the data towards higher values and corrections can be made when the full elemental composition of the rock is known. From the CT scan, the bedding density variations can be extracted (right side of Figure 3) showing layers about 2.5 mm thick. These layers may vary in porosity, pore size distribution, permeability, oil content, and wettability, and their importance will become evident over time. Brighter, high-density veins run through the shale. From the CT densities, these features are consistent with calcite composition.

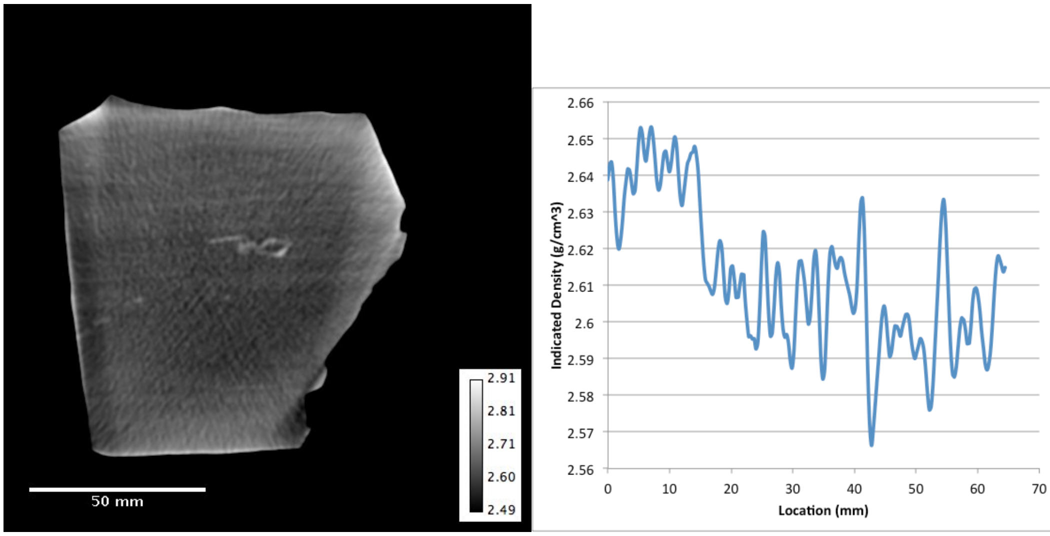

Figure III.2.3: left - calibrated CT scan showing layered structure of the shale with density in g/cm^3. The white curves inside the shale are thought to be calcite veins. right - densities across a vertical profile of the block.

Characterization of the shale sample via SEM/EDS and XRPD

The combination of scanning electron microscopy (SEM) with energy dispersive spectroscopy (EDS) and X-ray powder diffraction (XRPD) provides a first comprehensive characterization including mineralogy, chemical composition, texture/microstructure present in the sample.

For the SEM characterization two samples were prepared:

1) A sample broken along the slaty cleavage plane, subparallel to the bedding. This allows the morphological characterization of the phases and the planar features (scattered electron - SE imaging) of an undisturbed surface.
2) A sample with a face cut and polished ~perpendicular to the bedding plane. This allows a better characterization of the microstructure/texture, better back scattered electron (BSE) images, and more reliable energy dispersive spectroscopy (EDS) analyses.

The XRPD experiment has been carried out measuring a fragment crushed and pulverized from the same shale block, following a conventional procedure for lab XRPD measurements. The analysis of the XRPD profile was done with the Rietveld method, thus providing quantitative information about the bulk mineralogy, complementing the information obtained with SEM/EDS.

Electron microscopy

The broken surface shows wavy structures at the tens of μm scale (Figure III.2.4), with clay particles following the direction of these planes. Carbonates-rich structures also follow these structures (Figure III.2.5). Organic-rich particles can be found scattered on the surface. One (highlighted by the yellow arrow in Figure III.2.6) is close to what seems to be a weathered feldspar pseudomorph.

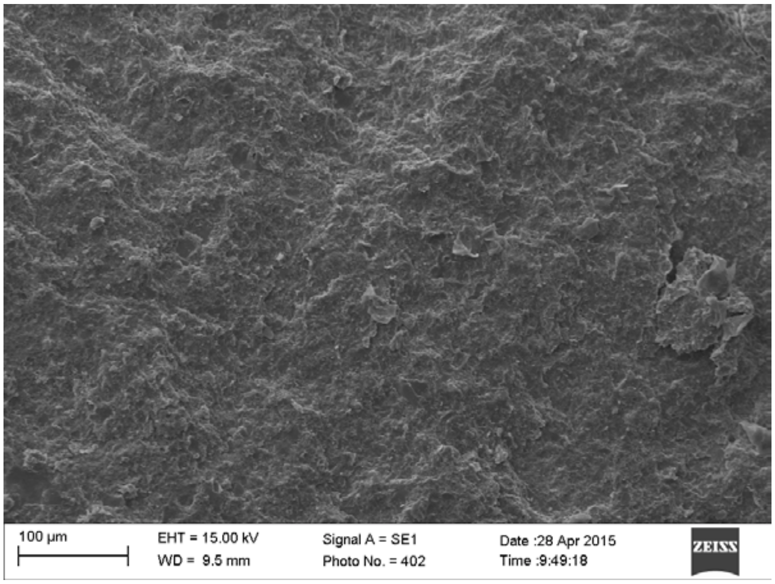

Figure III.2.4: Topography of the sample at low magnification showing more of the topography of the sample.

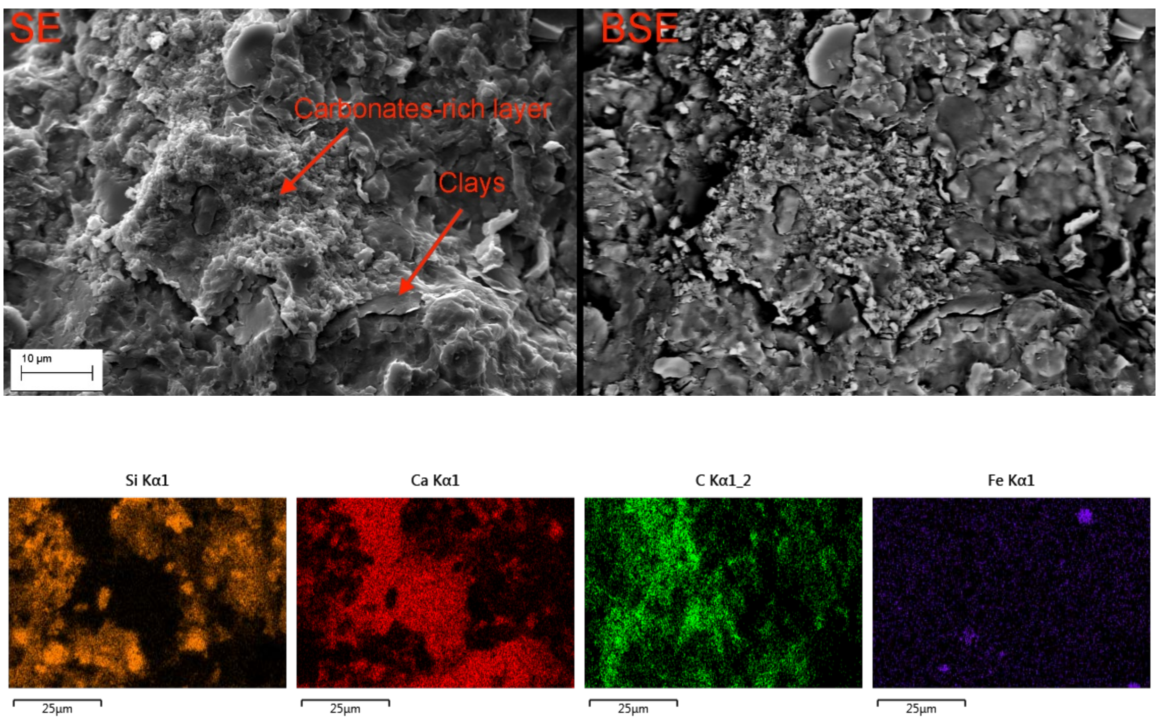

Figure III.2.5: Elemental maps of significant elements showing the distribution of the phases (some effects are due to the sample topography).

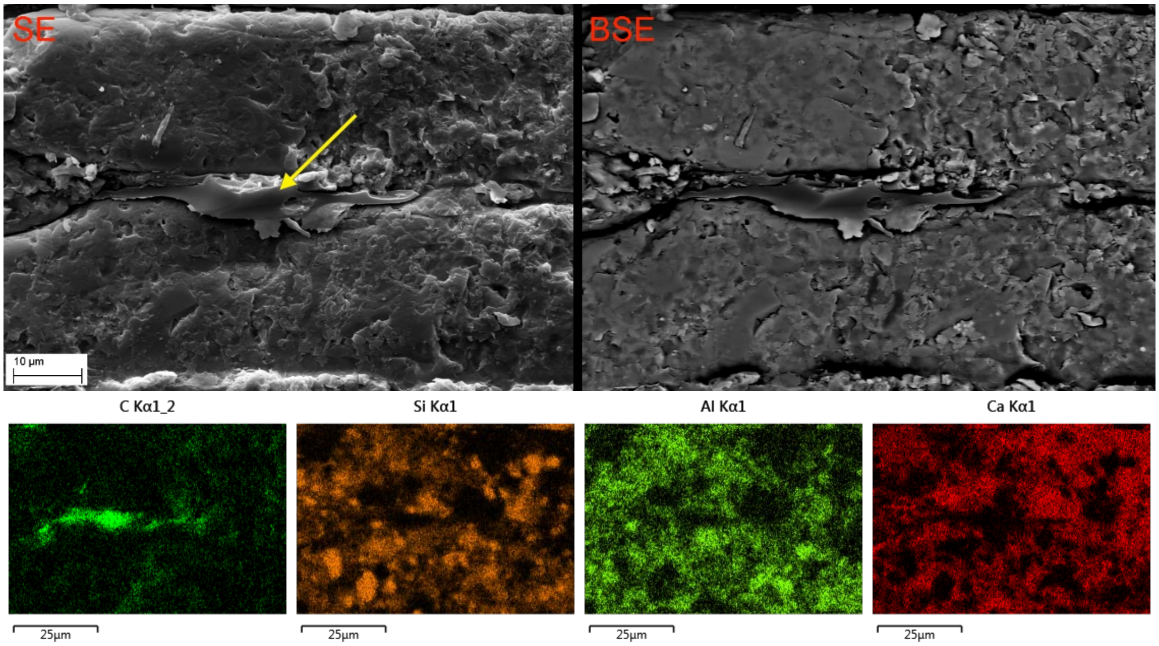

Figure III.2.6: top – organic-rich particles shown with SE and BSE. bottom - The EDS maps confirm the carbonaceous composition of the particle. Organic material highlighted by the yellow arrow.

The sample cut and polished on a plane perpendicular to the bedding plane shows the layering and the textural features of the sample much better (Figure III.2.7). This shale has a very high carbonates content (mainly calcite) and the texture is strongly influenced by the presence of the carbonates. These are diffused in the shale, with some micrometric lenticular structures enriched in calcite. Some larger scale layering is also present, with carbonates rich-layers (where calcite highlights small lenticular structures surrounded by clays and quartz). The microporosity seems to be related to the calcite content: where the calcite content is higher, the microporosity seems to be low (see BSE images). Some fine cracks healed with (often sparry) calcite are also present. In Figure III.2.7 the bedding direction is roughly vertical.

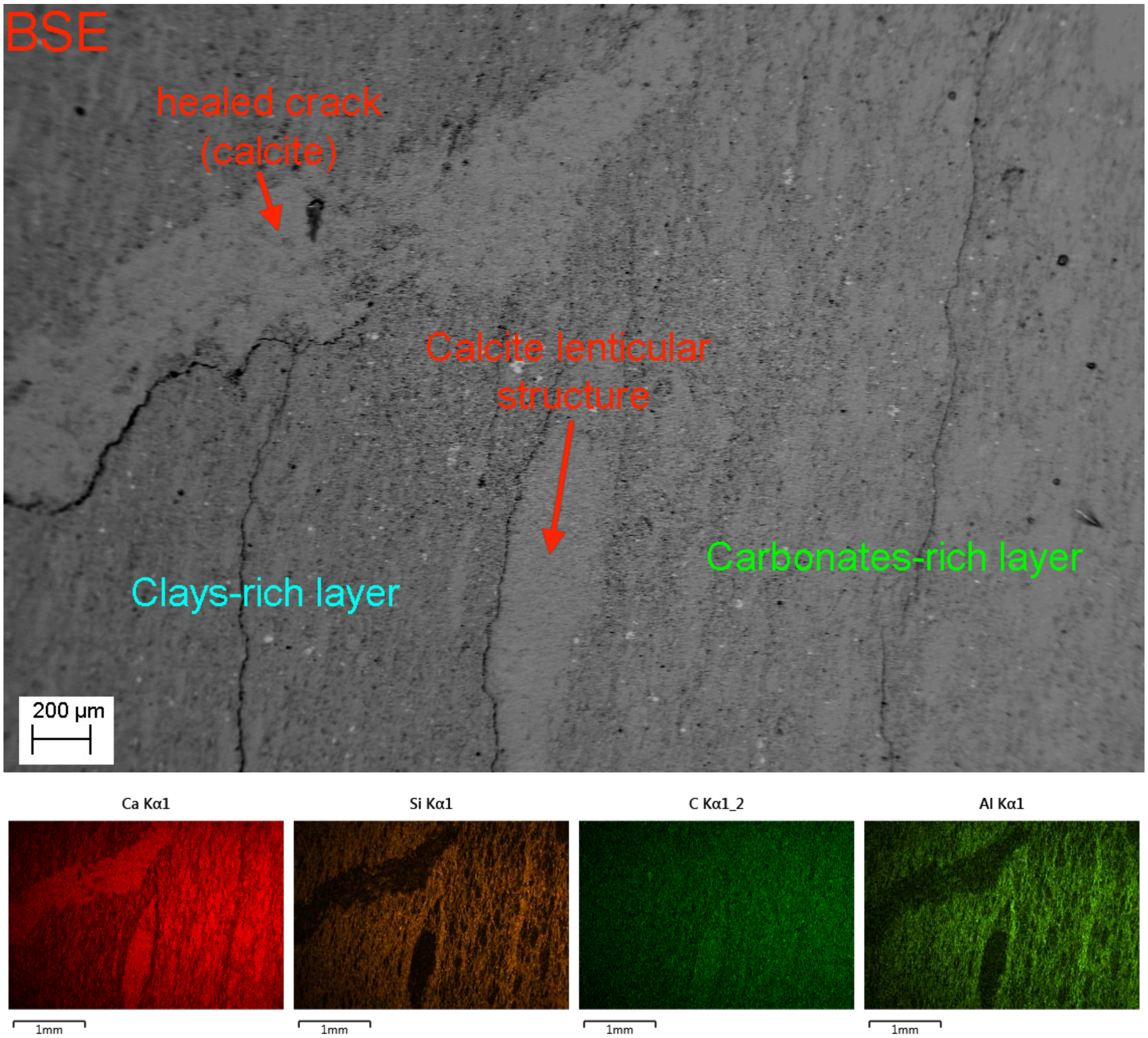

Figure III.2.7: top – Structure identified in the saw-cut sample. bottom - The EDS maps highlight the texture present on this sample, mostly due to the distribution of calcite (see Ca elemental map).

Organic-rich particles are also present (Figure 8. BSE images and EDS maps, with a zoom of the particle):

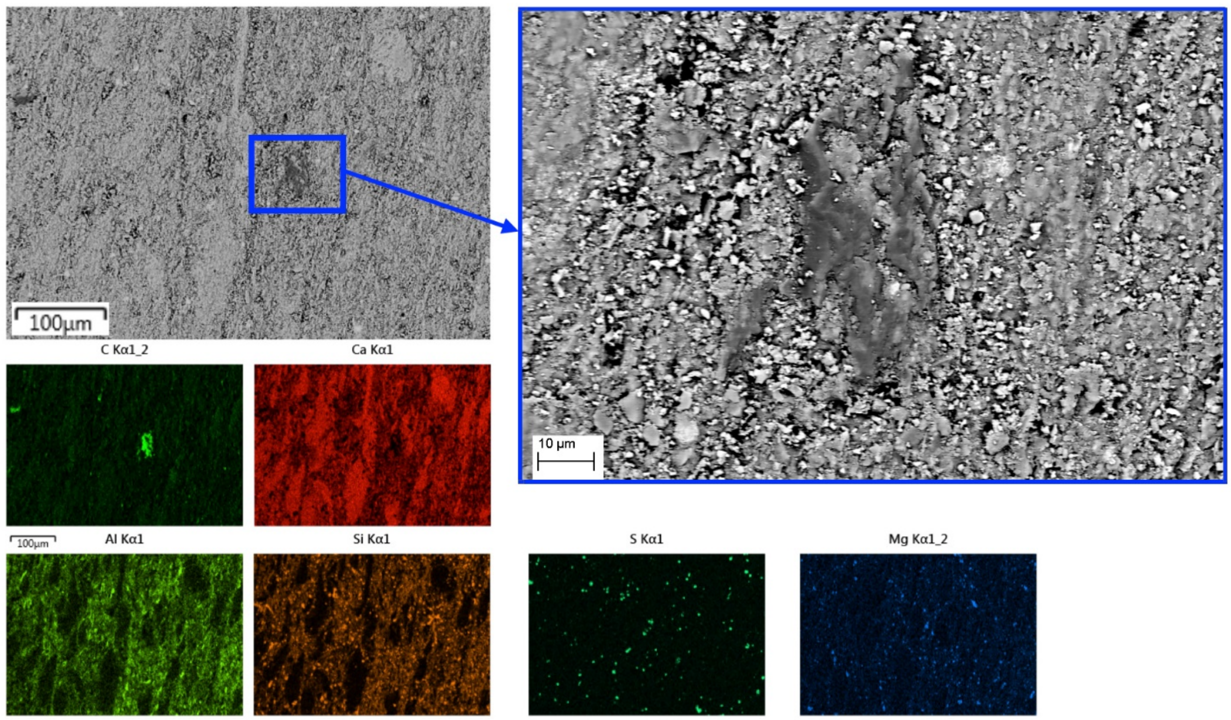

Figure III.2.8: Images from the cut and polished sample.

From the SEM analysis different accessory phases have been identified including: dolomite, pyrite (including typical framboids), and sphalerite/greenockite.

X-Ray Powder Diffraction analysis

For consistency, a fragment contiguous to the sample analyzed was chosen and ground for a XRPD analysis. The XRPD profile has been analyzed via Rietveld analysis to obtain quantitative information about the mineralogy of the sample (see section III.1.1).

Lattice preferred orientation has been considered for phyllosilicates and carbonates. Turbostratic disorder for the smectite has been considered as well.

Figure III.2.9 shows that the carbonates (mostly calcite) comprise slightly more than one half of the sample by weight. The crystallinity of this calcite is not very high (meaning not as high as in sparry calcite), as it is possible to interpret from the peak shape function and from the sample preparation (top loading sample holder for XRPD) that did not induce appreciable CPO. This confirms the observation from the SEM where the calcite looks more micritic in nature.

Table III.2.1: Composition of the Niobrara shale.

Quartz	*14.6(2)*
Smectite (~14Å)	*6.6(4)*
Plagioclase	*3.5(3)*
Calcite	*48.5(3)*
Dolomite	*6.8(2)*
Pyrite	*2.1(1)*
Detrital mica - illite (modeled with a muscovite 2M1 structure)	*17.5(4)*

The measured and the calculated profiles are in good agreement:

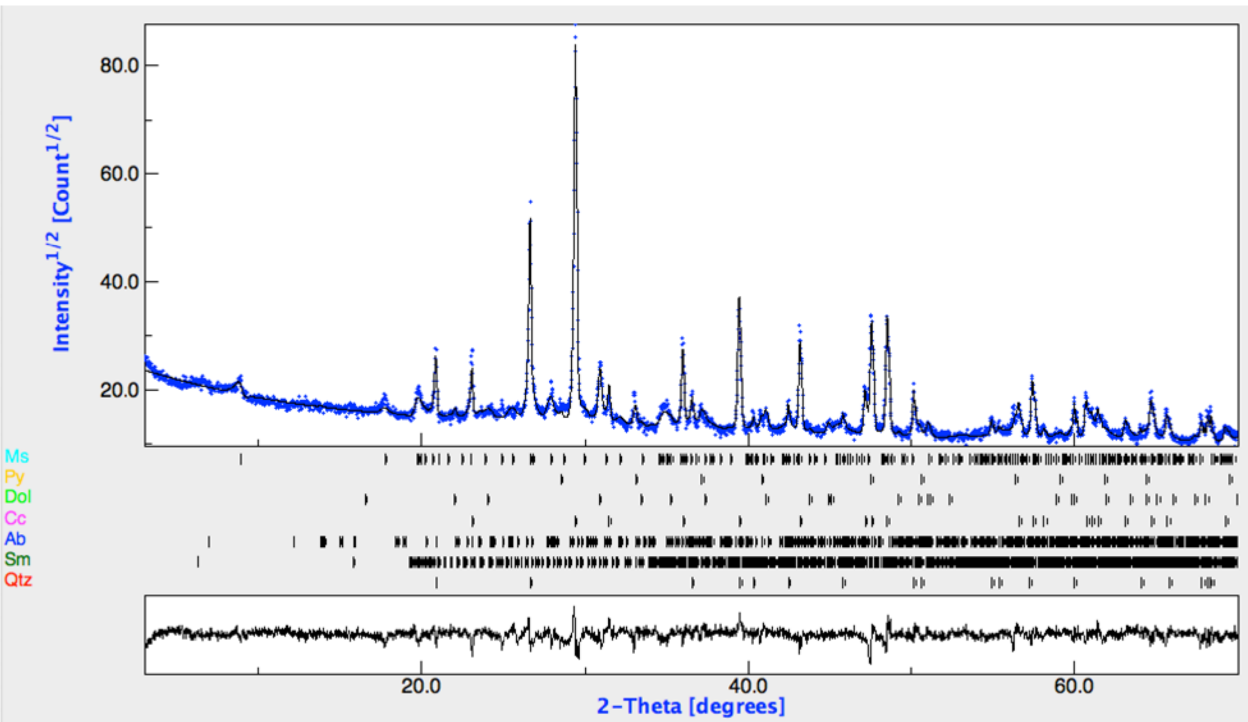

Figure III.2.9: XRPD analysis of the Niobrara shale.

As from this preliminary characterization it is possible to see that this shale is very rich in carbonates (mostly calcite, with some dolomite), distributed in layers and in micrometer lenticular structures. The presence of the micritic calcite is also related to the microporosity of the sample. The clay amount is typical of many shales, with smectite (with significant structural/stacking disorder) and detrital mica, while other phyllosilicates such as chlorite and kaolinite seem to be absent.

Organic-rich particles are scattered throughout the sample, and do not seem to follow the bedding by forming thin and flat structures like in many gas shales. Also, no significant porosity is visible at the magnification used for imaging.

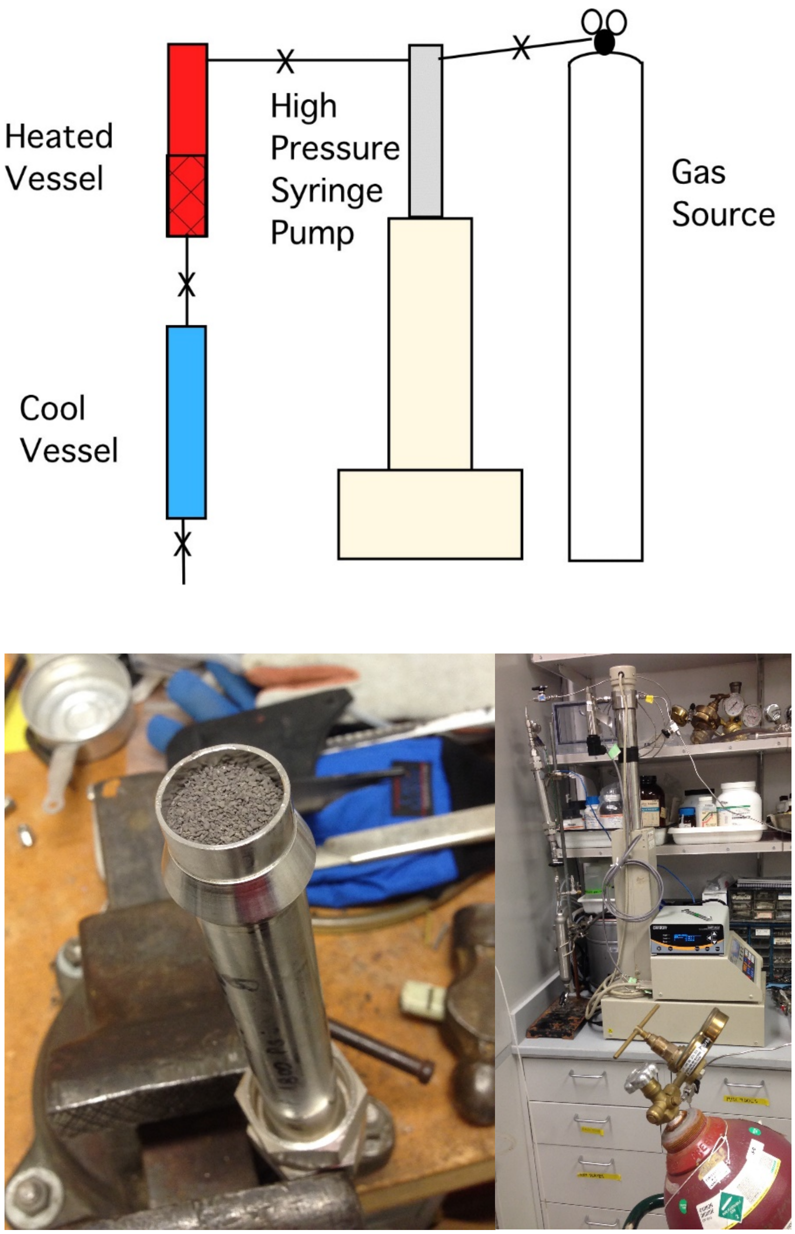

Figure III.2.10. top - Scoping experimental apparatus schematic, bottom left – vessel containing crushed Niobrara shale, bottom right – experimental setup (heater removed for clarity).

Initial experimental determination of LTO production

Experimental Apparatus

To test oil extraction techniques from the shale, crushed shale was placed in the upper portion of the heated vessel and then the vessel sealed (Figure III.2.10). The vessel was filled with pure supercritical CO_2 (for scoping, our operating conditions were 60C and 1300 psi), and the shale was allowed to "cook" for a specified duration (~1 week). Following that, the fluid from the heated vessel was flowed into the lower cool vessel, the CO_2 was slowly vented, and the collected material extracted for analysis.

We performed a test to give us a preliminary understanding of producing oil from shale. We constructed a system to extract oil from an outcrop Niobrara shale sample. We crushed the shale to maximize the surface area to volume ratio and allow rapid mass transfer. The shale was placed in a pressure vessel and supercritical $scCO_2$ was applied for a week to the heated vessel. Following that, the vessel was slowly drained into the cool vessel below the heated vessel. The vessel was depressurized through water. After venting, the vessel mass was slightly greater and the water developed a clean oil sheen.

Although the $scCO_2$ extracted oil from the shale, a number of issues were identified. Included are that only a small amount of oil was produced from a very poorly characterized shale sample. To accurately quantify the oil, another extraction step would be required to remove the oil from the cool vessel, and a better way of collecting the oil compounds in the vented phase would be needed. The oil production would depend on the exact characteristics of each sample, in addition to the technique. With error bars computed, the comparisons would be difficult to make.

Quantitative Experiments

In response to these issues, we redesigned our tests to allow for better comparisons. To do this, a large oil mass compared to the measurement error is desired as well as a known oil with well understood properties, a known pore space, known mineral phase wettability, specified starting conditions, and allowing for lab-scale test durations. We selected a system that uses layers of high-porosity well-studied ceramics with water-wetting surfaces to provide an anisotropic medium that optimizes oil mass vs. measurement error, uses low vapor pressure dodecane as the oil, allows specified starting conditions, and test durations on the order of days to weeks (Figure III.2.12).

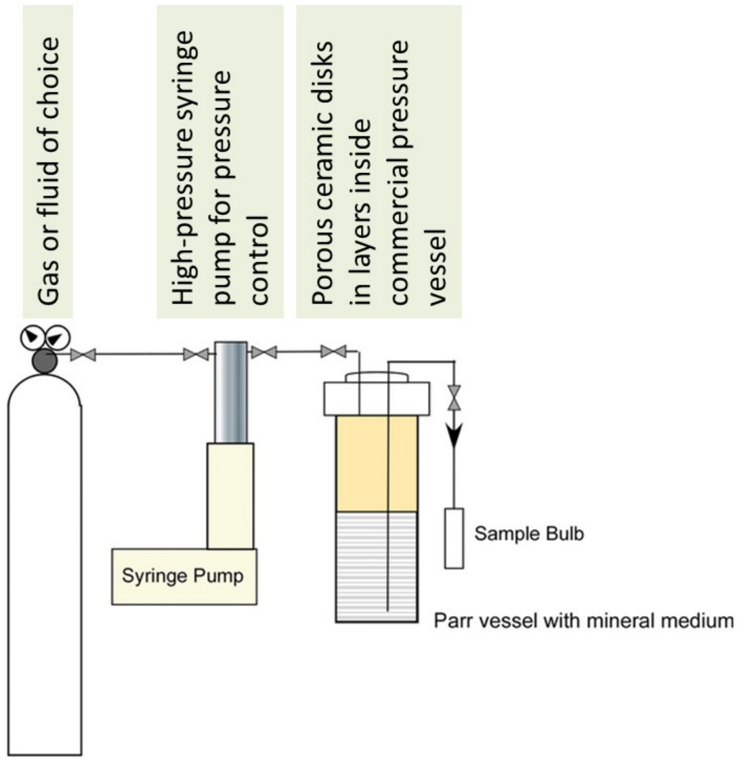

Figure III.2.12: New System. Mineral medium (water-wetting porous ceramic disks) are preconditioned with water vapor, then vacuum/pressure-saturated with dodecane.

Depressurization Tests

To perform depressurization tests, mineral medium (water-wetting porous ceramic disks) was purchased from SoilMoisture Equipment. These discs are manufactured from alumina and are inert to most solutions. The manufacturer specifications give an effective pore size of about 2.5 microns and hydraulic conductivity of 8.6 x 10^{-6} cm/sec. The discs are 5.4 cm diameter, 1 cm thick with a measured average porosity of 48.1%. Prior to pressurization the discs were preconditioned with water vapor by placing them in a sealed container with water-saturated air until the discs reached constant weight, which on average was determined to be 1% water by weight (0.45 g per disc). Although these parameters do not match those of any shale, they allow for a comparison of processes on the time scales of interest.

Using the measured disc porosity, the amount of void space available for dodecane and water absorption is 11.33 cm^3. If 0.45 cm^3 of the void space is occupied with water, then 10.88 cm^3 is available for dodecane. At 1500 psi and converting to weight units this would be 8.1930 g/disc, or 65.5437 g for 8 discs (8 discs were used for each experiment). Masses of the total pore volume of dodecane at test pressures are listed in Table III.2.2.

The purpose of the initial experiments was to evaluate the reproducibility of the experimental system and sensitivity of experimental procedure. All experiments completed have followed the same basic structure. This procedure has been to place 8 preconditioned discs in a standard 600 mL pressure vessel, flood with dodecane to a height which covers all the discs, and pull a vacuum on the system for 30 min to draw air out of the disks. The pressure vessels are kept at room temperature or heated (this is an experimental variable) and both temperature and pressure of the vessel are logged electronically every 20 seconds. Pressure vessels are placed at an angle and dodecane is collected through a stainless steel tube which has an inlet located at the very bottom of the vessel. When sampling, pressure within the vessel drives dodecane from the vessel when a valve is opened, while desired pressure is maintained with a syringe pump. Two pressure vessels were set up to increase the number of replicates and experimental conditions tested.

After addition of dodecane and degassing, the system is pressurized to 1500 psi with the fluid of choice and allowed to equilibrate for a number of hours. Enough dodecane is added so that under pressure and with maximum absorption all the discs are covered with dodecane (no pressurizing fluid/disc direct interface). The dodecane is then allowed to drain under pressure (1500 psi). Initially a large volume of dodecane is drained (on the order of 140 g) and then the system is allowed to sit and slowly drain to collect non-residual dodecane. Once drainage is determined to be complete, the depressurization test is performed by first reducing pressure from 1500 psi to 1000 psi and allowing the system to drain for a minimum of 16 hours. Collection of dodecane is repeated for pressure drops to 500 psi, 250 psi, and 0 psi (vent) until discs are returned to saturated conditions at 0 psi. The first several experiments were disassembled after the experiment to test both amount of dodecane remaining on the discs and well as the efficiency of the dodecane removal technique and it was determined that mass balance of dodecane added/dodecane recovered was greater than 98%. Subsequent experiments were repeated without removing the discs.

In Experiment 1 insufficient dodecane was added so there was a N_2/disc interface after pressurization to 1500 psi which likely resulted in entrainment of pressurized N_2 into the discs and subsequent larger recovery of dodecane during depressurization. Included in Table 3 are times in minutes of each pressurization/depressurization step, as well as the mass in grams of dodecane collected. Measurements in Table 3 were made at room pressure and temperature.

The predicted mass of dodecane that would be produced due to density change upon depressurization only can be calculated. If we assume 65.5437 g with a volume of 87.04 cm^3 is absorbed into the discs at 1500 psi, that same mass will have a volume of 87.3124 cm^3, a change of 0.2724 cm^3, or 0.2032 g at 0 psi. On average from the experiments the amount collected is 0.35 g, or approximately 0.47 mL, 170% of predicted. This may be due to experimental error, but the overproduction of dodecane increases at lower pressures. If the same 87.04 cm^3 is in discs at 1000 psi, then at 500 psi 0.2115 g should be produced, but on average 2.46 g, or 3.30 mL, is collected. When the pressure drops to 250 psi and 0 psi, again there is more production than density changes alone can predict. Overall, on average 8.1 g is produced whereas the predicted mass was ~0.8 g. Therefore in addition to density changes there are other physical processes occurring to produce oil from the discs.

One explanation for the increased production is dissolution and diffusion of nitrogen gas into the dodecane. After depressurization the system is allowed to drain for a specified period of time. During this time the exterior surfaces of the discs are exposed to nitrogen at pressure. The addition of nitrogen into already saturated discs will displace some dodecane, which could cause additional production. However the bulk of the dodecane is collected quickly after depressurization and generally only a small amount of nitrogen is added over the drainage period, so this cannot account for an order of magnitude increase in dodecane recovered. Mixing of nitrogen with dodecane will also change viscosity, surface tension, and density which could potentially increase the amount of dodecane recovered. More investigation is needed to determine the magnitude of these effects, but again these would cause changes over a period of time during diffusion, not instantly when the pressure is dropped. Lastly, and perhaps dominantly, dissolved nitrogen can expand rapidly during depressurization, displacing dodecane during expansion.

If the depressurization and nitrogen gas drive is the mechanism for increased recovery of dodecane, then longer drainage times should increase the amount of dodecane recovered due to increased time for diffusion of nitrogen into dodecane. A series of depressurizations were performed that varied the time the system was drained at 1500 psi (when the discs would be exposed to N_2 gas at 1500 psi) until depressurization at 1000 psi (Figure III.2.13).

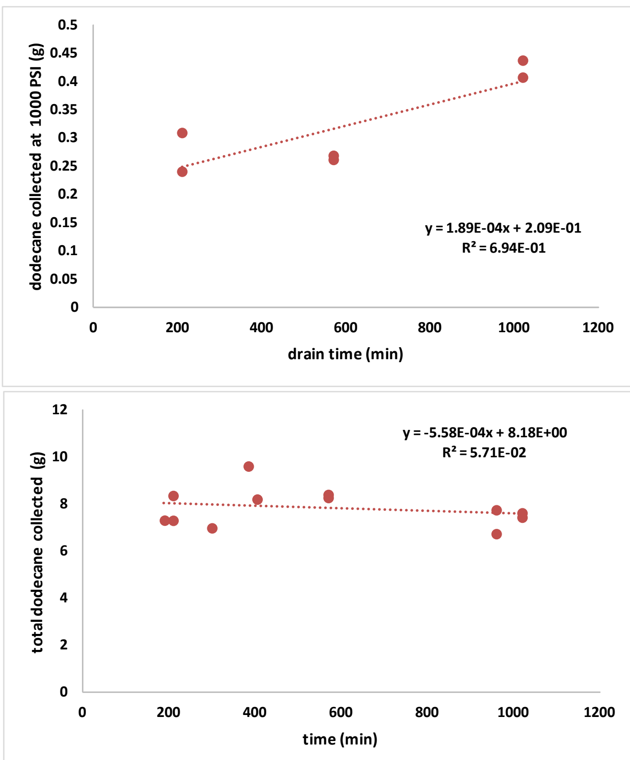

Figure III.2.13: Top - Dodecane produced in the first depressurization versus the initial drainage (nitrogen-dodecane contact) time. Bottom – Total dodecane produced over all depressurizations versus the initial drainage time.

Diffusion rates of gas into liquids is dependent on both pressure, temperature and viscosity of the fluid. To date, a diffusion coefficient for N_2 in dodecane at 1500 psi (10 MPa) has not been found in the literature. Upreti and Mehrora (2002) report a diffusion coefficient of N_2 in bitumen at 25°C of 1.80 x 10^{-11} m^2/s at 4 MPa and 5.55 x10^{-11} m^2/s at 8 MPa. Jamialahmadi et al. (2006) reports a diffusion coefficient for methane gas into dodecane at 10 MPa of 9.0 x 10^{-9} m^2/s. Methane is a bit smaller (FW 16) than nitrogen (FW 28) but these coefficients could be used as a starting point for estimating diffusion rates.

Nitrogen density changes from 0.11981 g/cm^3 at 1515 psia (1500 psig) to 0.0808 g/cm^3 (Table III.2.4) at 1015 psi which is a more significant change in volume than dodecane over the same range. Using this to account for the excess recovery of dodecane of about 0.2 mL, 0.01586 g of N_2 would have to diffuse into the dodecane at 1500 psi. To achieve the measured 2.5 g (3.4 mL) of dodecane recovered at 500 psi, 0.137 g of N2 would have to expand. Modelling of the diffusion of N_2 into the discs would have to be used to estimate if these amounts are reasonable or expected during the duration of the experiment.

Table III.2.2: Mass of dodecane occupying 10.88 cm^3 pore space at tested pressures.

Pressure (psi)	Density (g/cm^3)	Mass dodecane per disc (g)	Mass dodecane per 8 discs (g)
0	0.74573	8.1135	64.9083
250	0.74693	8.1266	65.0128
500	0.74825	8.1410	65.1277
1000	0.75068	8.1674	65.3392
1500	0.75303	8.1930	65.5437

Table III.2.3: Experimental data for the first 14 tests

	vacuum	vacuum DD	Press to 1500 psi	Drain 1500 psi	Draining 1000 psi	Draining 500 psi	Draining 250 psi	Draining 0 psi	Draining 1000 psi	Draining 500 psi	Draining 250 psi	Draining 0 psi	total collected
					Min						g		
Experiment 1	5	0	960	1440	1440	120			0.908	3.6793	2.0462	2.8768	9.5103
Experiment 2	5	0	960	960	1446	60	25	130	0.4079	2.9071	1.7003	2.7618	7.7771
Experiment 4	5	0	1023.6	384.6	1162.8	62.4	30	277.2	0.551	2.4717	2.7062	3.9091	9.638
Experiment 5	5	30	1014.6	300	990.6	184.8	114.6	120	0.4734	1.612	3.3049	1.6191	7.0094
Experiment 6	5	50	85	960	260	140	90	120	0.2959	1.7634	3.456	1.2479	6.7632
Experiment 7	5	30	960	190	150	65	55	1200	0.2234	1.1025	3.0133	2.9975	7.3367
Experiment 8	5	30	1200	405	1335	115	20	20	0.3014	2.7108	3.4212	1.7994	8.2328
Experiment 9	5	30	960	570	1080	120	135	20	0.2629	2.3783	1.8135	3.9755	8.4302
Experiment 10	5	30	960	570	1080	120	135	20	0.2702	2.3462	1.6832	3.9997	8.2993
Experiment 11	5	30	4320	210	1260	210	120	20	0.3106	2.6152	1.6799	3.7803	8.386
Experiment 12	5	30	4320	210	1260	210	120	20	0.242	2.3936	2.4456	2.2494	7.3306
Experiment 13	5	30	1020	1020	4320	210	121	20	0.4087	2.9385	0.5688	3.5465	7.4625
Experiment 14	5	30	1020	1020	4320	210	122	20	0.4388	3.0814	1.5004	2.6285	7.6491
Averages			1529	525	1304	136	88	179	0.3407	2.2945	2.3448	2.8987	7.8787

A series of additional experiments (total of 62 experiments) were performed using nitrogen, methane, and helium to further understand the parameters controlling release of dodecane during pressurization from 1500 psi to 1000 psi. Table III.2.4 lists the gas densities at pressures used in the experiment. For all three gases, more dodecane was produced than expected due to the expansion of dodecane as result of the change in density, which would be on the order of 0.2 g. The average collection of dodecane for methane extraction was the greatest, 2.0 g (+/- 0.9), followed by nitrogen with an amount of 0.49 g (+/1 0.25), and helium 0.27 g (+/- 0.18).

Table III.2.4: Gas and fluid density (g/mL) with pressure

20^o C				
Pressure (psia)	Nitrogen	Methane	Helium	Carbon Dioxide
15	0.0011889	0.00068201	0.00016976	0.0018776
265	0.021076	0.01244	0.002975	0.036801
515	0.041038	0.024962	0.0057354	0.082449
765	0.060986	0.038267	0.0084519	0.1568
830.93				0.1942
830.93				0.77339
1015	0.080826	0.052333	0.011126	0.80856
1265	0.10046	0.067067	0.013757	0.83915
1515	0.11981	0.082291	0.016348	0.86161

50^o C				
Pressure (psia)	Nitrogen	Methane	Helium	Carbon Dioxide
15	0.0010783	0.00061833		0.0017007
265	0.019044	0.011163		0.032268
515	0.036957	0.022155		0.068267
765	0.054756	0.03357		0.11268
1015	0.072382	0.045367		0.17194
1265	0.089778	0.057474		0.26404
1515	0.10689	0.069794		0.43887

The over production by methane could be due to diffusion of gas into the dodecane, and subsequent expansion of that gas during depressurization. The molecular diameters of nitrogen, methane, and helium are 155 pm, 414 pm, and 31 pm respectively, and the molecular masses are 28 for nitrogen, 16 for methane, and 4 for helium. Helium is therefore the smallest and lightest of the three, so should diffuse faster. Methane is lighter than nitrogen, but has a significantly larger diameter so potentially has a slower diffusion rate. The diffusion of methane and nitrogen may also be driven or limited by the solubility of the gas in dodecane.

According to Graham's law, the rate of diffusion (or effusion) is proportional to the mass of the molecule according to the relationship:

$$\frac{Rate_{gas\ 1}}{Rate_{gas\ 2}} = \sqrt{\frac{Mass_{gas\ 2}}{Mass_{gas\ 1}}}$$

This would result in Rate $_{Nitrogen}$ = 0.75 Rate $_{Methane}$. Complicating this relationship is solubility methane is about 4 times more soluble in dodecane than nitrogen, so the total amount diffusing in to the dodecane is greater for methane providing a stronger gas drive. Other factors that can influence the diffusion rate are differences in the porosity or density of the ceramic discs, differences in the geometry of the duplicate experimental systems, as well as the amount of water sorbed into the discs.

To investigate this, discs were saturated with dodecane at 1500 psi and allowed to drain, maintaining pressure at 1500 psi. The dodecane saturated ceramic discs were then allowed to equilibrate at 1500 psi with the gas for a period of time, ranging from a few hours to a few days, to see if increased diffusion time resulted in increased production of dodecane from the discs. After the period of equilibration, pressure was dropped to 1000 psi and released dodecane was collected. Data for all three gases is shown in Figure III.2.14.

The results for each gas were also plotted separately and fitted with a linear regression line (Figure III.2.15). The best correlation to equilibration time was found for nitrogen (R^2 = 0.81). Only a few helium experiments were performed and no correlation of dodecane to equilibration time was found (R^2 = 0.005), presumably because the equilibration time was short. The correlation for methane was also poor (R^2 = 0.13), over a wide range of equilibration times and experiments.

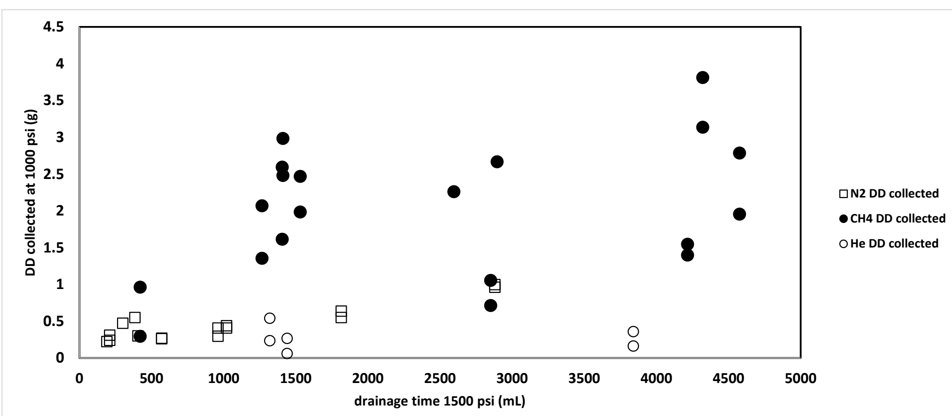

Figure III.2.14: Dodecane collected after depressurization from 1500 to 1000 psi with equilibration time at 1500 psi for the three gasses.

In an effort to improve the correlation for the methane and nitrogen experiments, the data from the methane and nitrogen experiments were correlated to both equilibration time at 1500 psi and the rate of production from 1500 to 1000 psi. For the nitrogen data, this improved the fit to an R^2 of 0.92 and for methane the correlation improved to an R^2 of 0.40. However, that is only a slight improvement from the linear correlation with just depressurization rate (R^2 = 0.38) indicating that for methane this rate of depressurization may be a more important factor. Despite the variation in the data, *overall it appears that methane is more effective in enhancing the release of dodecane during depressurization.*

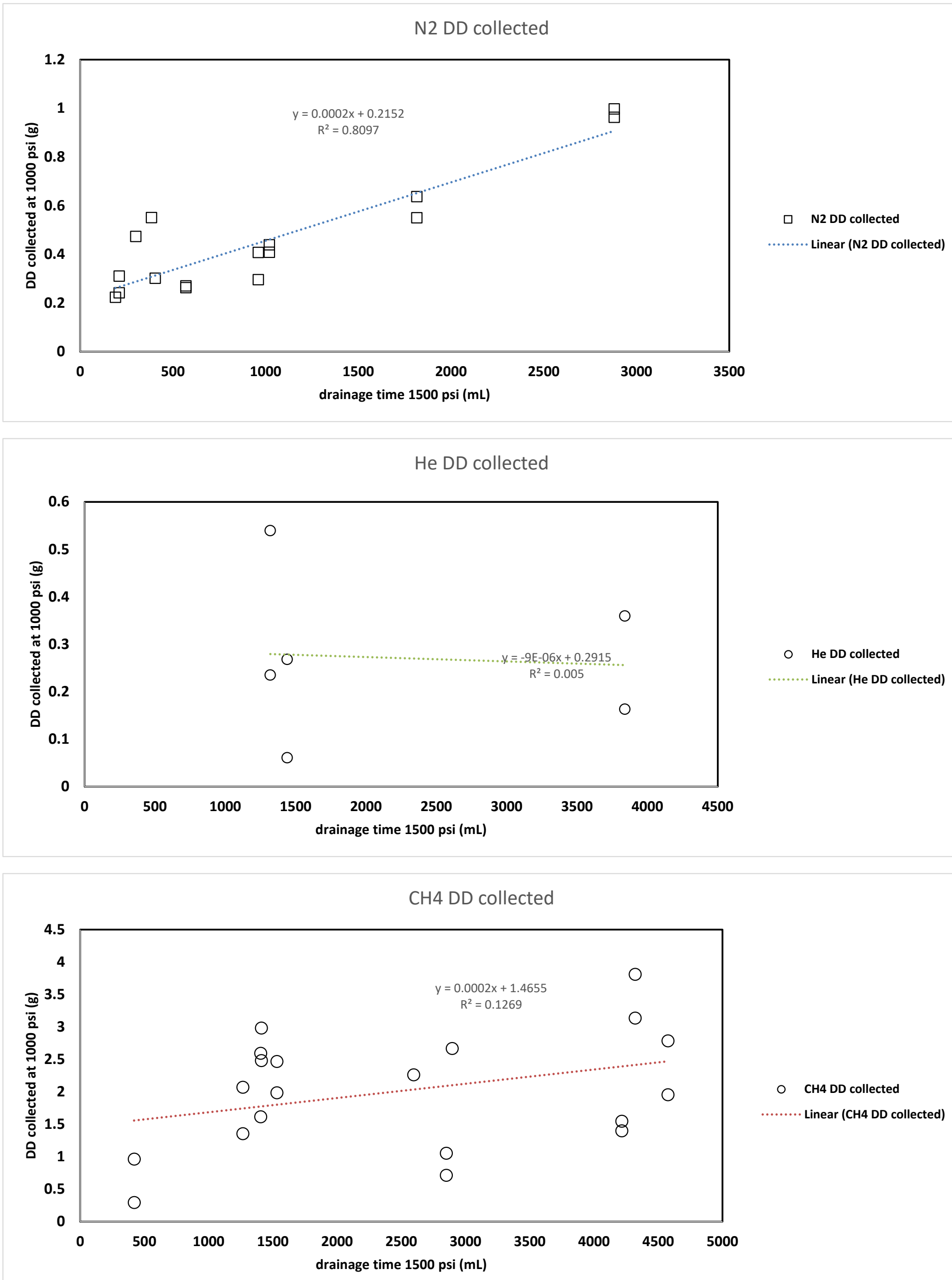

Figure III.2.15: Correlation of dodecane collected after depressurization from 1500 to 1000 psi with equilibration time at 1500 psi for the three gasses.

Effect of Temperature

Similar tests were performed at room temperature and nearer reservoir temperature (50°C) to examine the effect of temperature. Depressurization from 1500 psi to 1000 psi produced slightly less dodecane at increased temperature but overall recovery with depressurization to 0 psi was unchanged (Figure III.2.16).

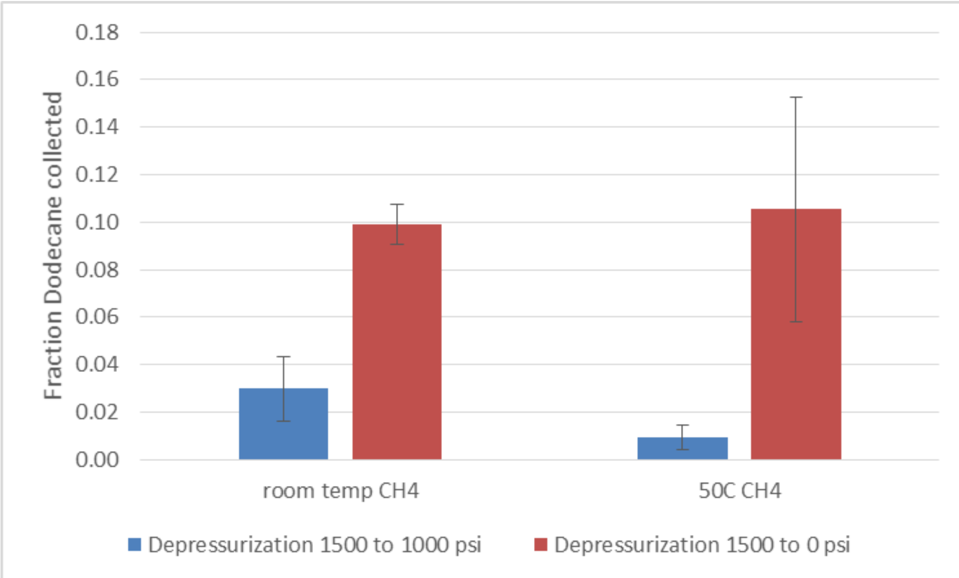

Figure III.2.16: Oil production with room temperature and 50°C methane.

Effect of using CO_2

So as not to saturate the dodecane with dissolved carbon dioxide, the system was pressurized with 1500 psi CH_4 to ensure complete saturation of the ceramic, and then displaced with supercritical CO_2 (also at 1500 psi, 50°C). Oil was collected during the displacement and also during depressurization. An atypically large fraction of the oil was produced during the displacement alone (Figure III.2.17), followed by typical amounts upon depressurization. This indicates there is a mechanism causing the ejection of the oil from the ceramic. Suggested mechanisms are interfacial tension reduction, and preferential wetting of the water-wet ceramic by the CO_2. If these mechanisms occurred in the early tests, it was not clear due to the small amount of oil present.

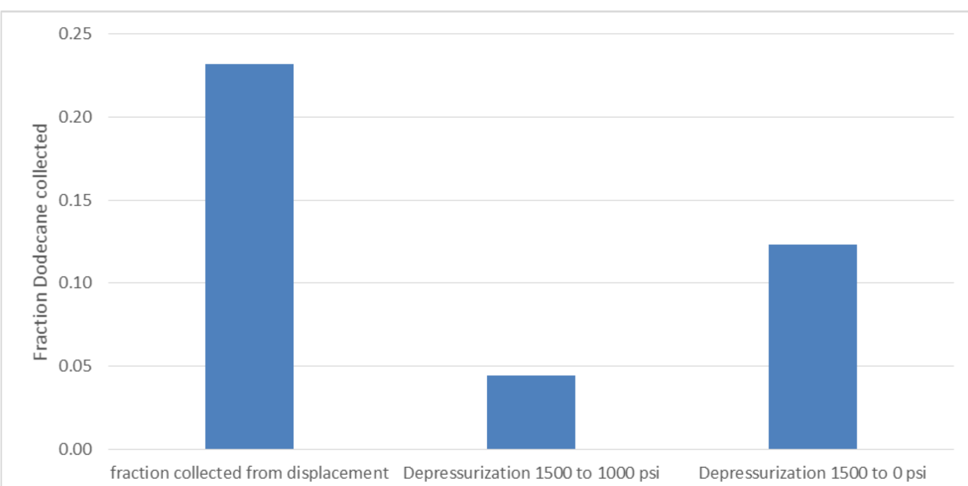

Figure III.2.17: Oil recovered during the 3 stages of the enhancement by CO_2 experiment.

Effect of using water

Using a similar procedure without applying pressure (the fluids used are relatively incompressible) the oil recovery was 0.88±0.23 when using dry media and 0.66±0.07 for pre-moistened media (Figure III.2.18). To understand the process better, visual observations were used. When water was applied to the oil-saturated media, the oil spontaneously effused from the rock as the water was selectively imbibed (Figure III.2.19). The probable reason for the lower production of oil for the moistened ceramic is presented. In both cases water is the preferred fluid to contact the ceramic. In the dry case, the oil was likely displaced in almost piston-like displacement (Mumley et al., 1986). Water imbibing in the moist case could flow in films and pendular structures around the oil resulting in some snap-off and oil retention (Ransohoff and Radke, 1987).

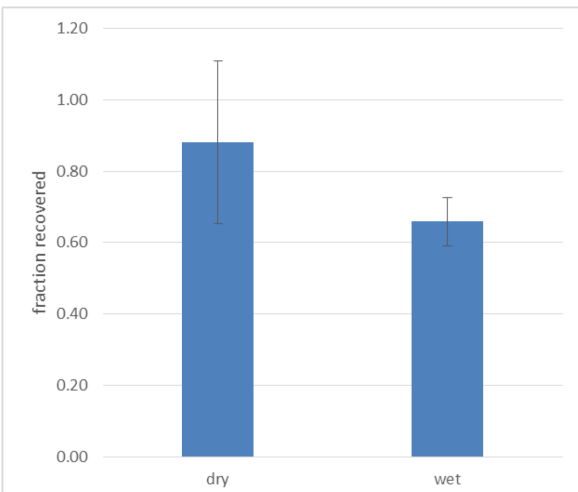

Figure III.2.18: Oil recovery for water displacement in dry and moistened ceramic disks.

Figure III.2.19: Oil spontaneously effusing from the ceramic as water is imbibed.

Subtask Summary

Over the course of the project, we built and operated two high-pressure process evaluation test rigs. The first one, in early tests, identified flaws in the experiment conceptualization. The second test rig and improvements of the procedure were used in numerous (>60) tests to evaluate gas dissolution, depressurization, and imbibition using nitrogen, methane, helium, carbon dioxide, and water. In terms of effectiveness, helium was a poor performer. Helium would not be used in the field anyway due to expense and rarity. Nitrogen was better than the helium and is much more available. As a surrogate for air, this indicates that for the purposes of gas injection, air might be useful. The chemical effects of altering the oxidation-reduction potential of the subsurface were not considered here, as ceramic is nonreactive and shales typically contain oxygen-reactive minerals. Methane was fairly effective at enhancing EOR and is often available near producing fields. Carbon dioxide was the most effective of the gas-like fluids although would likely be a supercritical fluid for EOR conditions. Please note that mass-wise, about seven times the CO_2 is needed compared to the methane to reach the desired conditions. Mixtures of the two gases might be much more effective and easier to obtain and use.

Compared to the gas-like fluids however, water was the superior fluid to enhance oil production. This may be an artifact of the water-wetting ceramic used; however the result was still unexpected. Imbibition of water into shales has also been observed to displace oil (Fakcharoenphol et al., 2014), and hypotheses of separate water-wetting and oil wetting pathways in shales have been stated (Ghanbari et al., 2014). If true, water could imbibe somewhat drawn by capillary and osmotic potentials, displacing local oil into fractures where it can be collected and produced.

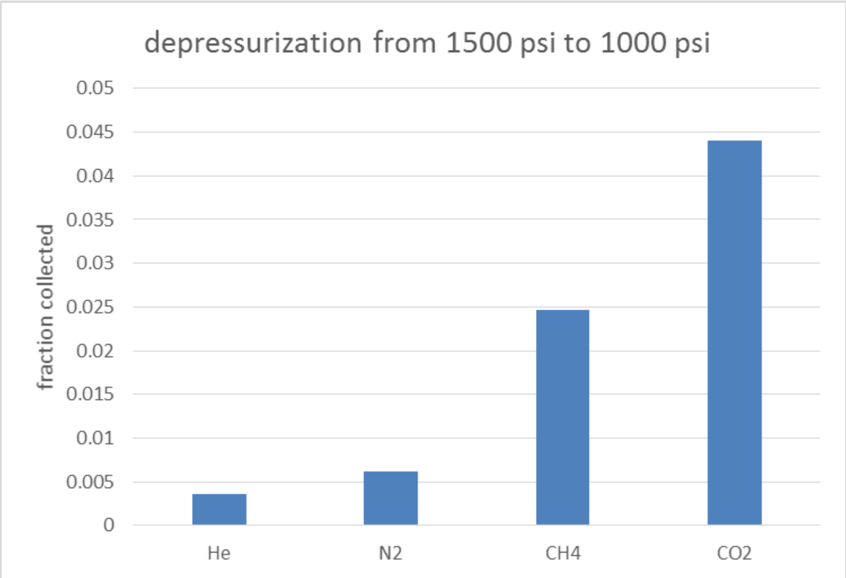

Figure III.2.20: Comparison of the effectiveness of the four gas-like fluids used in the EOR tests.

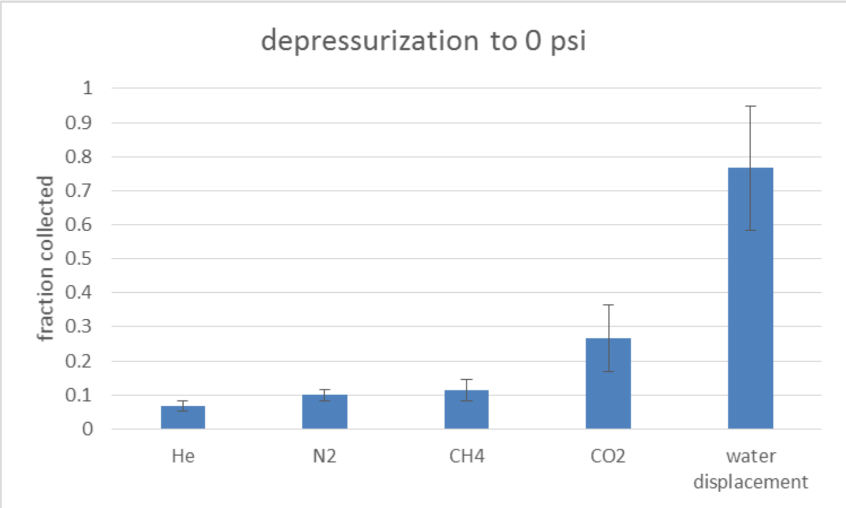

Figure III.2.21: Comparison of all fluids used in the EOR experiments.

Proppant transport

During the duration of the project, we developed and built a proppant transport apparatus allowing flexible setups. The initial concept of the apparatus shown in Figure III.2.22. In this apparatus, proppant-laden fluid is injected between two transparent blocks that are set with a desired aperture. Random fracture apertures can be created using roughened glass between plates or fracture analog techniques (Su et al., 1999, Kneafsey and Pruess, 1997), or cornered fractures (Figure 22) can be configured.

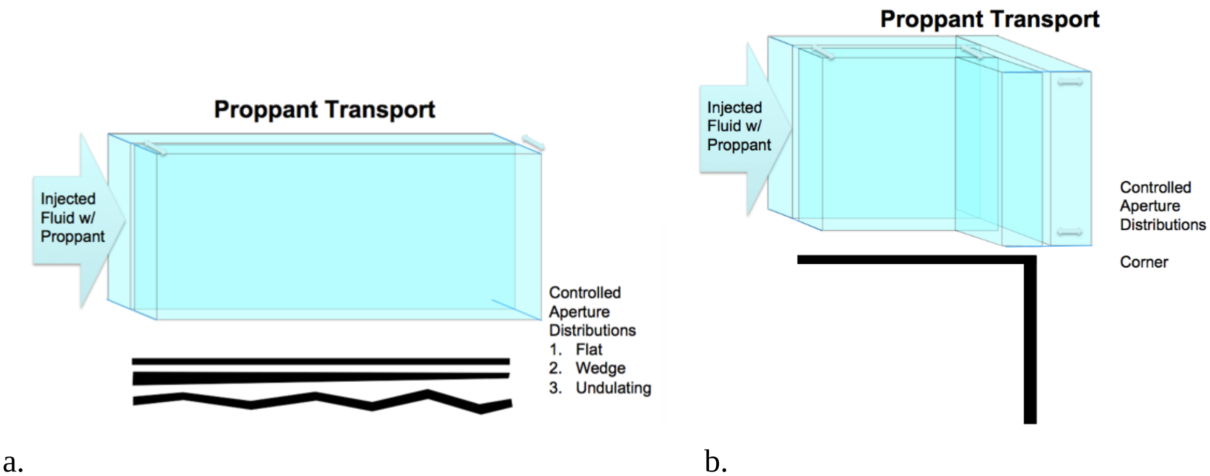

Figure III.2.22: Proppant visualization experiment setup. a. planar, wedge, and random fractures. b. cornered fractures.

Our physical system is shown in Figure III.2.23. Although conceptually easy, controlling leaks and flows were somewhat problematic. Flowing at pressure is very difficult for systems having large surface areas (a pressure of 10 psi requires a resistive force of 720 pounds for blocks the size we use as well as safety engineering) limiting alternatives. Improvements include pumping out of the system, such the fracture operates under a pressure slightly lower than atmospheric pressure and improved proppant mixing, loading, and suspension are being implemented and tests will be continued.

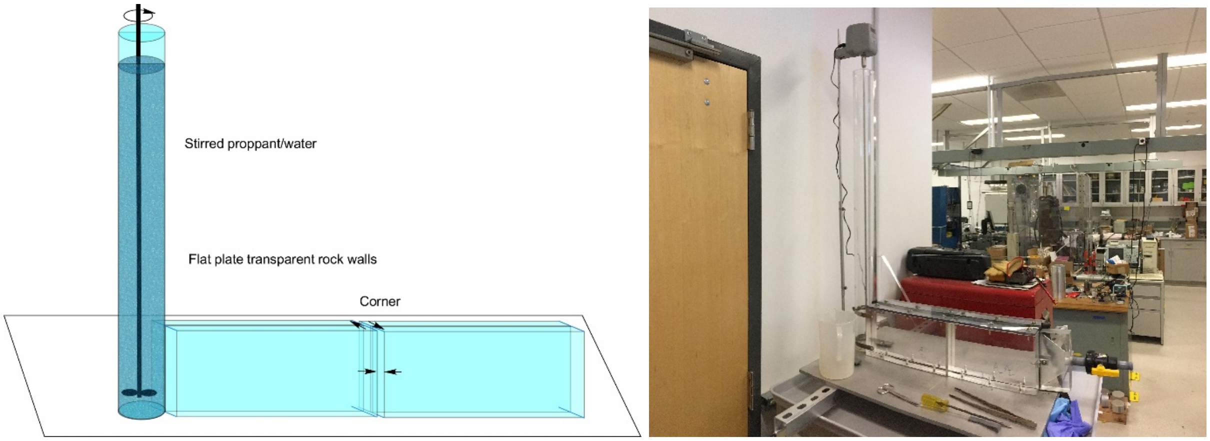

Figure III.2.23: Current proppant visualization setup. a. schematic, b. photo.

Micro and nano-scale infrared imaging of shale (Partially funded by this project)

Benchtop Fourier Transform Infrared Spectroscopy (FTIR) measurements were performed on a total of 4 bulk shale samples and a total of 6 powder samples from different origins, with replicates to identify mineralogical and organic composition. Geranium hemisphere imaging on 6 samples was performed to obtain microscale chemical images (Figure III.2.24). Synchrotron Infrared Nano Spectroscopy (SINS) imaging was performed on 4 polished shale samples to obtain nanoscale chemical images at the Advanced Light Source infrared beamline 5.4 (Figure III.2.24). To correlate the nanoscale imaging using SINS which is slow but easy to interpret to the microscale imaging which is fast and difficult to interpret, a machine learning analysis was performed allowing detailed understanding of the shale surface using germanium hemisphere rapid scanning (Figure III.2.25). Details of this work are published in Hao et al. (2018)

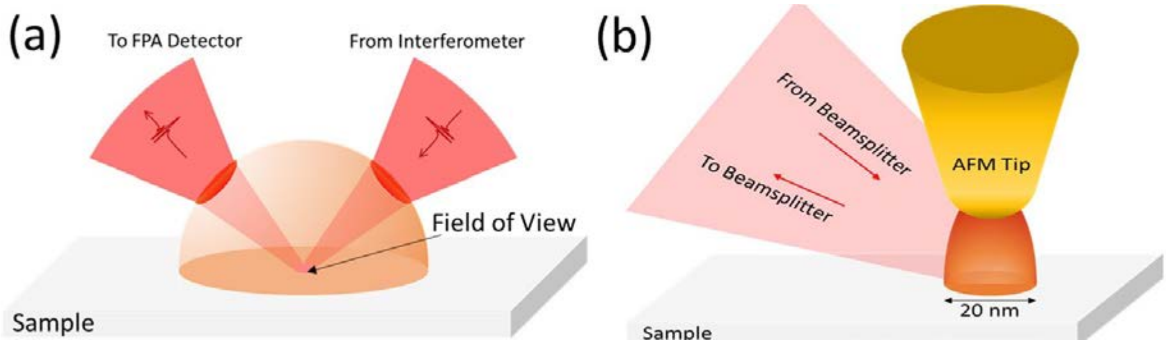

Figure III.2.24: FTIR and SINS imaging techniques from Hao et al., (2018).

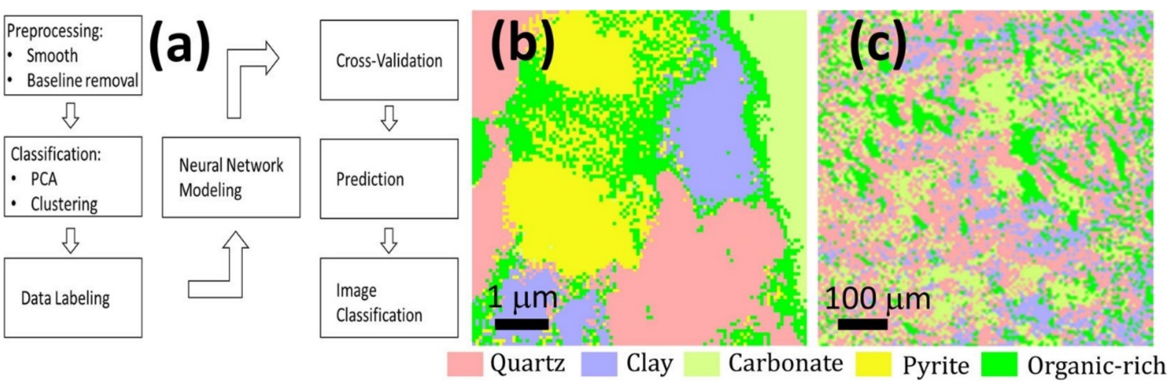

Figure III.2.25: Diagram of the steps of performing neural network modeling and prediction (a) and predicted mineral classification map at nanometer scale (b) and micrometer scale (c). In the classification maps the pink corresponds to quartz, light blue clay, light green carbonate, yellow pyrite, and green organic-rich regions. From Hao et al., (2018).

PART IV:

MOLECULAR-SCALE STUDIES

Phase I, Task 6: Molecular simulation analysis of system interactions

Phase II, Task 5: Molecular simulation analysis of system interactions

In this task, we attempted to study the expected fluid interactions and behavior in the most promising production scenarios identified in simulation tasks, as further focused by the laboratory results. Such fluid systems may include either mobilized oil (e.g., after a thermal treatment), or combinations of the native oil and displacing fluids (e.g., liquid water, steam, CO_2, CH_4, etc.) as well as kerogens and other high-viscosity hydrocarbons. Two types of molecular simulations were being used: Grand Canonical Monte Carlo (GCMC) simulations at constant temperature, chemical potential of the confined fluid, and pore volume, and classical Molecular Dynamics (MD) simulations at constant density (pressure) and temperature.

We began creating a realistic model of the pore structure using (a) a simple slab and a cylindrical geometry, as well as (b) micro-CT data from a sample from the Bakken formation. This model allowed us to obtain the thermodynamic phase behavior and fluid flow in a relatively straightforward manner as a function of the pore size. The intermolecular and intramolecular interactions were represented by effective force fields where the interaction energy is a function of intermolecular distance and several kinds of electrostatic interactions. Variations in electronic distribution were be incorporated via charges placed at molecular sites.

In Phase I of the project, we conducted molecular fluid dynamics simulations involving flow of water, water plus alkanes, water plus carboxylic acids, and water plus multiple species within nano-scale clay pores. We observed significant differences in the nature of the surface interactions (both edge and basal plane) with both species, and significant interactions were apparent at the surfaces when the species are mixed. Alkane simulations alone appear to be insufficient to accurately model surface interactions.

We attempted to perform MFD simulations for a small clay pore, then extend the system to 60,000 molecules and add a larger concentration of hydrocarbons to examine the details of clustering and associations with surfaces. We also attempted to leverage electron microscopy work performed outside this project, to connect MFD results to real-world visualizations of the 2-5 nm scale.

Preliminary results were promising, but the expansion to larger systems consumed increasing computational resources. As budgeted, simulations of the required complexity (to bridge the scale gap between the small pore and the micro-scale) were impractical within the original project scope. The remaining (limited) resources were diverted to the micro-scale visualization task, which throughout Phase I and Phase II had been providing better results and aligned with project deliverables.

PROJECT BUDGET

Actual Cost for the full FWP	Funds available for the full FWP	Balance of unspent funds (September 2018)
$898,992	$899,000	$7.00

PUBLICATIONS AND COMMUNICATION

The project resulted in 3 papers and 6 presentations (September 2018).

Peer-reviewed papers:

Hao, Z., Bechtel, H. A., Kneafsey, T., Gilbert, B. & Nico, P. S. 2018. Cross-Scale Molecular Analysis of Chemical Heterogeneity in Shale Rocks. *Scientific Reports*, 8, 2552.

Voltolini, M., Haboub, A., Dou, S., Kwon, T.H., MacDowell, A.A., Parkinson, D.Y. and Ajo-Franklin, J., 2017. The emerging role of 4D synchrotron X-ray micro-tomography for climate and fossil energy studies: five experiments showing the present capabilities at beamline 8.3. 2 at the Advanced Light Source. *Journal of synchrotron radiation*, 24(6), pp.1237-1249.

Queiruga, A. F., Moridis, G. J., Numerical experiments on the con- vergence properties of state-based peridynamic laws and influence functions in two-dimensional problems. *Computer Methods in Applied Mechanics and Engineering*, 322 (2017): 97-122. doi: 10.1016/j.cma.2017.04.016

Presentations:

Reagan, M.T.., "Numerical and Laboratory Investigations for Maximization of Production from Tight/Shale Oil Reservoirs: From Fundamental Studies to Technology Development and Evaluation," Mastering the Subsurface, Carbon Storage and Oil and Natural Gas Conference, Pittsburgh, PA 13-16 August 2018.

Reagan, M.T., "Numerical and Laboratory Investigations for Maximization of Production from Tight/Shale Oil Reservoirs: From Fundamental Studies to Technology Development and Evaluation," Mastering the Subsurface, Carbon Storage and Oil and Natural Gas Conference, Pittsburgh, PA 1-3 August 2017.

Reagan, M.T., "Simulation of the Shale Oil System: from Molecular Fluid Dynamics to Reservoir Scale," Mastering the Subsurface, Carbon Storage and Oil and Natural Gas Conference, Pittsburgh, PA 16-18 August 2016.

Quieruga, A.F., "Smoothing Methods to Address the Numerical Stability of Peridynamics Near the Fracture Tip in Hydraulic Extension," US National Congress for Theoretical and Applied Mechanics, 7 June 2018.

Queiruga, A.F., "Numerical Experiments on the Convergence Properties of State-based Peridynamic Laws and Influence Functions in Two-Dimensional Problems" World Congress on Computational Mechanics, 24 July 2018.

Voltolini, M., "New Insights into Fracture Evolution in Rocks Relevant to the Geological Carbon Sequestration from In Situ Synchrotron X-ray Microtomography," H41C-1309, AGU Fall Meeting, San Francisco, CA, 14-18 December 2015.

REFERENCES

Dusterhoft, R., Nguyen, P. and Conway, M., 2004, January. Maximizing effective proppant permeability under high-stress, high gas-rate conditions. In *SPE Annual Technical Conference and Exhibition*. Society of Petroleum Engineers.

Fakcharoenphol, P., Kurtoglu, B., Kazemi, H., Charoenwongsa, S. & Wu, Y.-S. 2014. The Effect of Osmotic Pressure on Improve Oil Recovery from Fractured Shale Formations. SPE Unconventional Resources Conference – USA. The Woodlands, Texas, USA: Society of Petroleum Engineers.

Freeman, C.M., G.J. Moridis, D. Ilk, and T.A. Blasingame, A Numerical Study of Performance for Tight Gas and Shale Gas Reservoir Systems, *Journal of Petroleum Science and Engineering* **108**, 22-39, 2013 (doi: 10.1016/j.petrol.2013.05.007)**.**

Ghanbari, E., Xu, M., Dehghanpour, H. & Bearinger, D. 2014. Advances in Understanding Liquid Flow in Gas Shales. SPE/CSUR Unconventional Resources Conference. Calgary, Alberta, Canada: Society of Petroleum Engineers.

Hao, Z., Bechtel, H. A., Kneafsey, T., Gilbert, B. & Nico, P. S. 2018. Cross-Scale Molecular Analysis of Chemical Heterogeneity in Shale Rocks. *Scientific Reports*, 8, 2552.

Jamialahmadi, M., Emadi, M. & Müller-Steinhagen, H. 2006. Diffusion coefficients of methane in liquid hydrocarbons at high pressure and temperature. *Journal of Petroleum Science and Engineering*, 53, 47-60.

Kneafsey, T. J. & Pruess, K. 1997. Preferential Flow Paths and Heat Pipes: Results from Laboratory Experiments on Heat-Driven Flow in Natural and Artificial Rock Fractures. Berkeley, California: Lawrence Berkeley National Laboratory.

Maxwell, S., 2011. Microseismic hydraulic fracture imaging: The path toward optimizing shale gas production. *The Leading Edge*, *30*(3), pp.340-346.

Moridis, G.J., T. Blasingame and C.M. Freeman**,** Analysis of Mechanisms of Flow in Fractured Tight- Gas and Shale-Gas Reservoirs, Paper SPE 139250, 2010 SPE Latin American & Caribbean Petroleum Engineering Conference, Lima, Peru, 1–3 December 2010.

Mumley, T. E., Radke, C. J. & Williams, M. C. 1986. Kinetics of Liquid/Liquid Capillary Rise I. Experimental Observations. *Journal of Colloid and Interface Science*, 109, 398-411.

Olorode, O., Numerical Modeling of Fractured Shale-Gas and Tight-Gas Reservoirs Using Unstructured Grids, MSc. Thesis, Texas A&M University, 2012.

Ransohoff, T. C. & Radke, C. J. 1987. Weeping Flow Around Nonwetting Bubbles Trapped in Constricted Noncircular Pores. *PhysicoChemical Hydrodynamics*, 8, 255-263.

Su, G. W., Geller, J. T., Pruess, K. & Wen, F. 1999. Experimental studies of water seepage and intermittent flow in unsaturated, rough-walled fractures. *Water Resources Research*, 35, 1019-1037.

Upreti, S. R. & Mehrotra, A. K. 2002. Diffusivity of CO2, CH4, C2H6 and N2 in athabasca bitumen. *The Canadian Journal of Chemical Engineering*, 80, 116-125.

Voltolini, M., Kwon, T.H. and Ajo-Franklin, J., 2017. Visualization and prediction of supercritical CO2 distribution in sandstones during drainage: An in situ synchrotron X-ray micro-computed tomography study. *International Journal of Greenhouse Gas Control*, *66*, pp.230-245.

Zuo, L., Ajo-Franklin, J.B., Voltolini, M., Geller, J.T. and Benson, S.M., 2017. Pore-scale multiphase flow modeling and imaging of CO2 exsolution in Sandstone. *Journal of Petroleum Science and Engineering*, *155*, pp.63-77.